Universidad de Málaga

Escuela Técnica Superior de Ingeniería de Telecomunicación

(Programa de doctorado en Ingeniería de Telecomunicación)

TESIS DOCTORAL POR COMPENDIO DE PUBLICACIONES

Surface-emitting antennas for optical phased arrays based on silicon waveguides

Autor:

Pablo Ginel Moreno

Directores:

Alejandro Ortega Moñux
Pavel Cheben

21 de julio de 2023

UNIVERSIDAD
DE MÁLAGA

AUTOR: Pablo Ginel Moreno

https://orcid.org/0000-0003-3406-0805

EDITA: Publicaciones y Divulgación Científica. Universidad de Málaga

DECLARACIÓN DE AUTORÍA Y ORIGINALIDAD DE LA TESIS PRESENTADA PARA OBTENER EL TÍTULO DE DOCTOR

D.PABLO GINEL MORENO
Estudiante del programa de doctorado EN INGENIERÍA DE TELECOMUNICACIÓN de la Universidad de Málaga, autor/a de la tesis, presentada para la obtención del título de doctor por la Universidad de Málaga, titulada: SURFACE-EMITTING ANTENNAS FOR OPTICAL PHASED ARRAYS BASED ON SILICON WAVEGUIDES

Realizada bajo la tutorización de ALEJANDRO ORTEGA MOÑUX y dirección de ALEJANDRO ORTEGA MOÑUX Y PAVEL CHEBEN (si tuviera varios directores deberá hacer constar el nombre de todos)

DECLARO QUE:

La tesis presentada es una obra original que no infringe los derechos de propiedad intelectual ni los derechos de propiedad industrial u otros, conforme al ordenamiento jurídico vigente (Real Decreto Legislativo 1/1996, de 12 de abril, por el que se aprueba el texto refundido de la Ley de Propiedad Intelectual, regularizando, aclarando y armonizando las disposiciones legales vigentes sobre la materia), modificado por la Ley 2/2019, de 1 de marzo.

Igualmente asumo, ante a la Universidad de Málaga y ante cualquier otra instancia, la responsabilidad que pudiera derivarse en caso de plagio de contenidos en la tesis presentada, conforme al ordenamiento jurídico vigente.

En Málaga, a 27 de MAYO de 2023

Fdo.: PABLO GINEL MORENO Doctorando	Fdo.: ALEJANDRO ORTEGA MOÑUX Tutor/a
Fdo.: ALEJANDRO ORTEGA MOÑUX Y PAVEL CHEBEN Directores de tesis	

Yo, **Alejandro Ortega Moñux,** con DNI , tutor y director de la tesis titulada "Surface-emitting antennas for optical phased arrays based on silicon waveguides", realizada por el estudiante del programa de doctorado en Ingeniería de Telecomunicación **Pablo Ginel Moreno**, con DNI , autorizo la lectura de dicha tesis doctoral.

De igual forma, confirmo que las publicaciones que avalan esta tesis, las cuales se pueden consultar en el Capítulo 4 de esta memoria, no han sido utilizadas en tesis anteriores.

En Málaga, a 27 de mayo de 2023.

Fdo. Alejandro Ortega Moñux
Director y tutor de tesis

Edificio Pabellón de Gobierno. Campus El Ejido. 29071
Tel.: 952 13 10 28 / 952 13 14 61 / 952 13 71 10
E-mail: doctorado@uma.es

Yo, **Pavel Cheben,** director de la tesis titulada "Surface-emitting antennas for optical phased arrays based on silicon waveguides", realizada por el estudiante del programa de doctorado en Ingeniería de Telecomunicación **Pablo Ginel Moreno**, con DNI autorizo la lectura de dicha tesis doctoral.

De igual forma, confirmo que las publicaciones que avalan esta tesis, las cuales se pueden consultar en el Capítulo 4 de esta memoria, no han sido utilizadas en tesis anteriores.

En Málaga, a 05 de junio de 2023.

Fdo. Pavel Cheben
Director de tesis

Surface-emitting antennas for optical phased arrays based on silicon waveguides

Pablo Ginel Moreno

Acknowledgements

Quiero dedicar esta página de mi Tesis para agradecer a todas las personas que me han apoyado durante todos estos años y han estado a mi lado en todo momento. No hay palabras para expresar el reconocimiento que merecéis y por ello parte de este trabajo también es vuestro.

Quisiera empezar agradeciendo a mis dos directores de Tesis. A Alejandro Ortega Moñux por su incansable ánimo y noble generosidad, por estar siempre cuando se le necesita y por ayudar sin recibir nada a cambio. Nos conocimos hace unos 6 años, y todo lo que he aprendido en este tiempo en parte te lo debo a ti. Para mi no eres solo un profesor y director ejemplar, sino que te considero un amigo y espero que podamos seguir siéndolo muchos años más. A mi director Pavel Cheben también le quiero agradecer por su infinita sabiduría y su gran corazón. Cuando llegué por primera vez a Canadá en 2019 y sentía que estaba más solo que nunca, alejado de mis seres queridos y en un país desconocido, él sin apenas conocerme, me trató como si fuese de su propia familia. A raíz de esa estancia y todos estos años de trabajo se ha forjado una gran relación que me gustaría mantener para siempre. De corazón, gracias a ambos.

A Nuria quiero agradecer todo su apoyo, en los momentos más complicados y en los más felices ella siempre ha estado ahí. Ayudándome, aconsejándome, abrazándome. Gracias, porque este trabajo es tuyo, y sin ti no hubiera sido posible haberlo acabado. Por infinitos años de apoyo y cariño, gracias.

A toda esa gente con la que he compartido tan buenos momentos, a mis amigos, a los compañeros de laboratorio, gracias a todos, porque con vosotros ha sido mucho más liviano este proceso tan duro que es la Tesis. Especial mención para todo el equipo de profesores que conforma el Photonics & RF Lab, Íñigo, Gonzalo, Pepe, Robert, gracias a todos. Con vosotros al mando todos los días de trabajo han sido un placer, esto se debe a que irradiais pasión por lo que hacéis y siempre se aprende algo, eso al final se agradece cuando pasas tantas horas en el labotario.

Y por último, y no por ello menos importante a mi familia. En especial a mis padres Rafa y Toñi, nunca podré devolveros todo lo que me habéis dado en esta vida. Sin vosotros yo no podría haber llegado hasta aquí. Gracias de corazón.

Funding

Esta Tesis ha sido posible gracias al apoyo y financiación de los siguientes programas, proyectos e instituciones:

- Ministerio de Ciencia, Innovación y Universidades.
  - Beca de formación de profesorado universitario (FPU).

    Número: FPU20/03487
- Ministerio de Economía y Competitividad (Generación de conocimiento y retos de investigación).
  - Título: Materiales y dispositivos fotónicos sublongitud de onda para aplicaciones del mundo real.

    Referencia: PID2019-106747RB-I00
- Junta de Andalucía (FEDER Andalucía).
  - Título: Fotónica integrada para escaneo de haces ópticos en aplicaciones LIDAR.

    Referencia: UMA20-FEDERJA-158
- National Research Council Canada (High Throughput and Secure Networks Challenge Program)
  - Título: High-performance metamaterial off-chip couplers for telecom and free-space optical communications

    Referencia: CSTIP Grant - 209
  - Título: Metamaterial waveguides for on-chip spectral control

    Referencia: CSTIP Grant - 210
- Ministerio de Ciencia e Innovación
  - Título: Sensores de campo lejano en fotónica del silicio.

    Referencia: TED2021-130400B-I00

Compendium of publications

Durante la realización de la tesis, el doctorando ha sido primer autor en tres publicaciones en revistas indexadas en el JCR cuya puntuación ANECA agregada es superior a 1. Además, ha participado en seis conferencias con revisión por pares de ámbito nacional e internacional, de las que en cuatro ha sido primer autor. De acuerdo con las regulaciones de los estudios doctorales en la Universidad de Málaga, se propone que las mencionadas publicaciones respalden la presentación de esta Tesis como un compendio de publicaciones.

Publicaciones que avalan la Tesis

1. Pablo Ginel-Moreno, Daniel Pereira-Martín, Abdelfettah Hadij-ElHouati, Winnie N. Ye, Daniele Melati, Dan-Xia Xu, Siegfried Janz, Alejandro Ortega-Moñux, J. Gonzalo Wangüemert-Pérez, Robert Halir, Íñigo Molina-Fernández, Jens H. Schmid, and Pavel Cheben, "Highly efficient optical antenna with small beam divergence in silicon waveguides," Optics Letters vol. 45, no. 20, pp. 5668-5671 (2020).

   Índices de calidad de la publicación en su año de publicación:

   - Factor de impacto de la revista (JIF): 3.776.
   - Ranking de la revista según el factor de impacto en el área de Óptica: 22/99. Primer cuartil (Q1).
   - Proceso de revisión por pares (peer-review).
   - Actualmente cuenta con 26 referencias en Google Scholar.

2. Pablo Ginel-Moreno, Alejandro Sánchez-Postigo, José de-Oliva-Rubio, Abdelfettah Hadij-ElHouati, Winnie N. Ye, J. Gonzalo Wangüemert-Pérez, Íñigo Molina-Fernández, Jens H. Schmid, Pavel Cheben, and Alejandro Ortega-Moñux, "Millimeter-long metamaterial surface-emitting antenna in the silicon photonics platform," Optics Letters 46(15), 3733- 3736 (2021).

   Índices de calidad de la publicación en su año de publicación:

   - Factor de impacto de la revista (JIF): 3.560.
   - Ranking de la revista según el factor de impacto en el área de Óptica: 32/101. Primer tercil.
   - Proceso de revisión por pares (peer-review).
   - El artículo fue *Editor's pick* en el mes de su publicación.
   - Actualmente cuenta con 16 referencias en Google Scholar.

3. Pablo Ginel-Moreno, Abdelfettah Hadij-ElHouati, Alejandro Sánchez-Postigo, J. Gonzalo

Wangüemert-Pérez, Íñigo Molina-Fernández, Jens H. Schmid, Pavel Cheben and Alejandro Ortega-Moñux, "On-chip metamaterial antenna array with distributed Bragg deflector for generation of collimated steerable beams," Laser & Photonics Reviews 16(9), 2200164 (2022).

Índices de calidad de la publicación en su año de publicación:

- Factor de impacto de la revista (JIF): 10.947.
- Ranking de la revista según el factor de impacto en el área de Óptica: 6/101. Primer decil (D1) y primer cuartil (Q1).
- Proceso de revisión por pares (peer-review).
- Actualmente cuenta con 1 referencia en Google Scholar.

Contents

1. Introduction

1.1. Silicon photonics for the information society

Modern information society is fundamentally rooted in two pivotal technologies that emerged over 50 years ago: electronic integrated circuits and high-capacity optical communications. These technologies have played a vital role in shaping our modern world. One notable aspect of these technologies is their rapid evolution, as evidenced by Moore's Law in the realm of microprocessors, where the number of transistors in a microprocessor doubles every two years [1]. Similarly, optical communications are experiencing remarkable growth in link capacity, increasing by a factor of 10 every four years [2]. These continuous advancements have been instrumental in propelling relentless progress and fostering innovation, thus defining the ever-evolving technological landscape we navigate today.

In 1969, shortly after the invention of the transistor and the demonstration of the first optical fiber transmission systems, the scientific community drew, for the first time, attention towards the idea of integrated photonics. The integration of optical devices has been always prone to revolutionize the field by seamlessly merging various functionalities into a compact photonic integrated circuit (PIC). This strategy capitalizes on the manifold advantages of scalability, such as the significant reduction in size, weight, and manufacturing costs. Moreover, integration empowers the realization of intricate functionalities that would otherwise be unfeasible with separate components. Until the beginning of this century, the development of PICs has been relatively slow when compared to the advancement of microelectronics, with only a few dominant niche applications, such as III-V semiconductor lasers [3], lithium niobate modulators [4], and wavelength multiplexers [5–7]. However, the landscape has undergone a dramatic shift in recent years with the emergence of Silicon Photonics (SiPh) [8–10].

Silicon is the fundamental material of SiPh technology, which has the property of being transparent in a wide wavelength range used in optical communications. Figure 1.1 shows a typical photonic-wire waveguide on the silicon-on-insulator (SOI) platform, in which the silicon core ($n_{\mathrm{Si}} \sim 3.45$) is surrounded by silicon dioxide ($n_{\mathrm{SiO_2}} \sim 1.45$). The high index contrast ($\Delta n \sim 2$) implies the use of very small waveguide cross-sections (hundreds of nanometers) to maintain the single-mode regime, and leads to very compact bending radii, of the order of only 5 µm, which reduces the size of the integrated circuits. For wavelengths below 1100 nm, where silicon is not transparent, or when high power levels are needed, other technological platforms are used. For example, silicon nitride ($n_{\mathrm{SiN}} \sim 2$), which is compatible with complementary metal-oxide-semiconductor (CMOS) manufacturing processes.

SiPh exhibits two fundamental advantages over other photonic technologies. First, it enables an extremely high integration capacity, allowing for the incorporation of numerous devices within a small chip area. Second, its materials are compatible with the CMOS man-

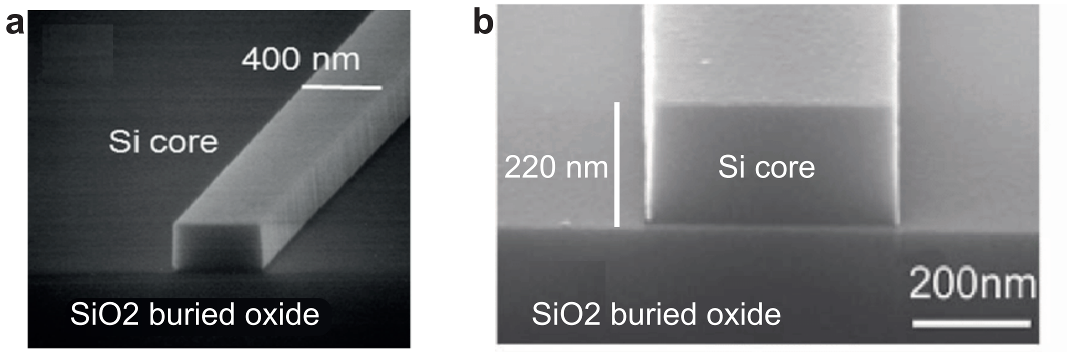

Figure 1.1.: SEM images of a conventional photonic-wire waveguide on SOI. a) 3D perspective of the waveguide prior to having a SiO_2 cladding deposited on top. b) Cross-sectional image of the waveguide. Source of the images [11, 12]

ufacturing processes employed in the field of microelectronics. This has great relevance in practice since it allows to leverage existing technologies and fabrication processes from the microelectronics industry. These two characteristics are key to provide low unit costs when mass fabrication is required, making silicon photonics the perfect technology for many applications that are expected to experience significant market growth. Currently, the silicon photonics market is experiencing exponential growth, with an estimated compound annual growth rate (CAGR) of 49% for the period 2021-2026 according to analysis at Yole Développment (see Fig. 1.2) [13]. This growth estimate is primarily due to a set of groundbreaking applications, including transceivers for data centers (which currently represent over 95% of the market) [14, 15], 5G transceivers [16, 17], health monitors for consumer applications such as smartwatches [18], photonic biosensors [19], photonic quantum computing and artificial intelligence (AI) [20, 21], automotive light detection and ranging (LiDAR) [22–24], and optoelectronic integration (co-packaged optics) [25, 26], among others.

SOI suffers from a lack of flexibility when envisioning its use with other materials in standard manufacturing processes. This, together with its high index contrast, poses some challenges when designing complex high-performance devices. Significant efforts have been devoted to developing technologies that allow the implementation of artificial metamaterials compatible with standard manufacturing processes in silicon photonics. Among several possible approaches, the most successful one is based on sub-wavelength grating (SWG) structures [27–29]. An SWG is a nanostructured artificial material, also called metamaterial, with optical characteristics determined by its geometry, that, when properly designed, improves device performance. This may include increased efficiency, bandwidth, and polarization handling, while also maintaining compatibility with standard fabrication techniques. Designing appropriate metamaterials for each specific application is the natural approach in academia and, recently, has also been implemented in industrial products.

In this thesis, SWG materials are used for the design of surface-emitting antennas. By leveraging new metamaterial structures, we are able to synthesize millimeter-scale antennas ($L > 1000\lambda$) that are compatible with standard manufacturing processes. The Photonics & RF Lab, in collaboration with the National Research Council of Canada (NRC), has conducted pioneering research focused on integrated optical devices using SWG metamaterial structures. These devices include: i) fiber-chip edge and surface grating couplers, ii) high-bandwidth and polarization-insensitive multi-mode interferometers (MMIs) used for

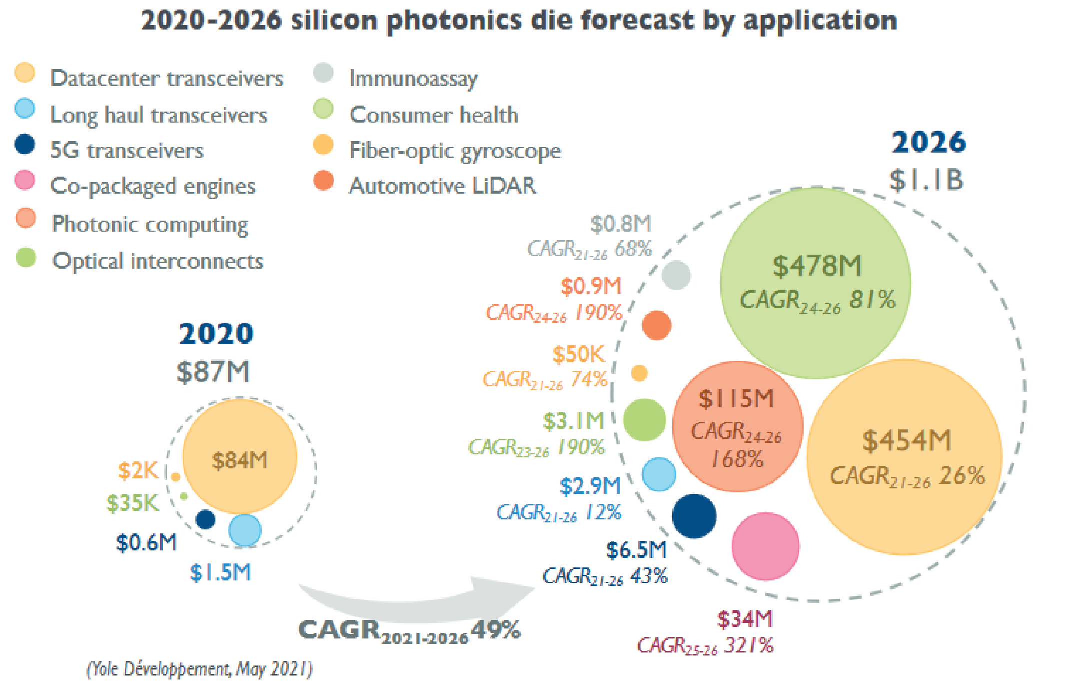

Figure 1.2.: Yole Développement report of Silicon Photonics in the next years. Study of the forecast for the next few years of SiPh chips per application to be manufactured, and the global proportion of money invested in each application. Source of the image [13]

efficient on-chip power splitting or coherent receivers in communications [30, 31], iii) integrated polarization splitters, essential for the proper functioning of conventional integrated optical systems where devices are sensitive to light polarization [32], iv) integrated optical antennas, highly useful in LiDAR and remote metrology by providing the capability to create millimeter-sized antennas with highly directive and steerable optical beams [33], v) metalenses, used in a wide range of applications by enabling on-chip lens functionality [34], and vi) spectral filters, providing efficient wavelength filtering for a variety of applications, including the ability to achieve extremely narrow spectral filters with this type of technology [35].

This Thesis focuses on the integrated optical antennas for the generation and control of highly collimated beams emitted from SiPh chips. Integrated optical antennas are fundamental building blocks for many applications such as optical interconnects, on-chip light detection and ranging (LIDAR), remote sensing, and free-space optical communications. Typically, integrated optical antennas are designed as dielectric gratings with a specific topology to achieve a particular radiation behavior in terms of directivity, radiation direction and angular divergence. Other mechanisms for controlling the emission of optical beams from solid-state antennas include plasmonic nano-antennas [36–38], liquid crystal gratings [39, 40] or emitters controlled by microelectromechanical systems (MEMS) [22, 41].

A solid-state solution that has been gaining traction in recent years is the use of dielectric antennas forming optical phased arrays (OPAs) to emit highly focused beams and electronically manipulate the radiation direction without the need of any mechanical system. Different architectures can be used to implement OPAs, as the one-dimensional arrays (1D-OPAs) [42–47], two-dimensional arrays (2D-OPAs) [48–51], spares arrays [52–54], focal plane arrays [22, 55], circular arrays [56], etc. A significant number of compilation works have been published in recent years, substantiating the growing importance of this technology [57–60].

The two most common architectures used in the state-of-the-art are the 2D-OPAs and the 1D-OPAs (see Fig. 1.3). The main differences between them are as follows: The 2D-OPA typically comprises an array of $N \times N$ antennas arranged uniformly in both transverse (y) and longitudinal (x) directions. As a result, the antennas used in 2D-OPAs are usually short and require high radiation strength. On the other hand, the 1D-OPA consists of an array of antennas grouped only in the transverse direction (y), necessitating weaker antennas with large lengths, usually a few millimeters to emit highly collimated beams. The 2D-OPA allows for manipulation of the radiation pattern in both the vertical and azimuthal directions ($\Delta\theta$, $\Delta\phi$), and enables beam steering towards any desired direction in space (θ_0, ϕ_0) through electronic phase shifting. In comparison, the 1D-OPA requires electronic phase shifting along with wavelength tuning to steer the radiated beam in different directions. 2D-OPAs can achieve beam steering and beam shaping without wavelength tuning, making them advantageous for monochromatic systems such as optical communication links. However, their feeding scheme and phase-shifting mechanism pose high complexity, which grows quadratically with the number of antennas (N^2). 1D-OPAs are a simpler approach with the same potential to radiate highly collimated beams and control the direction of radiation with N phase shifters for N antennas.

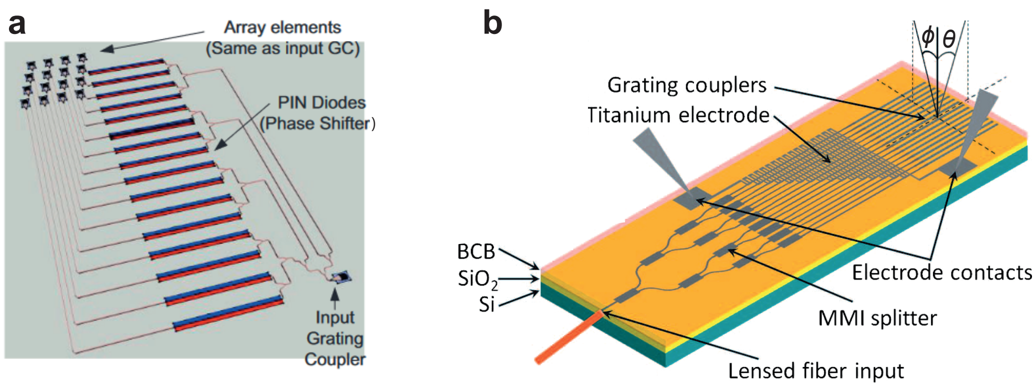

Figure 1.3.: Two main configurations of optical phased arrays (OPAs). a) 2D-OPA composed of 4×4 radiating elements (short gratings with high radiation strength) and 16 phase shifters for steering control [61]. b) 1D-OPA composed of 16 one-dimensional antennas (large gratings with low radiation strength) and 16 phase shifters for azimuthal beam steering (ϕ). Vertical steering (θ) requires wavelength tuning [42].

1.2. Overview of the Thesis

The primary goal of the research conducted in this Thesis is the development of SiPh surface-emitting antennas with millimeter-scale apertures designed for one-dimensional optical phased arrays. In high-contrast silicon-on-insulator waveguides, it is extremely challenging to implement long weakly radiating antennas using impractically small lithographic feature sizes on the order of tens of nanometers [62, 63]. In this work, we demonstrate for the first time a metamaterial antenna in silicon waveguides with lengths of several millimeters. Furthermore, a radically new concept for a 1D-OPA is proposed and experimentally demonstrated. It uses a novel antenna array feeding scheme, based on a distributed Bragg deflector to efficiently radiate steerable collimated beams from silicon photonic chips with a single control element.

The main contributions of this Thesis have resulted in three publications in journals indexed in the Journal Citation Reports (JCR) and six national and international peer-reviewed conferences, four of which the candidate has been the first author. Additionally, the candidate is a co-inventor of a patent related to the topologies for surface-emitting antennas presented in this Thesis. In accordance with the regulations for doctoral studies at the University of Malaga, the above-mentioned publications are proposed to support the presentation of this Thesis as a compendium of publications.

1.2.1. Contributions

All the contributions of the Thesis are summarized in Fig. 1.4, where the main characteristics of each design is briefly presented. Including the publications that endorse this Thesis.

Metamaterial surface-emitting antennas

In this Thesis, a novel topology for the development of weak radiating antennas in high-contrast platforms like SOI is presented. This topology leverages an SWG waveguide core in conjunction with evanescently coupled lateral segments that are arranged periodically along the propagation direction, enabling the radiation of the waveguide mode off-chip. The separation of the lateral segments from the SWG core gives a precise mechanism to control the radiation strength of the antennas. With this innovative approach, millimeter-scale antennas can be designed without being constrained by fabrication limitations, as the minimum feature size of the device can be significantly increased.

Several antenna designs have been developed throughout the Thesis (see Fig. 1.4). These designs include: i) Highly efficient surface-emitting antennas specifically designed for TM polarization (out-of-plane), ii) surface-emitting antennas optimized for TE polarization (in-plane), iii) slow-light surface-emitting antennas specifically tailored for TE polarization (in-plane). Each design possesses distinct characteristics, but all the antennas share a common topology enabling the realization of compact, large-scale antennas on SOI platforms while emitting highly collimated beams with beam divergences on the order of $\Delta\theta = 0.2°$ or lower. Most of the ideas developed in this Thesis have been successfully demonstrated experimentally with a satisfactory agreement with the modeling and simulation results.

Metamaterial antenna array fed by distributed Bragg deflector (DBD)

The final goal of the research conducted within this Thesis involved the development and experimental evaluation of a complete functional 1D-OPA, as a proof of concept. An antenna array comprising 112 metamaterial surface-emitting antennas was designed and fabricated. It presented a directivity of 53 dBi with a Gaussian far-field spot and an angular divergence of 0.2° × 1.8°. Moreover, the 1D-OPA included a novel feeding scheme using a distributed Bragg deflector (DBD) beam expander. This configuration enables beam shaping in the far-field region and beam scanning using a single control element, as opposed to conventional OPA architectures where a phase shifter is needed for each antenna in the array. The OPA was successfully fabricated and experimentally evaluated.

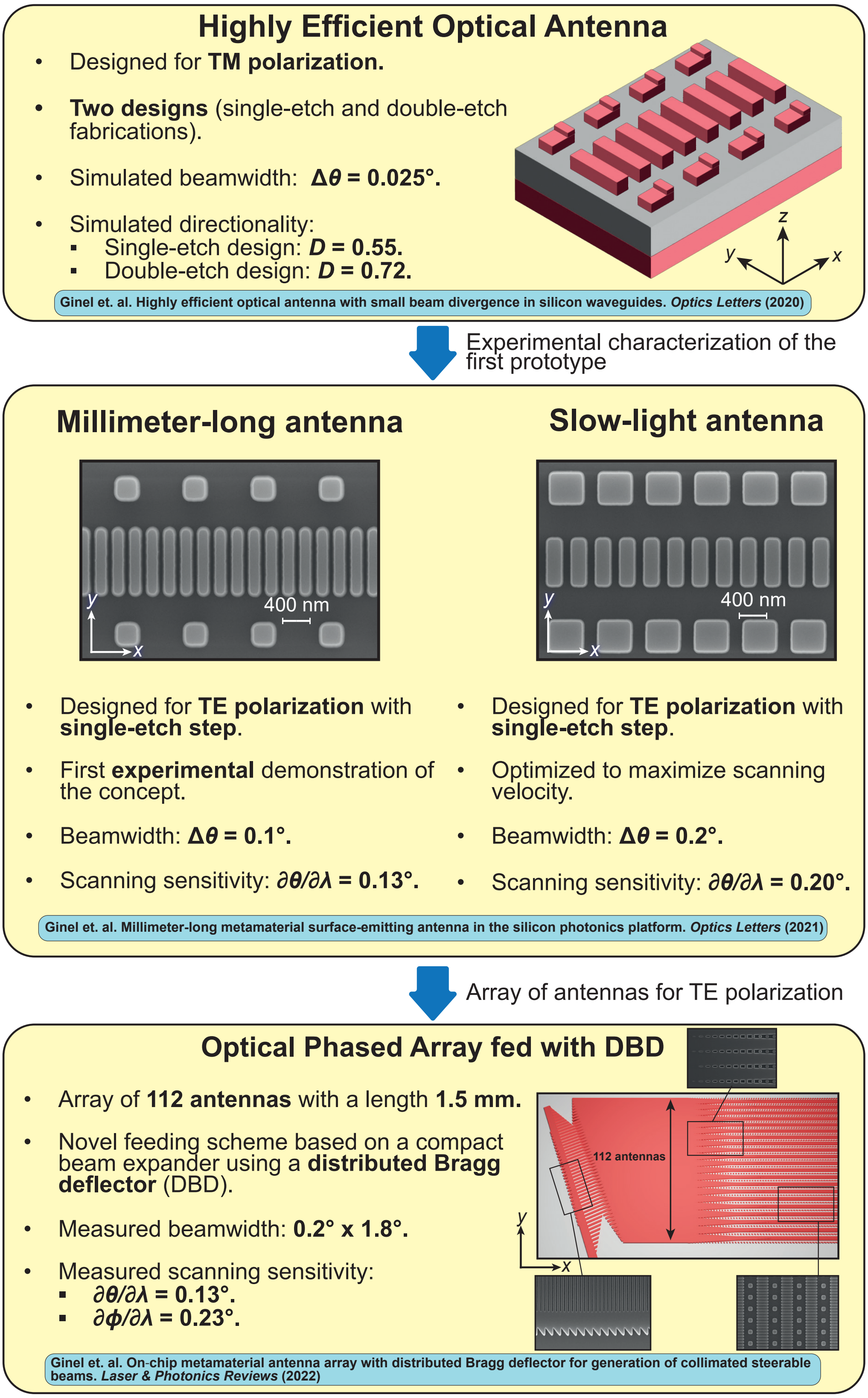

Figure 1.4.: Overview of the contributions presented in this Thesis.

1.2.2. Methods

Development of numerical tools for the design of optical antennas

The design of surface-emitting antennas required specific numerical methods to reduce the simulation time. This is due to the large dimensions of these antennas, which can make electromagnetic simulations computationally unfeasible. Therefore, an important achievement in this work is the development of a Floquet-Bloch analysis tool that can analyze the behavior of the entire antenna without the need to simulate the entire structure. Another significant contribution to reducing simulation time was the development of software methods for calculating the radiation pattern of the antennas. Typically, calculating the far-field distribution requires applying mathematical methods to the near-field data. Traditionally, a simulation of the entire structure is required for this process. One of the goals of this Thesis is the development of a numerical method that leverages the results obtained from the Floquet-Bloch analysis, which simulates a single period of the structure. This method enables the calculation of the radiation pattern of the antennas without the need to compute the entire near-field.

Design and assembly of experimental setups to characterize antennas

Two different setups were designed and built for the characterization of the radiation pattern of the fabricated antennas. The setups comprise an optical lens imaging system and an infrared camera. In the first setup, a single lens is used to observe the far-field radiation pattern and assess the scanning capability of the antenna. The second configuration involves two lenses to achieve a magnification of the far-field radiation pattern, enabling precise measurement of the beamwidth. Using these two configurations, the antenna can be characterized by measuring different figures of merit such as radiation direction, scanning sensitivity, and beam divergence. Both configurations are shown in Fig. 1.5.

1.3. Organization of the Thesis

According to the normative, the Thesis manuscript must include a brief description of the objectives of the Thesis, a summary of the state-of-the-art, a description of methodology aspects not included in the papers, a compilation of the publications as they were published, the conclusions, and the bibliography. These contents are organized within the Thesis manuscript as follows:

Chapter 1 presents an introduction, providing a comprehensive overview of the challenges to be addressed and the contributions and methods presented in the manuscript.

Chapter 2 provides an in-depth discussion of the topic of study and a summary of the state-of-the-art, where all the information about integrated optical antennas is collected. Section 2.1 delves into the fundamental principles of antennas, with a specific focus on two principal aspects of this research: the radiation pattern of antennas and the fundamentals of antenna arrays. In Section 2.2, a review of optical phased arrays is provided, highlighting

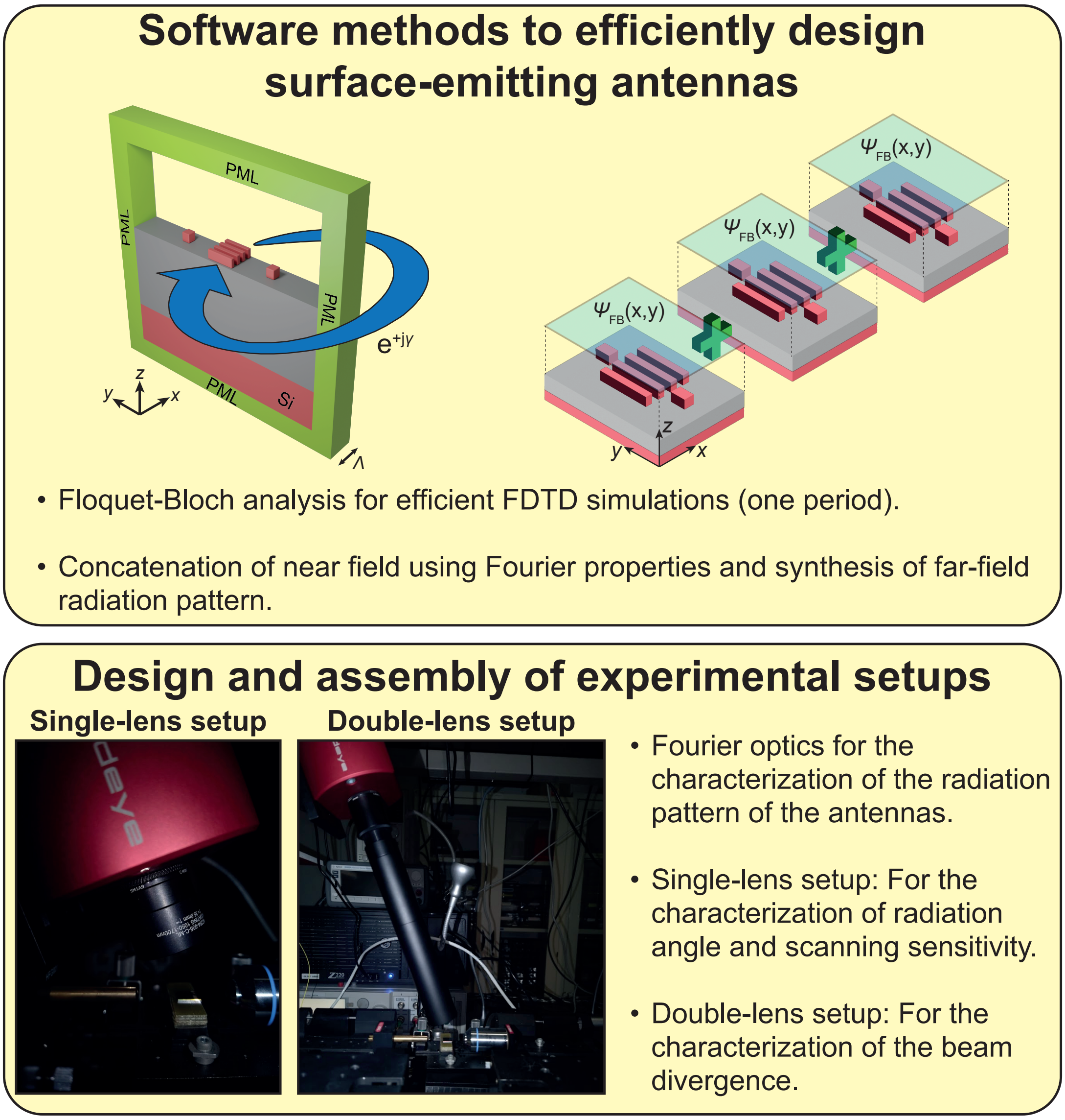

Figure 1.5.: Overview of the methodology of this Thesis. Brief summary of the methods and procedures used for the design and experimental characterization of the different antennas.

their characteristics and emphasizing the architecture studied in this work. Sections 2.3 and 2.4 encompass the physical operation and key parameters that describe integrated optical antennas.

Chapter 3 outlines the methodology employed to undertake the design of surface-emitting antennas. For this purpose, dedicated software tools were developed to efficiently simulate these devices and obtain accurate results substantially faster compared to conventional simulation methods (Section 3.2). Additionally, different experimental setups were designed to facilitate the experimental characterization of the antennas in the laboratory (Section 3.3). Finally, in section 3.4 a complete description of the fabrication mask is presented, listing the different devices which have been prototyped.

Chapter 4 encompasses the published articles that support this Thesis, showcasing the research conducted throughout the work and presenting the results obtained during the research process.

The Thesis ends in **Chapter 5** with the conclusions and prospects for future research.

2. Integrated optical antennas for beam steering applications

2.1. Introduction

The ability to emit highly collimated and steerable light beams from a compact and efficient device is crucial for the development of next-generation optical devices for a wide range of applications, including free-space optical communications (FSO) and optical switching [47, 64–66], quantum processing [67, 68], remote sensing [69, 70], and light detection and ranging (LIDAR) [23, 24, 55, 71, 72].

Optical beam steering can be achieved through a variety of mechanisms. The most commonly used approaches involve utilizing scanning mirrors or active materials and external optics to direct a laser beam in the desired direction. While these solutions are effective, they tend to be bulky and may not be suitable for applications where space is limited. In addition, a mechanical solution is not optimal in terms of performance due to its degradation related to acceleration, temperature, vibration, and inertial forces [58]. The leading commercial applications of integrated optical systems are related to automotive LIDAR, to scan the environment of intelligent vehicles and detect possible obstacles and, Space Optical Communications (SOC). The latter seeks a solution that offers an optical wireless communication (OWC) channel with high data rates, high bandwidth and good security by using optical frequencies to transmit information. Figure 2.1 shows currently deployed LIDAR systems used for the above-mentioned applications. Fig. 2.1.a,b shows the SOTA (Small Optical Transponder) system, a specialized LIDAR for space-based optical communications [73, 74], while Fig. 2.1.c depicts a typical LIDAR system for an autonomous car, backed by camera and RADAR driven systems [75]. In both configurations, it is seen that currently available commercial solutions are bulky and require the support of external optics, mechanical rotation systems and gimbals. For this reason, there is an intense research interest in the search for new beam steering mechanisms that obviate the need for bulky mechanical systems. One promising area of research is the use of integrated optical antennas and optical phased arrays (OPAs), which offer a compact and efficient solution for emitting highly collimated light beams and steering them electronically without the need for mechanical scanning. This solution is typically employed in the radio frequency (RF) field, where the use of phase-coupled antennas to control the steering of the radiation pattern is very common [76].

In the following, a classification of different approaches that are currently being investigated to achieve precise optical beam steering is presented according to the technology used, while all of them share the common feature of being compatible with solid-state systems and employ integrated optical emitters.

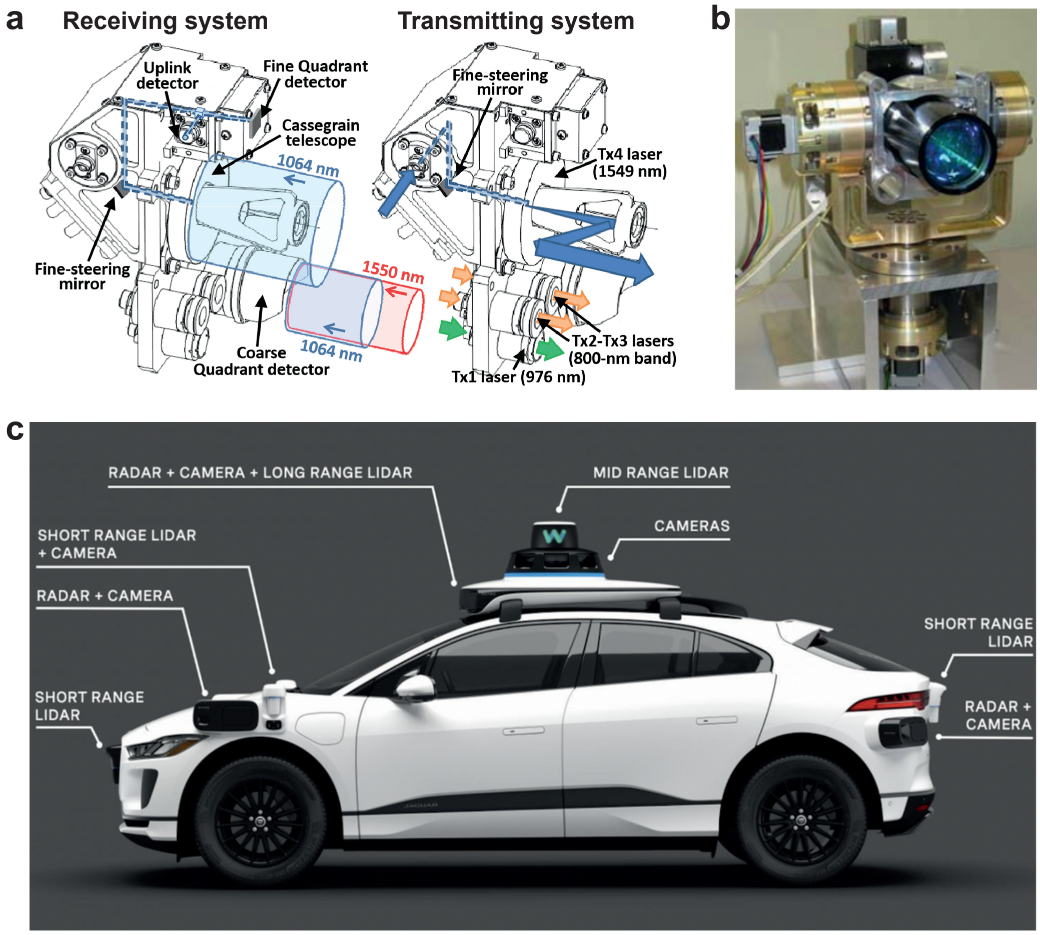

Figure 2.1.: Optical beam steering systems implanted with mechanical elements. a) Receiving and transmitting subsystems onboard SOTA including their main elements as: telescopes, lenses, gimbal systems, rotary motors, mirrors, etc. [74] . b) Photograph of the SOTA system. Total weight of the SOTA is 5.7 kg [73]. c) Schematic of an autonomous LIDAR system developed by OUSTER, INC. [77], a LIDAR company that has recently acquired the VELODYNE LIDAR, INC [78].

2.2. Classification of current approaches

There are various classifications of integrated optical antennas, based on the type of material used, the geometry of the structure, and the fabrication process employed. In the following, we briefly discuss three optical beam steering architectures, compatible with the technology developed in this Thesis.

- **Liquid crystal (LC) based beam steering devices.** This emitter scheme exploits the use of LCs whose state of matter changes through the use of external inputs such as heat, light, electricity, or magnetism [80]. This material is used to form substrates to redirect light to specific directions or as optical elements which allow high-performance beam steering working as gratings, prisms, or lenses [39, 40]. In this way it is possible to redirect the incident light in different directions, achieving real-time beam scanning by using external control. However, this technology has limited energy efficiency, as LCs tend

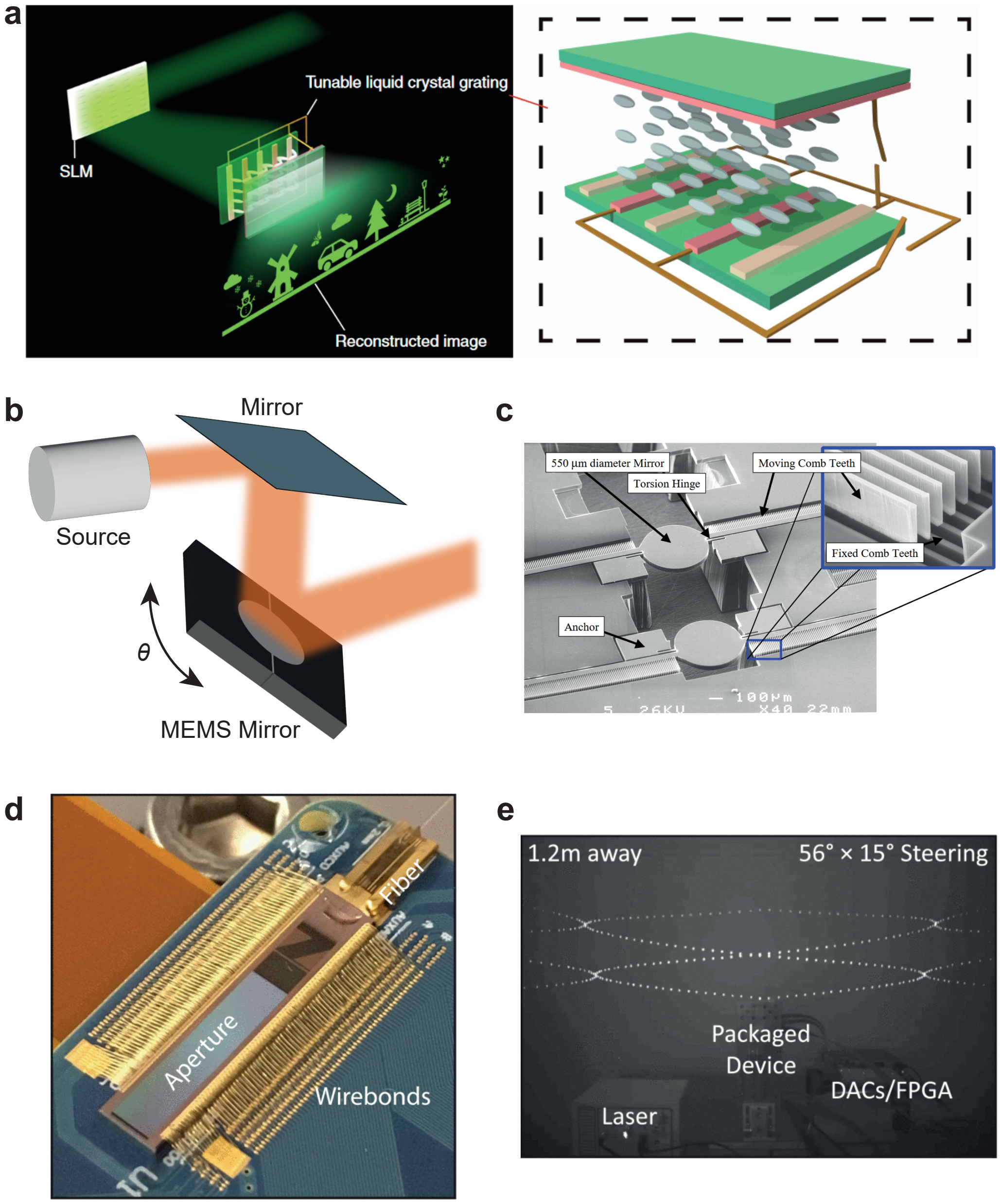

Figure 2.2.: Solid-state solutions for optical beam steering applications. a) Schematic of a holographic 3D display system based on a tunable liquid crystal grating [40], b) a MEMS laser scanner and c) SEM image of [79]. d) A packaged dielectric optical phased array with 512 elements [23]. e) Scanning of the radiated beam direction by electrically controlling the phase shift between the elements of the array [23].

to exhibit high absorption in the IR region ($\eta =\sim 60\,\%$). Furthermore, it is difficult to achieve a continuous scan of the emitted beam without angle discretization, and LCs also have comparably long response times ($\sim 1\,\text{ms}$). Figure 2.2.a shows a schematic of an LC grating working as a holographic system, controlled by external voltage.

- **Microelectromechanical systems (MEMS).** The use of MEMS mirrors to steer the optical beam of a laser or an array of lasers yields highly efficient systems with a large scanning area. However, there is a trade-off between the scanning area, the effective size of the mirror plates, and hence the resonant frequency and velocity of the MEMS mirror [81]. A larger detection area implies using larger mirror plates, decreasing the resonance frequency by having a device with higher mass, thus reducing the scanning speed. The detection area or field of view (FoV) typically achieves ranges from 25° to 180° with millimeter-size mirrors that rotate at frequencies of hundreds of hertz. Figure 2.2.b,c shows a schematic of a MEMS mirror configuration for directing the light from the source, and its SEM image [79]. In addition to using MEMS to move the mirrors, integrated optical circuits are also being used to form integrated optical antennas controlled by mechanical actuators, enabling further integration of mechanically controlled emitters compatible with CMOS fabrication processes [22, 41].

- **Dielectric optical phased arrays (OPAs).** An OPA comprises an array of integrated optical antennas or diffractive gratings, which allows the radiation of highly collimated beams and the steering of the radiation angle in a stable, fast, and precise way without the need for mechanical parts [58]. By achieving full control of the phase and amplitude of the light feeding each antenna in the array, it is possible to control the pointing direction of the radiated beam and perform beam shaping, thus achieving a more complete solution for beam steering applications. However, this is still an emerging technology and some major challenges needs to overcome. These include achieving high radiation efficiency without increasing the complexity of the system, being able to synthesize radiating apertures of the order of millimeters or centimeters to radiate highly collimated beams, and achieving large angular scans without the need to use external optics or mechanical systems. Figure 2.2.d shows a fully integrated LIDAR system with a radiative aperture made by an OPA [23] that can emit a collimated beam with a full-width at half-maximum (FWHM) diffraction angle of less than 0.04° and control its direction in a range of 56° × 15° as shown in Fig. 2.2.e.

  The work carried out here encompasses of the design and fabrication of new types of integrated optical antennas that allow the synthesis of large radiating apertures to achieve the emission of highly collimated beams. A comprehensive study has been conducted, resulting in the successful fabrication and characterization of a new type of OPA. The device is capable of emitting collimated beams with a FWHM divergence of 0.1°. Furthermore, the OPA developed in this study introduces a novel feeding scheme, which provides a compact and efficient solution for the individual feeding of each antenna within the array.

2.3. Antenna fundamentals

One of the fundamental parameters in antenna design is the radiation pattern, which determines how the antenna distributes the emitted power in space and provides important information about the far-field behavior of the antenna and its interaction with a receiver. When multiple antennas are grouped together the radiation pattern undergoes changes, allowing for the modification of the radiation direction by optoelectronic means (phase shifters). This section aims to elucidate the underlying principles governing the behavior and characteristics of antenna radiation patterns.

2.3.1. Radiation pattern of a single antenna

The radiation pattern is a mathematical function or a graphical representation of the radiation properties of the antenna as a function of space coordinates [76]. In most cases, the radiation pattern is determined in the far-field region, sufficiently far away from the radiation source. Figure 2.3.a depicts the angular convention followed in this work to represent the radiation pattern of antennas, using spherical coordinates. Following this angular convention, we consider that the antennas are contained in the XY plane. The radiation pattern can be defined in terms of electromagnetic field or intensity (power).

In the far-field region, also referred to as the Fraunhofer region, the angular divergence of the distribution of the radiated field is independent of the distance from the antenna. The condition is typically satisfied for [76]:

$$R_F > \frac{2D^2}{\lambda}, \tag{2.1}$$

where R_F is the distance from the antenna, D is the antenna size, and λ is the wavelength. Figure 2.3.b shows the variation of the radiated field at different distances, eventually reaching the Fraunhofer region, where the angular divergence is constant with the distance. There are different regions before reaching the Fraunhofer limit. The first is the reactive near-field region, where the radiation pattern is expanded and has a field distribution resembling the near-field. Further away from the antenna, the Fresnel region is found, where some lobes begin to form and the field envelope starts to smooth out. Finally, the Fraunhofer region starts where the main lobe is already well formed and the angular divergence is distance invariant [76]. A schematic representation of the different regions is showed in Fig. 2.3.c.

The calculation of the far field radiated by an integrated optical antenna can be done analytically by using the Fraunhofer transformation [82]. In the field of Fourier optics, a complex monochromatic wave traveling in free space can be decomposed into harmonics with different spatial frequencies, each harmonic corresponding to a plane wave. In the near-field region of an antenna, when the amplitude of the wave is represented in a constant z-plane, it can be decomposed into different plane waves that overlap with each other. At a sufficiently long distance (far-field region, $|\mathbf{r}| > R_F$), they contribute to the total amplitude of each point at the far field as the harmonics of the Fourier transform of the radiated wave. Therefore, the complex amplitude in the far-field region of the wave radiated by an antenna with a physical aperture D in the XY plane can be calculated as a two-dimensional Fourier transform of the near field by using the Fraunhofer diffraction equation [83]:

$$U(\phi,\theta) \propto \mathbf{f}(\phi,\theta) = \iint_D \mathbf{E_a}(x,y)e^{j(k_x x+k_y y)}dxdy, \tag{2.2}$$

where $U(\phi,\theta)$ is the far-field radiation pattern, $\mathbf{f}(\phi,\theta)$ is a complex radiation vector of the antenna, $\mathbf{E_a}$ is the electric field vector in the antenna aperture that only includes the components contained in the constant z-plane, and k_x and k_y are the components of the wave vector, which will be defined in more detail in Section 2.5. The complex vector $\mathbf{f}(\phi,\theta)$ can be resolved to calculate the far-field pattern, and hence the radiation intensity $U(\phi,\theta)$. Appendix A provides a detailed explanation of the procedure for calculating the radiation pattern of an antenna using the complex vector derived from the Fraunhofer equation.

As previously explained, the Fraunhofer diffraction equation represents the two-dimensional Fourier transform of the near field. Consequently, we can apply properties of

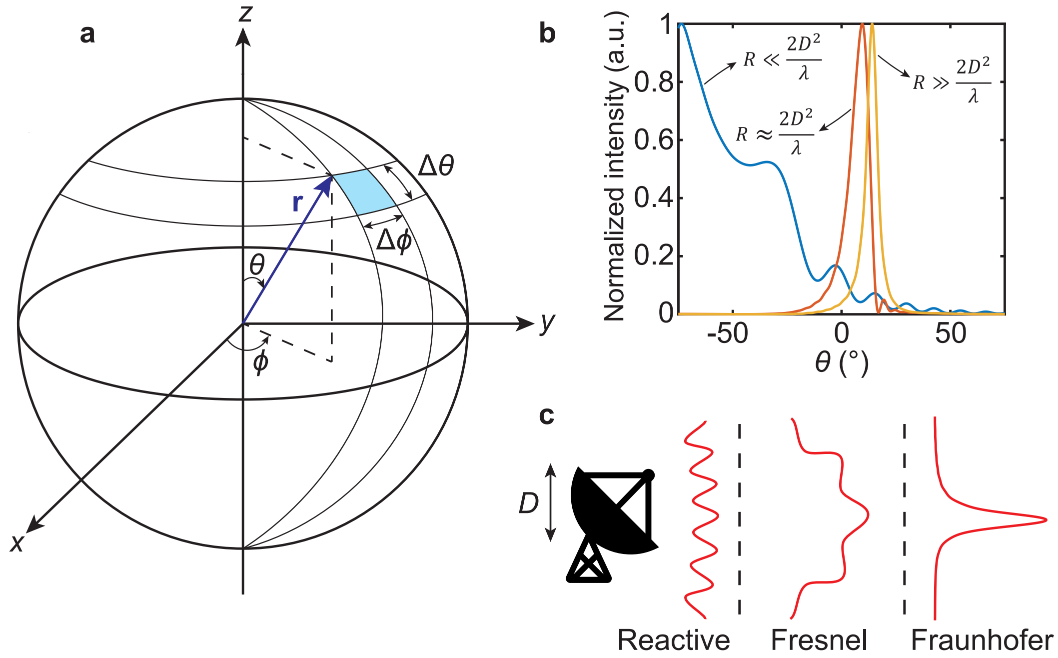

Figure 2.3.: Antenna radiation pattern. a) Coordinate system used in this Thesis for the analysis of antennas. b) Radiation pattern of a waveguide antenna as a function of elevation angle (θ) for a fixed azimuthal angle (ϕ_0) at different diffraction regions. c) Schematic of the different regions that radiated waves evolve trough before reaching the far-field region.

the Fourier transform to analyze the behavior of the radiation pattern. For instance, if an antenna has a large physical aperture in a particular direction of space, the resulting far-field radiation pattern in that same direction will exhibit a narrow beamwidth. This implies that the beam will be collimated in that specific direction. Conversely, when an antenna has a short physical aperture in a given direction of space, the far-field radiation pattern in that direction will feature a wide beamwidth. This indicates that the radiated beam in that direction will be divergent or less directive. These aspects will be of great importance in Section 2.4 when a classification of antennas according to the physical size of their radiating apertures is made.

2.3.2. Antenna array characterization

It is supposed that a given antenna will have an invariant radiation pattern for a given feeding configuration. Under this assumption, the radiated wave will propagate in a particular direction of space (ϕ_0, θ_0) with a specific beamwidth or angular divergence ($\Delta\phi$, $\Delta\theta$). If there is a need to vary the radiation direction of the emitted wave or achieve a more directional radiation pattern, one approach is to create an array of antennas. This involves grouping several antennas of the same type together and allowing them to interfere with each other.

When antennas are uniformly-spaced in a certain dimension and they interfere, the far field radiated by the whole array can be calculated as the product of the far field of a single element of the array $\mathbf{E}_{\text{single}}(\phi,\theta)$ and a new function resulting from the grouping, the array factor $F(\phi,\theta)$, thus the far-field radiation pattern is defined as:

$$\mathbf{E}_{\text{array}}(\phi,\theta) = \mathbf{E}_{\text{single}}(\phi,\theta) \cdot F(\phi,\theta). \tag{2.3}$$

In terms of power, the far field radiation intensity then is calculated as:

$$U_{\text{array}}(\phi,\theta) = U_{\text{single}}(\phi,\theta) \cdot |F(\phi,\theta)|^2, \tag{2.4}$$

showing that the far-field radiation pattern resulting from the array of antennas $U_{\text{array}}(\phi,\theta)$ will be modulated in amplitude by the radiation pattern of a single element of the array $U_{\text{single}}(\phi,\theta)$. Furthermore, the array factor provides the capability to dynamically and electronically modify the radiation pattern of the antenna array in real-time. This feature proves to be highly advantageous and beneficial for numerous applications.

The array factor $F(\phi,\theta)$ is defined as a mathematical function dependent on the complex amplitude of each antenna ($C = |C|e^{-j\varphi}$) and the separation between them inside the array (d). For a generic case in which the grouping is done in two dimensions and there are $N \times M$ antennas, the array factor is defined as follows [76]:

$$F(\phi,\theta) = \sum_{n=0}^{N-1}\sum_{m=0}^{M-1} C_{nm} e^{jk_0(md_x sin(\theta)cos(\phi)+nd_y sin(\theta)sin(\phi))}, \tag{2.5}$$

where k_0 is the wavenumber in the vacuum and the parameters d_x and d_y are the distances between antennas in x direction and y direction. By manipulating the module and phase of the complex amplitude of each antenna, it becomes feasible to alter the array factor, and consequently, engineer the radiation pattern of the antenna in the far-field region.

In this Thesis, the antennas are specifically optimized to form 1D-arrays. Therefore, as the antennas are going to be arrayed in a single direction (y), Eq.2.5 can be abbreviated and the array factor can be defined as:

$$F(\phi,\theta) = \sum_{n=0}^{N-1} C_n e^{jk_0 nd_y sin(\theta)sin(\phi)} = \sum_{n=0}^{N-1} |C_n| e^{jn(k_0 d_y sin(\theta)sin(\phi)-\Delta\varphi)}, \tag{2.6}$$

where $\Delta\varphi$ is the phase shift applied between adjacent antennas. In 1D-arrays to achieve a scanning of the radiated beam without altering the beam shape, the phase shift along the array must be linear. This means that the phase shift between two consecutive antennas must be constant $\Delta\varphi_n = \varphi_{n+1} - \varphi_n = \Delta\varphi$. In antenna theory, there is an interesting parameter to study this type of array known as digital wavenumber (Υ), which defines the phase constant of the array factor [84]:

$$\Upsilon = k_0 d_y sin(\theta) sin(\phi) - \Delta\varphi. \tag{2.7}$$

When this parameter becomes zero, the array factor is maximized. Taking this into account, it is clear that in a 1D-array in which the vertical direction is determined by the single element of the array (θ_0), adjusting the phase shift between adjacent antennas ($\Delta\varphi$) allows the azimuthal direction (ϕ_0) to be controlled to steer the radiation pattern in the desired direction. As mentioned earlier, the complex amplitude of the antennas in the array affects the radiation pattern. However, two other important parameters also influence the array factor: the distance between elements (d_y) and the number of antennas in the array (N). Figure 2.4.a illustrates the radiation pattern of an antenna array and its decomposition into the element pattern and array factor. It is observed that the width of the main lobe beam is inversely proportional to the product $N \times d_y$, indicating that a narrower main lobe is achieved when more antennas are grouped together. Additionally, the distance between antennas (d_y) is inversely proportional to the spacing between the lobes of the array factor. Thus, an increase in the distance between antennas leads to the emergence of more side-lobes near the main lobe. In Figure 2.4.b, the impact of controlling the phase shift between antennas is shown. It can be observed that when the phase shift is controlled, the array factor is displaced, and this displacement can result in the emergence of lateral lobes, known as grating lobes, which are side-lobes that have the same amplitude as the main lobe.

The array factor is a periodic function in Υ with a period 2π and the maximum value can be found at $\Upsilon = m2\pi$, where m is an integer. A representation of the array factor in the Υ domain is shown in Fig. 2.4.c-d. There is a set of Υ values defined as the visible region, which defines the region that is able to scan an array of antennas by modifying the phase shift between adjacent elements of the array. Depending on the size of the visible region, there could appear in the array factor the so-called grating lobes. Therefore, the ratio of wavelength (λ) to element spacing (d), which is included in the digital wavenumber, is important to ensure that no grating lobes appear in the radiation pattern. The most interesting cases are summarized here:

$$kd < \pi \Rightarrow d < \frac{\lambda}{2} \qquad \text{(Grating lobes will never appear)}$$

$$\pi \leq kd < 2\pi \Rightarrow \frac{\lambda}{2} \leq d < \lambda \qquad \text{(Grating lobes may appear)}$$

$$kd \geq 2\pi \Rightarrow d > \lambda \qquad \text{(There will always be grating lobes)}$$

Since the basics related to antenna radiation and antenna arrays have been explained, the following sections will show what types of aperture antennas can be realized on silicon photonics platforms and what is the physical principle behind them.

2.4. Optical phased arrays in silicon photonics

An optical phased array consists of a set of integrated optical antennas. In addition to the antenna array, it is composed of several stages before reaching the emitters, a schematic diagram of all the necessary stages of an OPA is represented in Fig. 2.5. It needs to receive light from a laser source, either integrated in the chip itself or external, using specific devices to couple light into the silicon photonics (SiPh) chip. The first stage is responsible for distributing the power from the laser source into different paths to feed every single emitter of the array. Feeding schemes such as MMI trees, star couplers, or directional couplers are normally used. This stage will grow in complexity as more antennas are added to the array. The next stage is responsible for controlling the phase of the light that will reach each antenna, this can be done on conventional silicon photonics platforms using thermo-optical or electro-optical phase shifters placed over interconnection waveguides. Electronic control is necessary to achieve the required phase shift in each emitter, therefore the optical packaging between SiPh chip and CMOS chip is important in this type of devices. Finally, once the light reaches each emitter that conforms the OPA with a specific phase and amplitude, these radiating elements will radiate light off-chip with a specific radiation pattern,

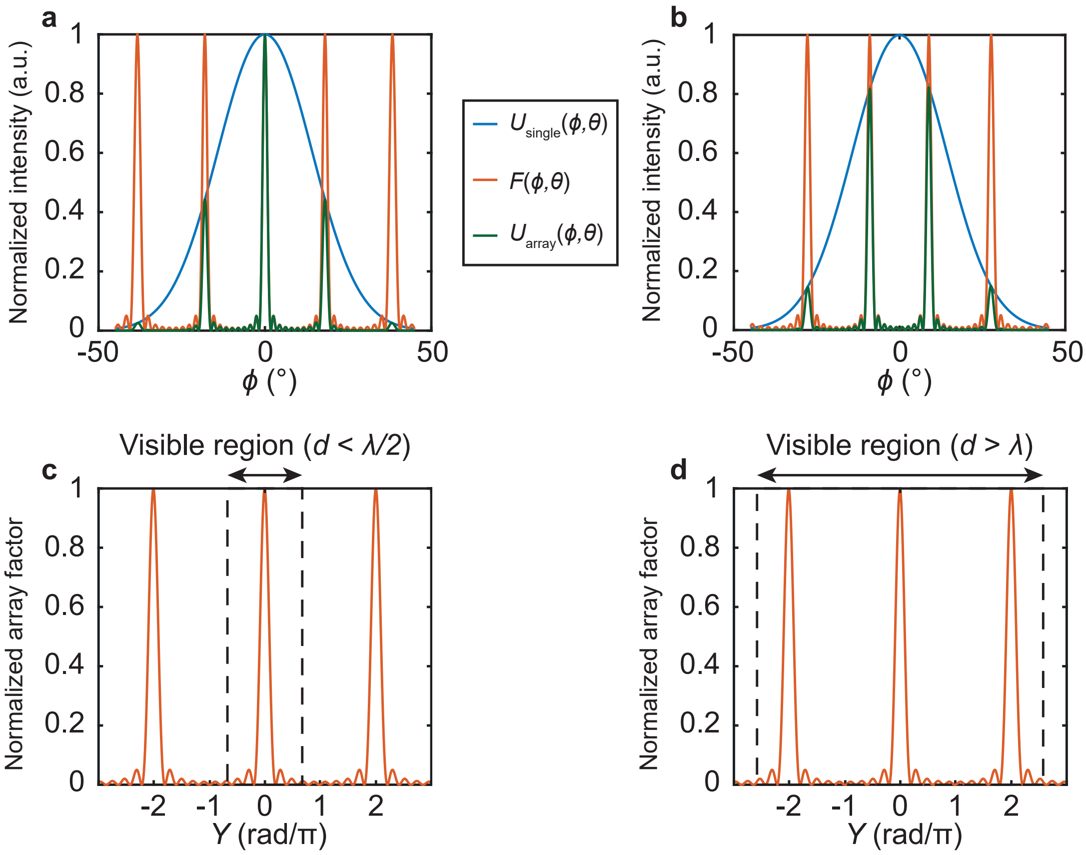

Figure 2.4.: Radiation pattern and its decomposition into the single element radiation pattern and the array factor. The radiation pattern of an array with $N = 10$ elements with a separation $d = 5\lambda$ between them, when a) there is no phase shift between antennas and b) when a phase shift is applied between adjacent antennas. c) The visible region of an array when the distance between elements is less than half the wavelength. In this case, the entire space can be scanned without any grating lobes appearing. d) The visible region of an array when the distance between elements is greater than the wavelength, grating lobes will always be present in the radiation pattern.

depending on their topology. In this Thesis the research is mainly focused on the antenna array block and new solutions for power routing are also studied.

Grouping antennas provides two main advantages, as mentioned in the previous section: first, it enables the steering of the radiated beam through the electronic application of phase shifts between adjacent antennas; second, it offers the possibility to have a large aperture size compared to the operational wavelength, which results in the radiation of highly collimated beams. The characteristics of the radiation pattern of the elements that conforms the OPA depend to a large extent on the topology chosen for its design. In addition, the distribution of these elements in space affect the radiation pattern of the antenna array, as it modifies the array factor. For this reason, there are numerous alternatives for forming an OPA, e.g., sparse arrays [53, 54], circular arrays [56], focal plane arrays [22, 55, 86], etc. However, the two most common architectures used in the state-of-the-art are the ones shown in Fig. 2.6, which in this work are referred as 2D-OPA (Fig. 2.6.a) and 1D-OPA (Fig. 2.6.b).

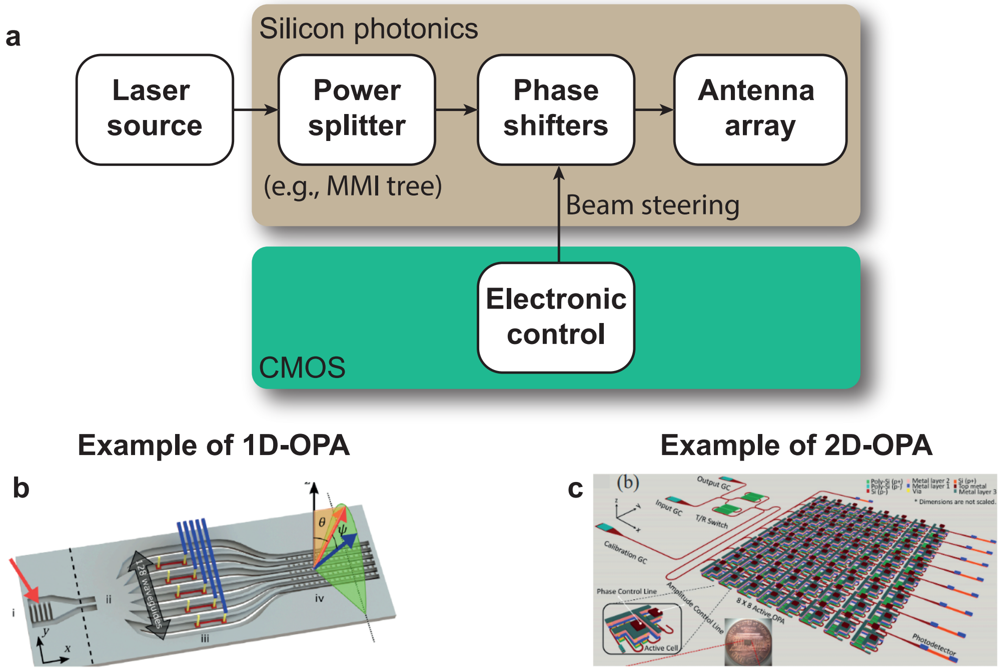

Figure 2.5.: Block diagram of the optical phased arrays architecture. a) Schematic of an OPA with all the necessary stages to implement it. The integration of photonic chips with electronics platforms in a single package is needed to have control of the phase shift between adjacent antennas. b) c) Examples of real implementation of OPAs on the SiPh platform [49, 85].

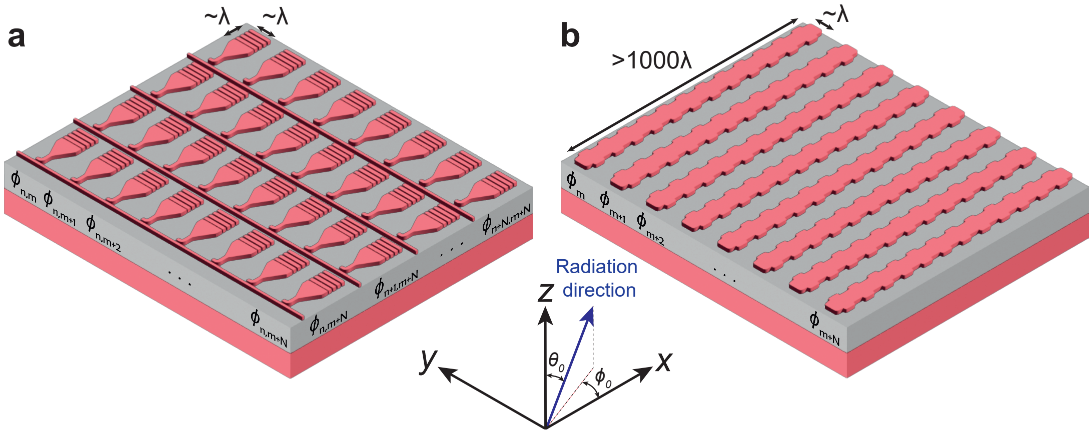

Figure 2.6.: Schematic view of the two main architectures used to implement an integrated OPA in silicon photonics. For the sake of illustration, the top cladding is removed. a) 2D-OPA with N^2 short strong antennas that are arrayed in both longitudinal (x) and transverse (y) direction. For this configuration the control of the phase shift between antennas ($\phi_{n,m}$) permits to scan the azimuthal and vertical angle of the radiation direction (θ_0, ϕ_0), presenting full control of the radiation direction with phase shifts only at the cost of having a complex feeding scheme. b) 1D-OPA with N long weak antennas that extends in the longitudinal direction (x) and are arrayed in the transverse direction (y). For this configuration, the control of the phase shift between antennas (ϕ_m) permits to scan the azimuthal angle of the radiation direction (ϕ_0).

- **A 2D-OPA** comprises an array of antennas arranged in a uniform manner along both transverse (y) and longitudinal (x) directions. It is crucial to maintain small distances between the antennas ($d < \lambda/2$) to prevent the appearance of grating lobes in the radiation pattern. Consequently, the antennas used in 2D-OPAs are typically short and require a high radiation strength [48]. Since the antennas are arranged in two dimensions, the array factor influences the radiation pattern in both vertical and azimuthal directions. By controlling the amplitude and phase shift between adjacent antennas, it becomes possible to manipulate the shape of the radiation pattern in both ($\Delta\phi$, $\Delta\theta$) directions and achieve beam steering towards any desired direction in space (θ_0, ϕ_0). This allows 2D-OPAs working as a monochromatic system (single wavelength), useful for applications in optical wireless communications (OWC) and free-space optical interconnects. Nevertheless, this type of architecture grows quadratically in complexity, as it necessitates N^2 phase shifters for N^2 antennas, which causes the OPA phase shifters and feeding scheme to be extremely complex and space consuming. Furthermore, achieving a 2D-OPA solution without the presence of grating lobes is challenging due to the complexity of the feeding scheme and the sizes of the antennas in conventional silicon photonics (SiPh) technological platforms. Various solutions have been investigated in the literature to address the complexity of the system. For instance, there are approaches proposed for implementing 2D-OPAs with a reduced number of phase shifters, such as using $2N$ phase shifters for N^2 antennas [87]. However, even with these optimizations, complexity remains a significant limiting factor in the design and implementation of 2D-OPAs.

- **A 1D-OPA** is formed by an array of antennas grouped in the transverse direction (y). This architecture tries to simplify the complexity of 2D-OPAs by using only N antennas with N phase shifters. In the same direction of the array (y), the antennas will need to be narrow, to get them closer avoiding grating lobes in the radiation pattern. In the longitudinal direction (x), the antennas will need to have a large length, usually around a few millimeters or thousand of wavelengths ($> 1000\lambda$) to emit highly collimated beams. For this purpose, contrary to the previous case, the antennas must have a low radiation strength to radiate light in more space. Since the phase between antennas is only controllable in the transverse direction (y), the steering mechanism of the radiated beam is different from the 2D-OPAs. In this case, the array factor is only affected by the complex amplitudes of the antennas arrayed in the transverse direction, thus the phase shift between antennas will only control the azimuthal direction (ϕ_0) of the radiatend beam. To achieve a scanning in the vertical direction (θ_0) a wavelength tuning will be necessary. It is crucial for the antennas to be highly sensitive to wavelength variations in order to achieve a large range of steering angles. Therefore, this type of OPA should be used in applications where the wavelength can change without compromising system performance. The effect related to the scanning with a wavelength tuning is will be explained in detail next in Section 2.5.

To be able to radiate highly collimated beams from a 1D-OPA, two main requirements must be met. First, the array should consist of a large number of antennas in the transverse direction. Second, each antenna in the array should be physically large in the longitudinal direction ($L > 1000\lambda$). Achieving a weakly radiating antenna on conventional SiPh platforms such as silicon-on-insulator (SOI), is often complicated. This is because it needs to have periodic perturbations extremely weak. To achieve this, a common approach in SiPh is to use a conventional photonic-wire waveguide to which a lateral modulation is added, as the one shown in Fig. 2.6.b. The lateral modulation is usually very small to achieve very weak antennas, resulting in periodic perturbations with sizes in the order of tens of nannometers [62, 63]. This type of minimum feature sizes (MFS) are only possible with specific lithography processes, not compatible with the immersion deep-UV lithography [88], typical from commercial foundries.

Each solution has its own set of benefits and limitations, making each approach suitable for a specific application. In Table 2.1, a concise overview of the key differences between these two architectures is provided, along with a comparison to the OPA presented in this Thesis. The OPA discussed in this work is a 1D-OPA comprising 112 surface-emitting antennas. It employs a novel feeding scheme based on a distributed Bragg deflector, which enables 2D-beam steering by controlling the phase shift between antennas using a single control element. This design will be explained in more detail in Chapter 4 together with its corresponding publication.

	2D-OPA	**1D-OPA**	**Our proposal**
# of antennas	N^2	N	N
Feeding complexity	Extremely high	High	Medium
Steering in θ	Phase shift	Wavelength tuning	Wavelength tuning
Steering in ϕ	Phase shift	Phase shift	Phase shift / Wavelength tuning
# of phase shifters	N^2	N	1
Antenna size in x	Very short	Very long	Very long
Antenna size in y	Very short	Very short	Short
Grating lobes	Almost always	Avoidable	May appear

Table 2.1.: Comparison between different approaches for OPAs. The proposal presented in this Thesis is a 1D-OPA with a novel feeding scheme that allows 2D-beam steering with only a control element (phase shifter) for N antennas.

2.5. Physical principles of integrated optical antennas

An integrated optical antenna is a type of surface diffraction grating whose topology is optimized to achieve a particular radiation diagram that fits the required application. The surface diffraction grating is a planar device that consists of a sequence of periodically spaced segments distributed along the propagation direction of the fundamental mode (x). The distance between these segments is referred to as the period (Λ) of the grating, and each segment will have a length $a = \mathrm{DC} \cdot \Lambda$, where DC is the duty cycle of the period (see Fig. 2.7). The mode that travels through this periodic structure will be diffracted into a plane wave, propagating through the medium that surrounds the grating and achieving off-chip radiation.

The modes propagating through such devices are different from conventional x-invariant waveguide modes, and, therefore, will have special characteristics that allow the diffraction of light outside the SiPh chip.

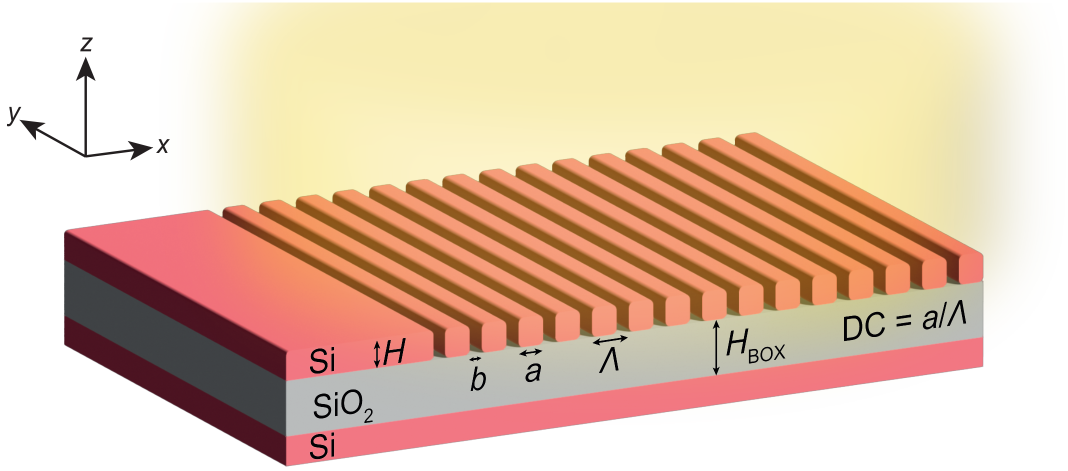

Figure 2.7.: Schematic view of a conventional grating on the silicon-on-insulator (SOI) platform. Surface diffraction grating usually has an invariant geometry in the transverse direction (y). For the sake of illustration, only the silicon layer and substrate together with the bottom oxide (BOX) of thickness H_{BOX} (silicon dioxide) are shown. Each segment that conforms the grating is periodically separated with a period Λ. By controlling the geometry of the segments (DC, etch − depth, Λ) the radiation pattern of the grating can be altered.

2.5.1. Floquet-Bloch modes in periodic structures

Periodic structures support what are called Floquet-Bloch modes, which are the solution of Maxwell's equations for waves propagating in structures with periodic lattices [89]. In a general way, the refractive index of a crystal lattice in dielectric periodic structures can be expressed as a function, as follows:

$$n(\mathbf{r}) = n(\mathbf{r} + \mathbf{R}), \tag{2.8}$$

where $\mathbf{R} = \Lambda_x \hat{\mathbf{x}} + \Lambda_y \hat{\mathbf{y}} + \Lambda_z \hat{\mathbf{z}}$ is the lattice vector, assuming Cartesian coordinates, and represents the periodicity of the structure in each dimension where the structure exhibits periodic behavior. Since in this work, all the periodic structures studied will only have periodicity in the longitudinal direction (x), and hence the lattice vector will only have a single component ($\mathbf{R} = \Lambda\hat{\mathbf{x}}$), all the formulation on Floquet-Bloch modes will be done for the simplified case of periodicity in a single dimension.

Assuming the case of a Floquet-Bloch mode propagating in x direction through a structure periodic in the same direction with a period Λ and an invariant geometry in the y direction, the field distribution of the Floquet-Bloch mode can be expressed as follows:

$$\Psi(x,z) = \Psi_{\text{FB}}(x,z)e^{-jk_x x}, \tag{2.9}$$

where $\Psi_{\text{FB}}(x,z)$ is the mode profile in the XZ plane, because it will be constant in the transverse direction (invariant geometry), and k_x is the only component of the wavevector of the mode. Hereafter, since the modes under study propagate only in the longitudinal direction (x), the wavevector of the modes will have a single component ($\mathbf{k}_{\text{FB}} = k_x\hat{\mathbf{x}}$), hence the wavevector will be defined as a constant (k_{FB}).

An interesting characteristic of the Floquet-Bloch mode, that makes them different from the conventional modes, is that its mode profile is periodic, having the same periodicity as the structure (Λ), proving that:

$$\Psi(x+\Lambda,z) = \Psi_{\mathrm{FB}}(x+\Lambda,z)e^{-jk_{\mathrm{FB}}(x+\Lambda)} = \Psi_{\mathrm{FB}}(x,z)e^{-jk_{\mathrm{FB}}\Lambda}. \tag{2.10}$$

This phenomenon is of great interest since it will enable the mode propagating through the periodic structure to be coupled to a plane wave propagating in space outside the plane of the chip, as it will be explained later. The wavevector of a mode can be defined as:

$$k_{\mathrm{FB}} = k_0 n_{\mathrm{FB}} = \beta_{\mathrm{FB}} - j\alpha_{\mathrm{FB}}, \tag{2.11}$$

where $k_0 = 2\pi/\lambda$ is the wavenumber in the vacuum, n_{FB} is the effective index of the Floquet-Bloch mode, β_{FB} is the phase constant and α_{FB} is the attenuation constant. If the effective index of the mode has a complex term, it causes the attenuation constant (α_{FB}) to appear in the wavevector of the mode. The attenuation constant (α_{FB}) represents all energy losses that the mode experiences through the propagation. Sources of losses can come from many physical phenomena, such as diffraction of the Floquet-Bloch mode itself caused in each segment of the periodic structure, from material losses in the medium through which it travels at a specific wavelength, or even from leakage to the bottom substrate, e.g., when SiPh platforms are used and there is a finite bottom oxide between the grating and the silicon substrate. On the other hand, the phase constant (β_{FB}) describes the phase shift experienced by the mode as it propagates through the periodic medium and is inherent to the mode.

In the following, it will be explained the phase matching condition, which governs the power transfer between a Floquet-Bloch mode and a plane wave traveling through an infinite medium, e.g., the top cladding and bottom substrate surrounding the grating.

2.5.2. Phase matching condition for conventional gratings

A special characteristic of the Floquet-Bloch modes, inherent to their periodicity, is that their field distribution can be represented as a Fourier series expansion of a sum of weighted complex exponentials. Therefore, the Fourier series expansion of the field distribution of a Floquet-Bloch mode can be expressed as:

$$\Psi(x,z) = \left(\sum_{m=-\infty}^{\infty} \Psi_{\mathrm{FB_m}}(z)e^{-j\frac{2\pi}{\Lambda}mx}\right)e^{-j\beta_{\mathrm{FB}}x}e^{-\alpha_{\mathrm{FB}}x}. \tag{2.12}$$

This expression indicates that a Floquet-Bloch mode can be decomposed into a series of infinite harmonics of m-th order. The same attenuation constant that includes all energy losses is used for all the harmonics (α_{FB}), assuming that is equivalent to the partial sum of the attenuation constant of each harmonic [90]. However, each of the infinite harmonics will have a different phase constant defined as:

$$\beta_{\mathrm{FB},m} = \frac{2\pi}{\lambda}Re\{n_{\mathrm{FB}}\} + \frac{2\pi}{\Lambda}m. \tag{2.13}$$

Notice that the phase constant of the Floquet-Bloch mode that travels through the periodic structure (Eq.2.11) corresponds to the phase constant of the 0-th order harmonic ($\beta_{\mathrm{FB}} = \beta_{\mathrm{FB},0}$).In the case of surface diffraction gratings this assumption is very interesting because it lays the foundation of the radiation of light off-chip in a specific direction in space. Each of these harmonics that is radiated out of the grating structure as a plane wave will be known as a diffraction order. The dielectric medium that is around the grating supports the propagation of an infinite continuum of plane waves each radiating to a specific angle in space (θ_0). Each of this plane waves will have a wavevector defined as (see Fig. 2.8.a):

$$\mathbf{k}_{\mathbf{PW}} = k_c sin(\theta)\hat{\boldsymbol{x}} + k_c cos(\theta)\hat{\boldsymbol{z}}, \tag{2.14}$$

where k_c is the wavenumber of a plane wave propagating in a medium with a refractive index n_c. In this case, the wavevector will only have real phase constant, since the dielectric media around the grating is assumed to be lossless. Figure 2.8.a schematically depicts how a periodic structure with a period Λ can radiate the mode propagating through it into the surrounding media. In this case, it can be observed that the grating, which supports a Floquet-Bloch mode with a wavevector $\mathbf{k}_{\mathrm{FB}}$, radiates light into a plane wave with a wavevector $\mathbf{k}_{\mathrm{PW}}$ and the radiated field has an exponential decay as stated in Eq.2.12 . The same effect will occur with the material under the grating, but for better understanding it has been omitted in the figure.

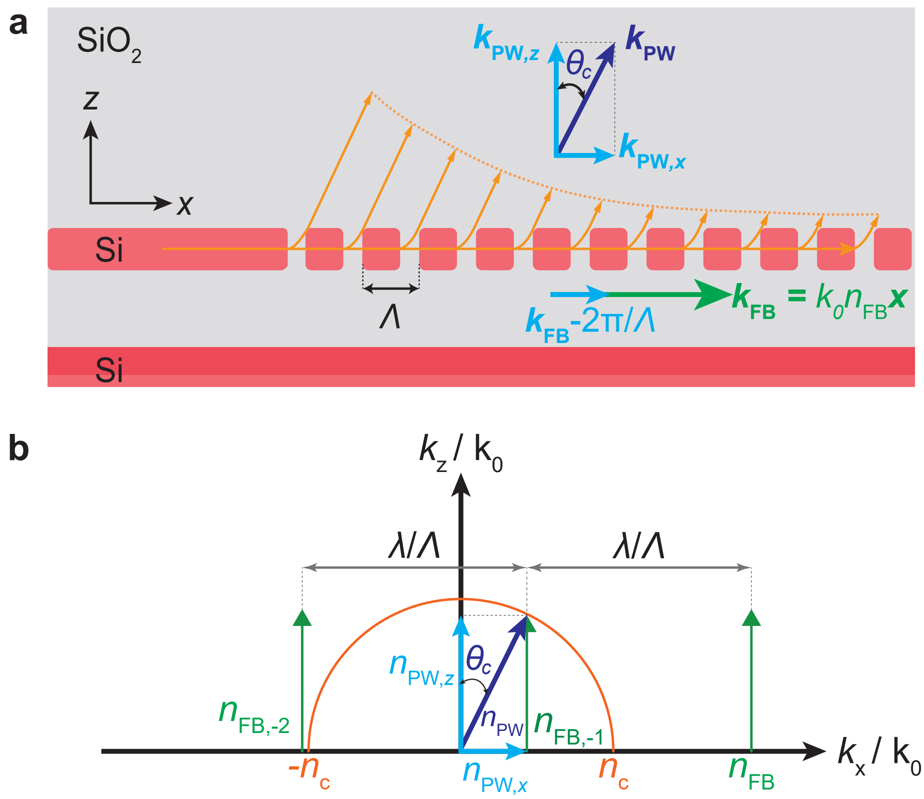

Figure 2.8.: Phase matching condition for 2D-structures. a) Schematic of a conventional planar diffractive grating (side view) radiating exponentially the Floquet-Bloch traveling through it. b) Normalized k-diagram for a problem with an invariant solution in the transverse direction (y). All the m-th harmonics that fall under the semicircle that represent the effective index of a plane wave propagating in a medium with refractive index n_c will be radiated into a plane wave with an angle θ relative to the normal of the chip.

It is said that, the phase matching condition is fulfilled when $\beta_{\mathrm{FB},m} = k_{\mathrm{PW},x}$, the phase constant of any harmonic equals the longitudinal component of the wavevector of a specific plane wave with a radiation angle θ_c, this equality can then be defined as:

$$\frac{2\pi}{\lambda}Re\{n_{\mathrm{FB}}\}+\frac{2\pi}{\Lambda}m=\frac{2\pi}{\lambda}n_c sin(\theta_c). \tag{2.15}$$

In the case of grating couplers and antennas, it is typically desired that only one diffraction order satisfies the phase matching condition. By achieving this condition, all the power can be effectively radiated into a single wave propagating in a specific direction, rather than being distributed among multiple waves. This allows for a more focused and efficient radiation pattern. Additionally, from Eq. 2.15 it can be obtained the grating equation [82]:

$$n_c sin(\theta_c)=Re\{n_{\mathrm{FB}}\}+m\frac{\lambda}{\Lambda}. \tag{2.16}$$

In this equation it can be clearly observed the dependence that exists between the wavelength and the vertical angle of the radiated order. This is why in the case of 1D-OPA, to steer the radiated beam in the vertical direction (θ) it is necessary to tune the wavelength. Also, from Eq.2.16 it can be obtained the condition that the phase constant of a harmonic must satisfy in order to be able to be radiated to the medium with index n_c, which is:

$$|Re\{n_{\mathrm{FB}}\}+m\frac{\lambda}{\Lambda}|\leq n_c. \tag{2.17}$$

Since the real part of the effective index of the propagating mode will always be greater than the refractive index of the material surrounding the periodic structure ($Re\{n_{\mathrm{FB}}\}>n_c$), the diffraction orders must be negative integers ($m=-1,-2,-3,...$). This condition can be easily illustrated with the k-diagram represented in Fig. 2.8.b, which depicts the case of a conventional grating surrounded by a material with a refractive index of n_c. The k-diagram is a mathematical abstraction to easily understand why some harmonics can be radiated as diffraction orders and how their behavior is modified with variations on the period of the structure and the wavelength. For better comprehension, Fig. 2.8.b shows the k-diagram normalized by the vacuum wavenumber (k_0), thus representing exactly the condition of Eq. 2.17. All diffraction orders whose phase constant falls inside the semicircle, of radius n_c, will be radiated to that medium as a plane wave with a specific angle (θ_m). For the sake of clarity, the k-diagram is only shown for the upward radiation of the grating. However, if the phase matching is also satisfied with plane waves in the lower medium, then the grating mode could also be radiated downward. In this case, another k-diagram needs to be drawn to show the diffraction orders in the downward direction.

The antennas that will be studied in the next chapter (Chapter 3) work in a similar way to a conventional surface grating, except that the topology will be designed specifically to achieve certain characteristics. The emitted beam achieved with those antennas will be radiated into a plane wave with a vertical angle dependent on a specific wavelength $\theta(\lambda)$. These antennas will need to be arrayed in one dimension forming a 1D-OPA to achieve scanning in the azimuthal direction by applying phase shifts between the antennas of the array $\phi(\Delta\varphi)$. However, there is an alternative approach to achieve radiating beams in a direction with vertical and azimuthal components without the need to form arrays. This is the use of large surface gratings where the Floquet-Bloch mode that is propagated through them, can do it in an arbitrary direction, different from the longitudinal direction (x) [91]. Therefore, phase matching can be achieved between the Floquet-Bloch mode and a plane wave radiating in a direction (ϕ_0,θ_0). The following section analyzes how phase matching is produced.

2.5.3. Phase matching for large-scale radiative apertures

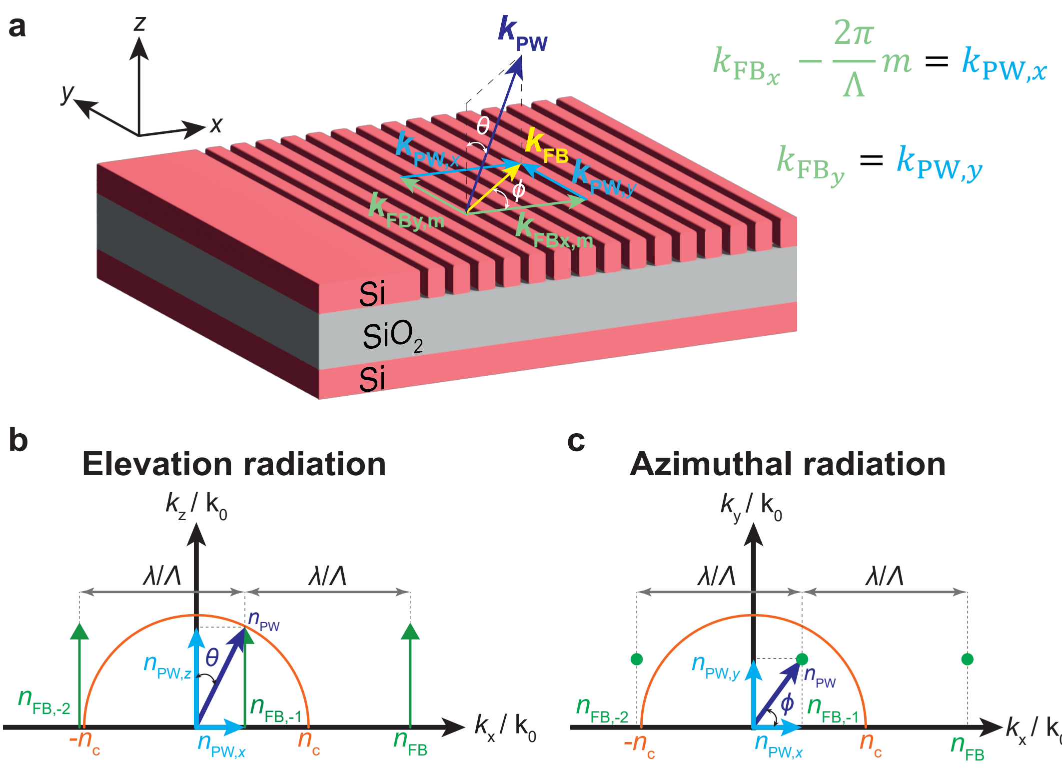

Figure 2.9.: Phase matching condition for large-scale radiative apertures. a) Schematic of a conventional planar diffractive grating (3D view), as the wavevector of the fundamental mode has more than one component, all the possible plane waves that fulfill the phase matching condition can be radiated into the near media with a radiation direction (ϕ_0,θ_0). Normalized k-diagram with two different views: for b) xz plane and c) xy plane. As the structure is only periodic in the longitudinal direction (x) the m-th harmonics of the Floquet-Bloch will be repeated in that direction and no harmonics would appear for the transverse direction (y).

Assuming a conventional grating with periodicity Λ only in the longitudinal direction (x), and a large extension in the transverse direction (y), when an arbitrary Floquet-Bloch mode travels through the periodic medium in a different direction from (x), its wavevector will contain multiple components ($\mathbf{k}_{\text{FB}} = k_{\text{FB},x}\hat{\mathbf{x}} + k_{\text{FB},y}\hat{\mathbf{y}}$), as shown in Fig. 2.9.a. As a result, the direction of propagation of the mode will deviate from the direction of the periodicity of the structure, and depending on its polarization, the mode will perceive the periodic structure as an anisotropic medium. The primary implications are that the phase constant and attenuation constant can have different directions. The former will be determined by the direction of the real part of the wavevector, while the latter will be determined by the direction of the Poynting vector of the propagating mode. Also, another significant outcome of this example is that now the diffraction order can fulfill the phase matching condition with a planewave with both vertical (θ_0) and azimuthal (ϕ_0) components. In the present scenario, to radiate the Floquet-Bloch mode into different plane waves the phase components of the wavevector must be matched ($\beta_{\mathrm{FB},m,x} = k_{\mathrm{PW},x}$ and $\beta_{\mathrm{FB},y} = k_{\mathrm{PW},y}$) as:

$$k_0 Re\{n_{\mathrm{FB},x}\} + m\frac{2\pi}{\Lambda} = k_0 n_c sin(\theta_0) cos(\phi_0), \tag{2.18}$$

$$k_0 Re\{n_{\mathrm{FB},y}\} = k_0 n_c sin(\theta_0) sin(\phi_0). \tag{2.19}$$

The longitudinal component $\beta_{\mathrm{FB},m,x}$ of the phase constant has the possibility of decomposing into harmonics, because it is the only direction where the structure is periodic. In this case we are assuming that the structure is invariant in the transverse direction (y), which implies that the field in that direction cannot be expressed as a Fourier harmonic series. As the propagation direction of the mode is different from x, the effective index can be decomposed as a vector into different directions provided that ${n_{\mathrm{FB}}}^2 = {n_{\mathrm{FB},x}}^2 + {n_{\mathrm{FB},y}}^2$ is satisfied. If we solve the system of equations from above, to calculate the direction of propagation of diffraction orders, the results are the following:

$$tan(\phi_0) = \frac{n_{\mathrm{FB},y}}{n_{\mathrm{FB},x} + m\frac{\lambda}{\Lambda}}, \tag{2.20}$$

$$sin(\theta_0) = \frac{1}{n_c}\sqrt{\left(n_{\mathrm{FB},x} + m\frac{\lambda}{\Lambda}\right)^2 + n_{\mathrm{FB},y}^2}. \tag{2.21}$$

This result yields the general solution of plane waves radiated by a conventional planar diffractive grating for any mode propagating through it in different directions. Whereas the previous case is contained in this result when the wavevector of the Floquet-Bloch mode has no transverse component ($n_{\mathrm{FB},y} = 0$).

The k-diagram in this case can be represented by a semisphere, where the three components of the mode wavevector can be represented. Fig. 2.9.b-c shows the normalized k-diagrams for the last example. Several conclusions can be drawn from this graph: i) As we are using conventional spherical coordinates to indicate the direction of the plane waves radiated out of the grating plane, the semicircle that indicates the radiation zone also represents the azimuthal and vertical angles of the diffraction order depending the position inside of it. ii) If the transverse component of the Floquet-Bloch mode wavevector is sufficiently large, it is possible to frustrate the radiation because the harmonic will go out of the semicircle. It is the same as saying that, if the mode propagates in a direction far away from the periodic axis of the grating, its phase matching may be canceled and therefore it will not be radiated.

2.6. Fundamental parameters of integrated optical antennas

Integrated optical antennas are planar diffraction gratings whose topology is designed to obtain specific performance parameters that fit a required application. As the work of this Thesis is focused on the design of novel topologies to implement antennas for 1D-OPAs, the parameters presented in this section will be adapted for this type of antenna. Each of the following parameters will be related to specific physical parameters dependent on long and weak antennas for 1D-OPAs. The following table attempts to summarize the relationship between antenna parameters and the physical phenomena that affect them.

Parameter	Antenna	Array
Beamwidth	Radiation strength	Separation and number of antennas
Radiation efficiency	Directionality	x
Scanning sensitivity	$\partial\theta/\partial\lambda$	$\partial\phi/\partial\Delta\varphi$
Field of view	Radiation pattern	Separation between antennas

Table 2.2.: Fundamental parameters of integrated optical antennas and the physical phenomena that affects them. There are two type of physical phenomena, those related to the antennas and those related to the array of antennas. The x means that there is no physical phenomena in relation with the parameter.

2.6.1. Beamwidth

Integrated optical antennas are used in critical applications where the beamwidth of the radiated beam is of great importance. For example, in LIDAR applications it is extremely important to have a high resolution of the emitted beam, sufficient to distinguish two closely spaced objects [58]. Another example where highly collimated beams are necessary is in free space optical communication links where the distances are extremely large, in this case, it is required that the transmitter beam does not expand too much before reaching the receptor, achieving a highly efficient and secure communication link [59].

The beamwidth or angular divergence is usually defined as the angular separation between two points where the radiation pattern drops to a value. There are different definitions of beamwidth depending on the convention followed to measure it. It is common to measure the beamwidth in the far-field radiation pattern at half its maximum value, in these cases, it is called FWHM (full width at half maximum) beamwidth. Another interesting type of definition is the beamwidth measured between the first nulls of the radiation intensity around the main lobe radiated by the antenna, denoted in this case by FNBW (first null beamwidth).

Assuming the case of a 1D-OPA, the beamwidth of the radiated beam in the far-field region can be separated into the two principal planes of the radiation pattern (ϕ and θ). The angular divergence in the vertical direction ($\Delta\theta$) will be affected by the radiation strength of the antenna, and the angular divergence in the azimuthal direction ($\Delta\phi$) will be affected by the number of antennas in the array and the separation between them.

Vertical beamwidth ($\Delta\theta$)

The vertical beamwidth is imposed by the radiation strength of the antennas and the shape of the near field radiated by them. The radiation strength is a parameter that indicates how much power an antenna can radiate per unit of distance traveled by the Floquet-Bloch mode through the aperture. The total radiated power can be determined after the propagation of the Floquet-Bloch mode over a distance L as:

$$P_{rad} = P_{in}[1 - e^{-2\alpha_{FB}L}], \tag{2.22}$$

where P_{rad} is the total radiated power, P_{in} is the input power fed into the antenna, α_{FB} is the attenuation constant of the mode in units of $[mm^{-1}]$ and L is the distance over which the mode has propagated. With the apodization of the antenna periods, it can be obtained arbitrary shapes of the radiated near field. In Fig. 2.10 two different antennas are shown, one with constant perturbations where an exponential field profile is radiated and the other apodized specifically to obtain a Gaussian field profile. According to [92], it is possible to determine the radiation intensity distribution necessary along the structure to create an arbitrary radiated field profile as:

$$\alpha(x) = \frac{B^2(x)}{2\left[A_0^2 - \int_0^x B^2(t)\,dt\right]}. \tag{2.23}$$

In this case the structure is periodic in x direction, A_0 is the electric field of the guided wave at the beginning of the antenna ($x = 0$), and $B(x)$ is the arbitrary field profile radiated by the antenna, normalized as $\int_{-\infty}^{\infty} B^2(t)\,dt) = 1$. For the case of integrated optical antennas for 1D-OPAs, very weak radiation strength is needed to achieve antenna lengths in the order of millimeters.

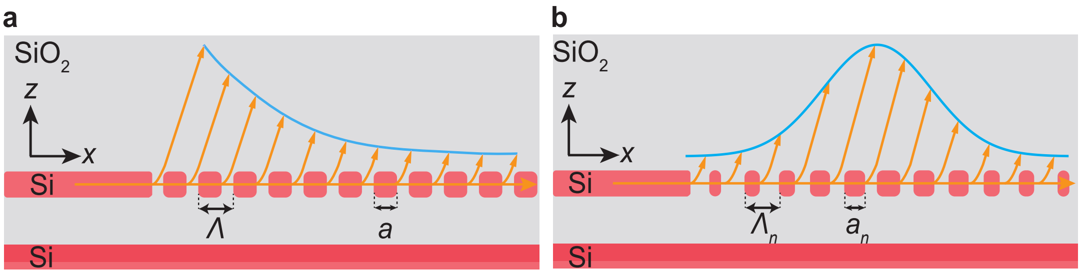

Figure 2.10.: Different apodizations of a surface diffraction grating. a) Uniform planar diffractive grating where the fundamental mode has a constant radiation strength, as the attenuation constant remains the same on each segment. b) Apodized planar diffractive grating where the duty cycle and period of each segment have been designed to modify the attenuation constant of the mode and hence achieve a radiation pattern with a Gaussian shape.

In the case of weak antennas for 1D-OPAs, if we assume that the periodic structure is constant (no apodization is introduced), it will radiate an exponential field profile in the near-field region, thus the far-field intensity will have the shape of a Lorentzian function, i.e., the Fourier transform of an exponential function. The general expression of the far-field radiation intensity in the vertical plane (θ) of an antenna with a length L extending along the propagation axis (x) and a radiation strength (α) which is radiating at an angle θ_0 is:

$$I(\theta) = \frac{1 + e^{-2L\alpha} - 2e^{-L\alpha} cos\left[Lk_0\left(sin(\theta_0) - sin(\theta)\right)\right]}{\alpha^2 + k_0^2\left(sin(\theta_0) - sin(\theta)\right)^2}. \tag{2.24}$$

Assuming that the length of the antenna L is sufficiently large to radiate almost all the power introduced to it ($P_{\mathrm{rad}} > 0.999P_{\mathrm{in}}$), this expression can be simplified, and then the FWHM beamwidth can be calculated approximately as:

$$\mathrm{FWHM}_\theta \approx \frac{2\alpha}{k_0 cos(\theta_0)} = \frac{\lambda}{cos(\theta_0)} \cdot \frac{\alpha}{\pi}. \tag{2.25}$$

This result corresponds to the scenario where a periodic structure with an exponential near-field profile. However, there are additional interesting cases in which the antenna periods can be apodized to achieve different beam divergences in the far-field radiation pattern. Two particularly interesting cases are as follows: i) Apodization of the antenna periods to

	Vertical beam divergence ($\Delta\theta$)
Exponential	$\frac{\lambda}{cos(\theta_0)} \cdot \frac{1.1}{L}$.
Uniform	$\frac{\lambda}{cos(\theta_0)} \cdot \frac{0.886}{L}$.
Gaussian	$\frac{\lambda}{cos(\theta_0)} \cdot \frac{1.5}{L}$.

Table 2.3.: Vertical beam divergence ($\Delta\theta$) for different aperture radiations. For the case of an exponential near-field profile the antenna radiates the 99.9% of the input power after propagating the length L. For the case of the Gaussian near-field profile the length of the antenna is assumed 4 times the beam waist radius $L = 4w_0$.

achieve uniform power radiation along the structure, resulting in a radiation pattern with a sinc distribution. ii) Apodization of the antenna periods to achieve power radiation with a Gaussian profile, leading to a far-field radiation pattern characterized by a Gaussian profile. For each of these cases, the FWHM beam divergence in the far-field region has been calculated and is presented in Table 2.3.

The beam divergences can be compared for the same antenna length. In the non-apodized case with a near field with exponential decay the attenuation constant (α) is selected to radiate the 99.9% of the input power over an antenna length L. While in the case of Gaussian radiation, the antenna length is estimated to be 4 times the beam waist radius of the Gaussian pulse ($L = 4w_0$). In conclusion, it can be determined that the uniform distribution of the field yields the narrowest beam in the far field. However, it is important to note that designing the apodization for extremely long structures can become complex.

Azimuthal beamwidth ($\Delta\phi$)

When antennas are grouped in a specific dimension, the beamwidth in that dimension will be collimated, due to the effect of the array factor in the radiation pattern of the whole system. When all antennas are fed with the same amplitude (uniform array), which is a typical solution in state-of-the-art [45, 62, 63], the FWHM beamwidth of the radiation pattern can be estimated as:

$$\text{FWHM}_\phi = 0.886\frac{\lambda}{cos(\theta_0)dN}, \tag{2.26}$$

where λ is the wavelength, d is the separation between antennas, N is the number of antennas and the term $cos(\theta_0)$ is an obliquity factor, necessary when the radiation is not normal to the plane of the aperture in the same direction of the array. This result is the same as mentioned earlier for apodized antennas that achieves uniform radiation, except that in this case the aperture size is $N \cdot d$. In this case, the Eq.2.26 defines the FWHM beamwidth for an OPA of antennas arrayed in the transverse direction (y), which is why the affected beamwidth is in the azimuthal direction (ϕ). If the amplitude of each antenna in the OPA is arbitrary, then the Fourier transform of the near field is needed to estimate the beamwidth of the far-field emitted beam. In the third publication presented in this Thesis (Chapter 4) a theoretical formula is presented for the estimation of the beamwidth of a beam radiated by an OPA with a Gaussian illumination of the antennas.

2.6.2. Radiation efficiency

The radiation efficiency is defined as the ratio of the total power radiated by the antenna in the desired direction to the total radiated power, and is directly related to the topology of the antenna. The parameter that controls the quantity of power radiated out of the chip compared to the power radiated to other directions is called directionality. For the case of on-chip planar diffractive antennas, the directionality is defined as:

$$D = \frac{P_{\mathrm{up}}}{P_{\mathrm{up}} + P_{\mathrm{down}} + P_{\mathrm{left}} + P_{\mathrm{right}}}, \tag{2.27}$$

where P_{up} is the fraction of power radiated off-chip into the air, P_{down} is the fraction of power radiated to the substrate, and P_{left} and P_{right} are the fractions of power radiated to the sides, usually very small. Figure 2.11.a-b shows schematically how the power is radiated in a conventional surface grating. Conventionally in a symmetrical structure where the cladding material and the bottom oxide (BOX) are the same material, the antenna would have a directionality of $D = 0.5$. However, in the lower substrate, there are reflections that can constructively or destructively sum to the power that is radiated upwards (see Fig. 2.11.a). Therefore, in geometries where there is a symmetry around the antenna, the directionality will oscillate around 0.5.

One of the most commonly used techniques for the optimization of directionality is the use of etching techniques. Etching techniques are a commonly used method to optimize directionality. This technique involves breaking the vertical symmetry of the antenna's geometry to take advantage of the "blaze effect" of the blazed grating [93]. Blazed gratings are a specific type of grating with perturbations with a sawtooth shape that maximizes radiation efficiency towards the desired direction of radiation (see Fig. 2.11.c). Nevertheless, this technique complicates the fabrication process, so echelle gratings are used [94, 95], which are the discretization of the sawtooth with several levels. The first publication that endorses this Thesis (Chapter 4) includes a detailed study of an antenna with two etch-steps, achieving directionalities over 0.7 on a silicon-on-insulator platform.

2.6.3. Scanning sensitivity

The scanning sensitivity is a much more widely used parameter for 1D-OPA antenna design. It indicates the ratio between an angular shift in the direction of radiation of the main lobe and the minimum necessary change in the parameter used to perform the scan. For the case of surface diffractive gratings, where the vertical radiation angle is controlled with a wavelength tuning ($\theta_0(\lambda)$), the scanning sensitivity can be estimated from the grating equation (Eq.2.16):

$$\frac{\partial\theta}{\partial\lambda} = \frac{1}{n_{\mathrm{c}} cos(\theta_0)}\left[\frac{\partial n_{\mathrm{FB}}}{\partial\lambda} - \frac{1}{\Lambda} - \frac{\partial n_{\mathrm{c}}}{\partial\lambda} sin(\theta_0)\right] \sim \frac{1}{n_{\mathrm{c}} cos(\theta_0)}\left[\frac{\partial n_{\mathrm{FB}}}{\partial\lambda} - \frac{1}{\Lambda}\right]. \tag{2.28}$$

As can be observed, the variation of the vertical angle depends on the pointing angle (θ), the Floquet-Bloch mode dispersion ($\partial n_{\mathrm{FB}}/\partial\lambda$), the period of the structure (Λ), and the dis-

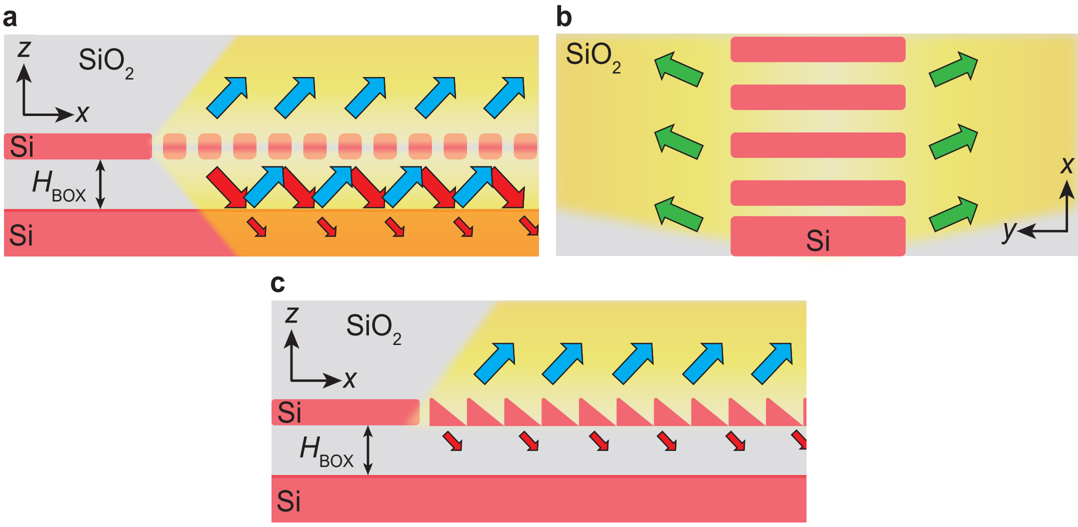

Figure 2.11.: Radiation directionality of gratings in SOI. a), b) Schematic of how a planar integrated antenna radiates. The blue color represents the power radiated upwards, the red color the power radiated downwards and the green color represents the power radiated to the left and right of the structure. c) A blazed grating design optimized to achieve constructive interference in the upwards direction.

persion of the material medium to which the light is radiated ($\partial n_c/\partial\lambda$), which is usually not taken into account since it is orders of magnitude smaller than the rest of the terms.

There are some mechanisms to achieve large variations of the vertical angle scan with small wavelength tuning. One is directly related to the direction of radiation of the main lobe in the vertical direction (θ_0). If the antenna radiates far away from the normal to the plane where the aperture is placed, the variation of the vertical angle is amplified [62, 63]. Another technique, which is widely used with the so-called slow-light antennas [96–98], exploits the use of diverse topologies to achieve Floquet-Bloch modes with a large group index and thus amplify the scanning sensitivity since the dispersion of the effective mode index is related to the group index as:

$$n_g = n_{\mathrm{FB}} - \lambda\frac{\partial n_{\mathrm{FB}}}{\partial\lambda}, \tag{2.29}$$

where n_g is the group index of the mode. Because of this, antennas designed for 1D-OPA have a higher scanning sensitivity for in-plane (TE) polarization than for out-plane (TM) polarization. If Eq. 2.29 is inserted in Eq. 2.28, it is obtained that:

$$\frac{\partial\theta}{\partial\lambda} = \frac{1}{n_c cos(\theta)}\left[\frac{n_{\mathrm{FB}} - n_g}{\lambda} - \frac{1}{\Lambda}\right], \tag{2.30}$$

where the group index is directly proportional to the scanning sensitivity, thus the higher the group index, the greater the sensitivity to wavelength variations.

Weak antennas in SOI platform usually presents scanning sensitivities of $\sim 0.15°/nm$ [58], except some works that presents higher numbers, radiating at large angles ($\theta_0 > 45°$) [62] or using topologies for slow-light antennas. In Chapter 4 we will present a slow light antenna design that takes advantage of the use of metamaterials, demonstrating a scanning sensitivity double that of conventional antennas. It was designed within the framework of this Thesis despite not appearing in any of the publications that support this work.

The scanning sensitivity can also be defined for the tuning in the azimuthal direction. It will be measured as the quantity of azimuthal angle that the beam is steered when the phase shift between antennas changes. From Eq.2.7 the azimuthal scanning sensitivity can be calculated as:

$$\frac{\partial \phi}{\partial \Delta \varphi} = \frac{1}{k_0 d sin(\theta) cos(\phi)}. \tag{2.31}$$

2.6.4. Field of View (FoV)

The field of view represents the whole area where the main lobe can be scanned without any interference from other grating lobes of the radiation pattern. In the case of an OPA with a distance between elements that achieves no grating lobes in the far-field radiation pattern ($d < \lambda/2$), then the FoV is the maximum scanning area that the antenna can physically achieve. This area is typically divided into two parts: the vertical FoV and the azimuthal FoV, as schematically illustrated in Fig. 2.12.a. If the radiation pattern has grating lobes, the FoV is defined as the maximum scanning area of the main lobe before a grating lobe enters the radiation area, an example is represented in Fig. 2.12.c. When antennas are arrayed the FoV of the whole radiative aperture can be calculated as [63]:

$$\text{FoV} = \pm asin\left(\frac{\lambda}{2d}\right). \tag{2.32}$$

It will only estimate the FoV in the same dimension as the array grouping, i.e., if the antennas are only arranged in the transverse (y) direction, as in the case of 1D-OPAs, Eq.2.32 will indicate the azimuthal FoV (FoV_ϕ), the vertical FoV (FoV_θ) being then dependent on the wavelength scan and the diffraction orders of the antenna in this case. Eq.2.32 is only valid when the distance between antennas is greater than half the wavelength. The larger the distance between antennas the smaller the FoV would be since a much larger number of grating lobes will appear near the main lobe limiting the scanning range without interference. Table 1 shows the FoV requirements for different applications where optical technology has a large research niche.

Application	Field of view (deg)
Autonomous vehicles (blind spot)	>120
Face recognition	50
Airborne LIDAR	30
Terrestrial robotics	25

Table 2.4.: Field of view required for different LIDAR applications The applications are ordered from the most demanding to the least challenging.

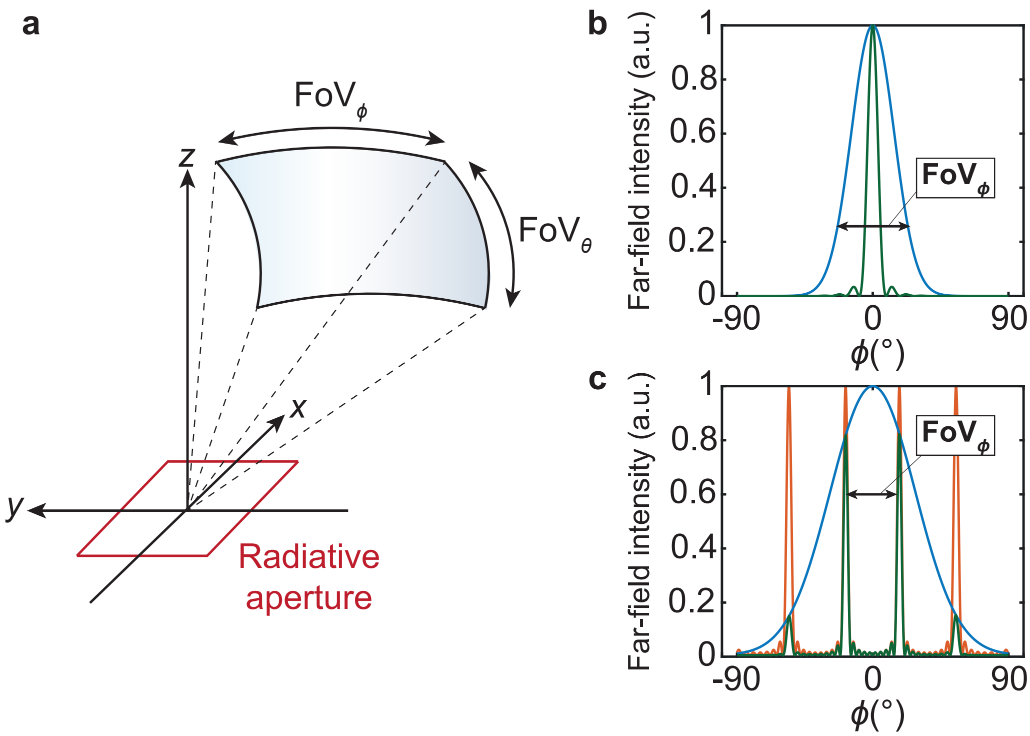

Figure 2.12.: Definition of Field of View (FoV). a) 3D schematic of an aperture radiating at different directions, the area covered by the antenna is the FoV, and it is segmented into azimuthal FoV (FoV$_\phi$) and vertical FoV (FoV$_\theta$). b) Field of view when the antenna array does not present grating lobes ($d < \lambda/2$). In this case the FoV will be the convention of the user's choice, usually measured as the maximum angle until the amplitude of the main lobe falls below a determined value. c) Field of view when the antenna array presents grating lobes. In this case, it will be measured as the distance between two grating lobes, i.e., the maximum steerable angle before a grating lobe has the same amplitude as the main lobe.

3. Characterization of optical integrated antennas: simulation and experimental methods

Before presenting the publications that supports this thesis, a brief description of the antenna developed during this work will be provided. Furthermore, the simulation method used to accurately calculate the Floquet-Bloch mode supported by the antenna, and the computation of a far-field radiation pattern generated by a millimeter-scale structure, will be explained. Another important section will detail the different lens system configurations designed to characterize the antenna radiation pattern in the laboratory. Additionally, an explanation of the structures fabricated on the chip to validate the simulations will be given. Finally, the topology of the OPA developed during this thesis, including the feeding scheme, will be presented.

3.1. Metamaterial surface emitting antennas

3.1.1. Geometry and basic foundations

As explained in the previous chapter, the antenna developed in the framework of this thesis (see Fig. 3.1), offers several advantages over conventional designs: i) It is compatible with monolayer photonics platforms (SOI, SiN, LNOI,...) using single etch step. This avoids the need for specific fabrication processes. ii) The geometry allows the synthesis of extremely weak antennas (millimeter scale) using large MFS compatible with commercial foundries, hence offering the possibility to be fabricated using deep-UV immersion lithography technology. iii) The use of metamaterial subwavelength gratings (SWG) provides more degrees of freedom in antenna design, e.g., it allows for the synthesis of slow-light antennas that can improve scanning sensitivity ($\partial\theta/\partial\lambda$).

A schematic view of the antenna developed during the Thesis is shown in Fig. 3.1 together with two SEM images of different fabricated prototypes. It consists of a main core where a mode is propagating and a series of lateral segments which are physically separated from the core with a gap (g). The lateral segments are spaced periodically with a period (Λ) in the propagation direction (x), while the core needs to support a propagating mode, in this case by a subwavelength grating waveguide (SWG). The principle of operation of the antenna is based on the interaction between the evanescent field of the mode traveling through the core and the lateral segments. As a result of this interaction, the Floquet-Bloch mode supported by the whole structure is radiated in a diffraction order at an angle θ_m determined by the grating equation (Eq. 2.16).

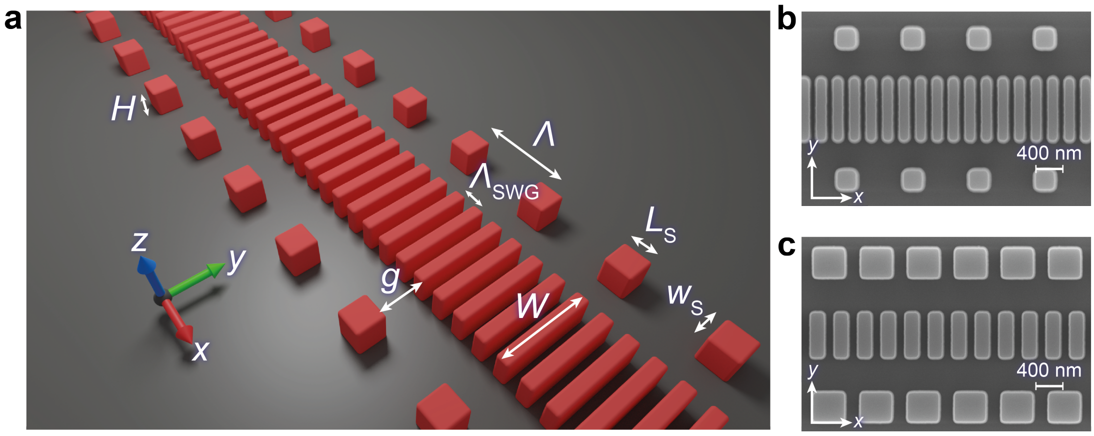

Figure 3.1.: Metamaterial surface-emitting antenna. a) 3D schematic. The design parameters in relation with the antenna are also represented. b) SEM image of the conventional design studied in detail in the second publication of next chapter (Chapter 4). c) SEM image of a slow-light antenna design optimized to achieve an improvement of ×2 in the scanning sensitivity with the wavelength ($\partial\theta/\partial\lambda$).

A subwavelength grating waveguide is a periodic structure that supports the propagation of Floquet-Bloch modes with no losses [27, 28]. To work in the SWG regime the period of the structure must fulfill the following condition:

$$\Lambda_{\mathrm{SWG}} < \frac{\lambda_0}{2n_{\mathrm{FB}}}, \tag{3.1}$$

where λ_0 is the operating wavelength (in vacuum), Λ_{SWG} is the period of the structure and n_{FB} is the effective index of the Floquet-Bloch mode. Therefore, if the period of the metamaterial is below the Bragg condition (Eq. 3.1), it is said that the structure is operating in the SWG regime. In this regime, the periodic waveguide acts as a homogeneous waveguide with an equivalent refractive index (n_{eq}). The effect of homogenization in the SWG regime is schematically shown in Fig. 3.2.a. The properties of the Floquet-Bloch like refractive index and group index can be controlled with the geometry (see Fig. 3.2.b). Also, the use of SWG material allows for precise control over the electromagnetic field distribution of the propagating modes (see Fig. 3.2.c) [29].

The main designs presented in this thesis are focused on the use of SWG metamaterials for the waveguide core to achieve better interaction of the mode field and the lateral segments. Also, the use of an SWG core results in a larger gap size (g) that does not limit the design in the MFS. This type of geometry allows to design antennas with a radiation strength (α_{FB}) extremely low ($\sim 1\,\mathrm{mm}^{-1}$). This phenomenon can be explained by the perturbation theory [99]. Perturbation theory studies how the field distribution, and hence the properties of a mode propagating through a medium change when weak periodic perturbations are introduced in the refractive index of the structure. Applying the perturbation theory to analyze the antenna presented in this thesis, we define the SWG core as an unperturbed waveguide that supports the propagation with no losses of a Floquet-Bloch mode that has a real wavevector $k_u = k_0 n_{\mathrm{FB,u}}$. When it is perturbed, i.e., lateral segments are placed periodically (Λ) and interact with the evanescent field of the mode, the properties of the Floquet-Bloch are affected. The phase constant is modified and losses appear, as the mode fulfills the phase matching condition to be radiated outside the antenna.

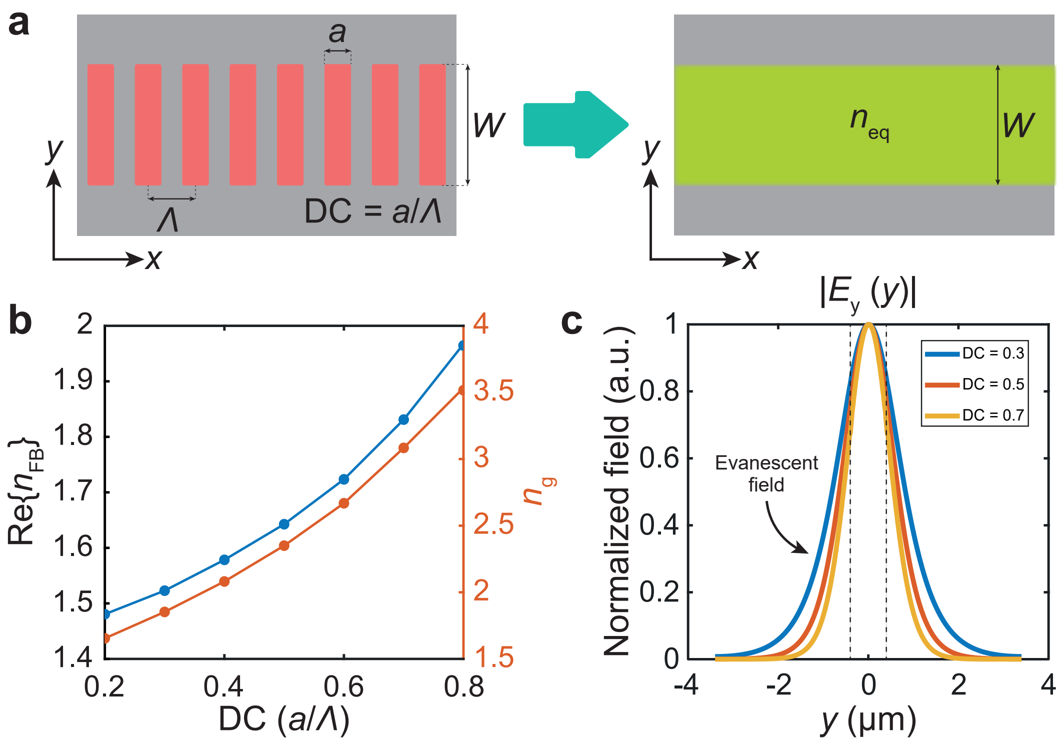

Figure 3.2.: Subwavelength grating metamaterial fundamentals. a) Conventional SWG waveguide (top view) where the mode propagates in the same direction as the periodicity and its equivalent homogeneous metamaterial. b) Refractive index and group index of a Floquet-Bloch mode with TM (out-plane) polarization as the duty cycle of the periods changes. c) Comparison between cross-sectional field distributions of a TM-mode when the duty cycle varies. The dashed lines in the figure represent the transverse limits in the transverse direction of the waveguide (y). It is evident that an SWG metamaterial waveguide enables the engineering of field distribution delocalization of modes, thereby controlling the exponential decay of the evanescent field.

Therefore, the wavevector of the Floquet-Bloch mode can be defined after perturbation as $k_p = \beta_p - j\alpha_p = (k_u + \Delta\beta) - j\alpha_p$. According to perturbation theory, if the perturbations are weak, these two parameters $(\Delta\beta, \alpha_p)$ are directly proportional to the coupling coefficient (κ), defined as [99]:

$$(\Delta\beta, \alpha_p) \propto \kappa = \int_S \Delta\epsilon(y,z)|\mathbf{E}|^2 \mathrm{dS}. \tag{3.2}$$

Here, $\Delta\epsilon(y,z)$ represents the difference in the refractive index between the unperturbed and perturbed structure for a constant x_0 value, and $\mathbf{E}$ corresponds to the field profile of the unperturbed structure. From this equation, several statements can be made. Firstly, the strength of the perturbation increases proportionally with the area of the lateral segment ($W_s \times L_s$), resulting in stronger radiation from the diffracted mode. However, the lateral segments are placed away from the core, in the evanescent field region, where the perturbation becomes extremely weak because $\mathbf{E}$ decays exponentially with the gap (g). Therefore, as the SWG lets to control the mode delocalizaton from the core (Fig. 3.2.c), it enables precise control of the radiation strength.

In the following sections, we will discuss the simulation of a millimeter-scale antenna using the 3D-FDTD (Finite Difference Time Domain) method and the analysis of its far-field radiation characteristics. It is important to note that simulating large-scale structures

($L > 1000\lambda$) using the 3D-FDTD method is not possible due to the high memory requirements. However, we will outline the necessary steps and considerations to ensure an accurate and computationally efficient simulation, by using only the 3D-FDTD simulation of a single period of the antenna.

3.2. Computational design of surface-emitting antennas

3.2.1. Floquet-Bloch analysis

The characterization of long devices ($L > 1000\lambda$) often involves a large computational burden, especially if it is required to measure the performance of a device using the FDTD method in electromagnetic simulations. Running a complete 3D-FDTD simulation of an entire millimeter-scale antenna with a grid resolution of tens of nanometers can be computationally unaffordable. To overcome this limitation, we propose the use of a method that involves simulating a single period of the structure using periodic boundaries with 3D-FDTD simulation. This computational method allows to calculate a Floquet-Bloch mode and analyze the modes in periodic geometries without the need for a complete 3D-FDTD simulation of the entire structure, obtaining the mode profile in a period together with the complex effective index, which will indicate the phase constant (β_{FB}) and attenuation constant (α_{FB}) of the mode, as well as the group index (n_g) at a specific wavelength. The method is based on the theory explained in [100] to calculate band structures in photonic crystals. During this thesis, the Floquet-Bloch analysis method has been programmed in Python to be used together with MEEP [101], an open source package for electromagnetic simulations using the FDTD method, developed by the Massachusetts Institute of Technology.

The method iteratively searches for the Floquet-Bloch mode of a structure propagating at a desired wavelength λ_{end}. It provides at the end of the computation the effective index of the mode $n_{\mathrm{eff}}(\lambda_{\mathrm{end}})$, the group index $n_{\mathrm{g}}(\lambda_{\mathrm{end}})$, and the attenuation constant $\alpha(\lambda_{\mathrm{end}})$ if there are any losses present in the system. To understand how the method works, a list of important elements and required information is provided, offering an efficient way to calculate Floquet-Bloch modes in periodic structures:

- **Simulation cell:** Figure 3.3.a shows a 3D-schematic of the simulation cell of the antenna together with the boundary conditions. The main simulation cell should have a size of a single period Λ in the propagation direction (x). In the other dimensions, the cell should be large enough to contain the calculated mode without reaching the boundary limits. The boundary conditions at the beginning ($x = 0$) and end ($x = \Lambda$) of the simulation cell in the propagation direction must be periodic, which causes the field leaving at one end of the simulation cell to be injected back at the opposite end with a phase shift $e^{j\gamma}$, where $\gamma = (2\pi/\lambda)n_{\mathrm{FB}}\Lambda$. In the other dimensions, the boundary condition will be a perfectly matched layer (PML) to prevent reflections from affecting the simulation.
- **Field monitor:** Before exciting the structure with a source, it is necessary to place a field monitor in the cell that will store the fields during the simulation. It is important not to place the point monitor at or near a node where the fields associated with a mode go to zero because the contribution may be too low, and it may not find the correct mode. Similarly, the component of the field used to measure the field monitor should be the

major component of the mode being analyzed.

- **Source:** The excitation source profile used inside the unit cell (period) must be similar to the field distribution of the modes we want to compute. It is recommended to use a Gaussian pulse in time as excitation, reducing the frequency band of study and making it easier to find the desired resonance (mode).
- **Method starting point:** Before running the FDTD simulation, the method needs a starting point to iteratively reach the mode propagating at the desired wavelength (λ_{end}). The initial guess is an effective index $n_{\text{eff}}^{\text{guess}}$ that will adjust the phase shift of the periodic boundaries to:

$$\gamma_{\text{guess}}^{(0)} = \frac{2\pi}{\lambda_{\text{end}}} n_{\text{eff}}^{(\text{guess})} \Lambda. \tag{3.3}$$

- **Signal processing:** After launching the source and waiting enough time of simulation, the phase shift of the periodic boundaries and the simulated geometry will impose the resonance of several modes, between them one will have a major contribution. The signal stored in the field monitor will be processed with the Filter Diagonalization Method (FDM) [100]. It consists of a spectral analysis of the signal using FFT (Fast Fourier Transform) to determine the resonating frequency of the mode propagating in the cell, and hence the wavelength of the mode found (λ_{reso}). Also, if the mode found exhibits losses, the attenuation constant (α_{reso}) can be calculated with the decay of the field stored in the monitor.

  If the found mode in iteration i, is not resonating at the desired wavelength ($\lambda_{\text{reso}}^{(i)} \neq \lambda_{\text{end}}$), an iterative process begin, where the next value of phase shift imposed in the periodic boundaries ($\gamma_{\text{guess}}^{(i)}$) is the result of a linear regression between the two last results. This iterative method allows to calculate between iterations the variation of the effective index with wavelength, allowing to estimate the group index ($n_g^{(i)}$). An example of the iterative process is schematically shown in Fig. 3.3.b, where three iterations where needed to find the Floquet-Bloch mode at the desired wavelength.

A flow diagram is shown in Fig. 3.3.c where the full method of Floquet-Bloch analysis is explained. The initial effective index is referred to as $n_{\text{eff}}^{(\text{guess})}$, the effective index of the mode resulting from an iteration i is defined as $n_{\text{reso}}^{(i)}$, and the final desired wavelength is λ_{end}.

3.2.2. Far-field computation with FDTD simulation

One of the most crucial properties to analyze in antenna simulation is the far-field radiation pattern. For antennas with physical apertures much larger than the wavelength, the far-field region begins at very long distances (Eq. 2.1). To measure the far-field radiation pattern of a millimeter-scale antenna in simulation using the FDTD method, it is necessary to place a field monitor at distances of several meters, which is computationally infeasible. The Fraunhofer approximation is commonly used in simulation for this reason, obtaining the far-field radiation diagram through a mathematical processing of the measured near field. To do so, it requires simulating the entire antenna to store the whole near field in a field monitor, and then do the Fourier transform processing to obtain the far field. However, for the case of the antennas presented here, it is not a feasible solution as it needs to simulate the entire millimeter-scale antenna and it will require a lot of computational memory. To address this

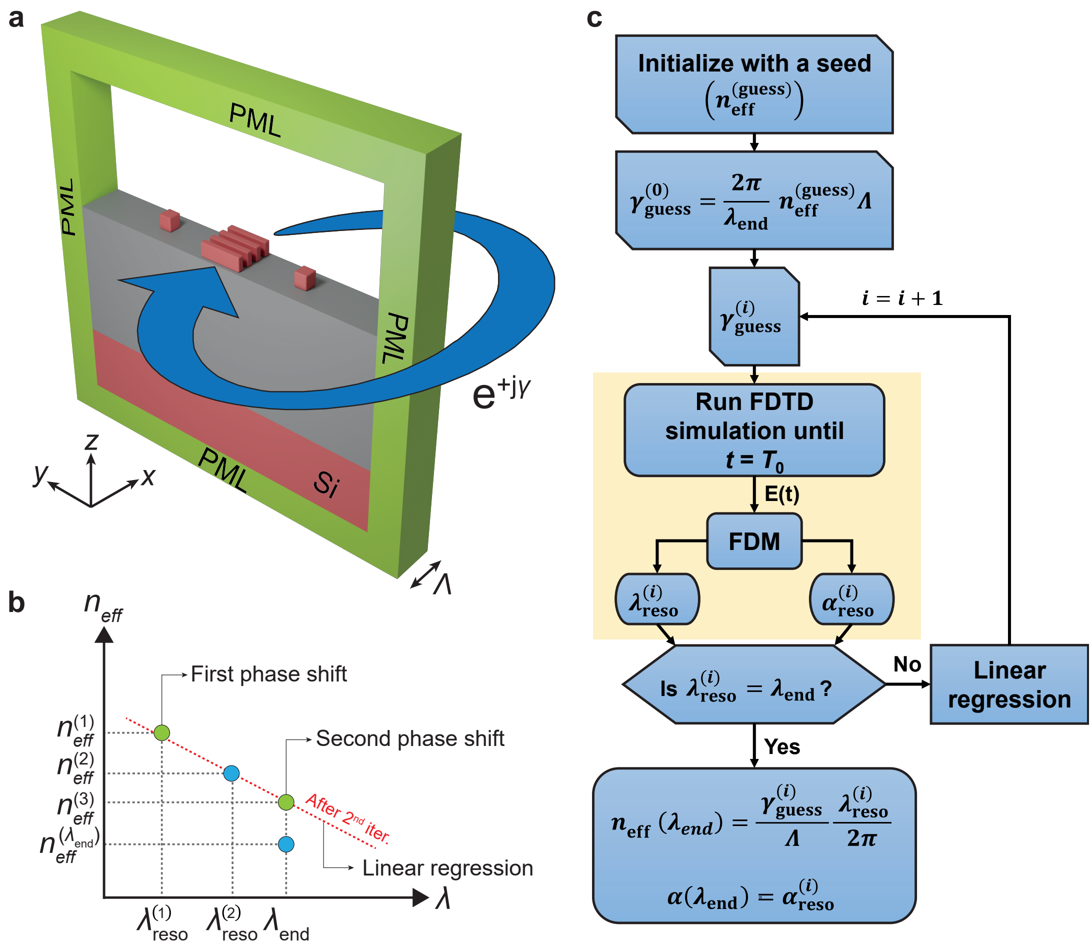

Figure 3.3.: 3D-FDTD Floquet-Bloch analysis. a) Simulation unit cell, with boundary conditions applied in the y and z directions as perfectly matched layers (PMLs) to minimize reflections and their impact on the results. In the x direction, a periodic boundary condition is employed, applying a phase shift $e^{j\gamma}$ to the field that travels thought it. b) Example of the method where three iterations were needed to found the mode at the desired wavelength. The green markers represent the estimated effective index, indicating the step where the phase shift in the periodic boundaries is modified, while the blue markers depict the results obtained from an FDTD simulation. In the first phase shift, the result obtained from the simulation using the initial guess and the phase shift applied to the boundary conditions coincide. Each iteration yields the effective index of a mode resonating at a specific wavelength. The method concludes when the last computed mode resonates at λ_{end}. c) Flux diagram illustrating the step-by-step computational method for Floquet-Bloch analysis.

issue, we developed a mathematical method to construct the near field of a large-scale antenna using the 3D-FDTD simulation of only a single period of the periodic structure. This solution reduce the simulation time from several days to only a few minutes.

For the simulation of a single period of the antenna we use the Floquet-Bloch analysis explained before (Section 3.2.1). While using this iterative method, the near field of the Floquet-Bloch mode is measured by a field monitor placed near the antenna at a distance lower than the wavelength (typically $z = 0.5\,\mu\mathrm{m} - 1\,\mu\mathrm{m}$) occupying the entire simulation cell in the XY plane, a schematic is shown in Fig. 3.4.a. The components of the near field that will participate in the far-field radiation pattern will be those whose direction is included in the plane of the aperture. The near-field distribution captured by the field monitor placed in an XY plane at a certain height from the antenna, is defined as:

$$\Psi_{\text{monitor}}(x,y) = \Psi_{\text{FB}}(x,y)e^{-jkx} = \Psi_{\text{FB}}(x,y)e^{-j(\beta_{\text{FB}}-j\alpha_{\text{FB}})x}. \tag{3.4}$$

The near field of the antenna will have the same field distribution of a Floquet-Bloch mode, with a periodic component $\Psi_{\text{FB}}(x,y)$ and the effect of the complex wavevector $k = \beta_{\text{FB}} - j\alpha_{\text{FB}}$. The first part of the method consists of synthesizing the whole near field of the antenna only with the captured field resulting from the simulation of one period. To do so, it will be important to obtain the periodic component of the near field multiplying the field captured with the monitor by:

$$\Psi_{\text{FB}}(x,y) = \Psi_{\text{monitor}}(x,y)e^{+jkx} = \Psi_{\text{monitor}}(x,y)e^{+j(\beta_{\text{FB}}-j\alpha_{\text{FB}})x}, \tag{3.5}$$

where $\Psi_{\text{monitor}}(x,y)$ is the field distribution of a single period captured by the field monitor and β_{FB} and α_{FB} are the phase constant and attenuation constant obtained with Floquet-Bloch analysis. Once we have the periodic distribution of a single period, it needs to be concatenated as many periods as the antenna has. Assuming that, everything outside the area occupied by the field monitor has a value of zero, the concatenation of the periodic component in N periods can be defined as:

$$\boldsymbol{\Psi}_{\text{periodic}}(x,y) = \sum_{m=0}^{N-1} \left(\boldsymbol{\Psi}_{\text{FB}}(x+m\Lambda,y)\right), \tag{3.6}$$

where N is the number of periods in the antenna and Λ is the period length. Finally, to construct the near field of the antenna ($\boldsymbol{\Psi}_{\text{NF}}$) the effect of the complex wavevector k is applied to the periodic field distribution of the whole antenna:

$$\boldsymbol{\Psi}_{\text{NF}}(x,y) = \boldsymbol{\Psi}_{\text{periodic}}(x,y)e^{-j(\beta_{\text{FB}}-j\alpha_{\text{FB}})x}. \tag{3.7}$$

Finally, in order to calculate the far-field radiation pattern of the antenna, the Fraunhofer integral will be applied to the synthesized near field. By leveraging the Fourier properties and efficiently concatenating the near field in the Fourier domain, the far-field can be obtained through a single period Fourier transform. Applying Fourier properties to Eq.3.7 and developing the integral, the far-field can be expressed as:

$$\mathbf{U}(\phi,\theta) \propto \mathbf{f}(\phi,\theta) = \left(\iint_D \boldsymbol{\Psi}(x,y,z)e^{j(k_x x+k_y y)}dxdy\right)\cdot\left(\sum_{n=0}^{N-1} e^{-n\Lambda[\alpha_{\text{FB}}+jk_0(n_{\text{FB}}-sin(\theta)cos(\phi))]}\right). \tag{3.8}$$

The equation shows the product between the Fourier transform of the near field of a single period of the structure and a factor that symbolizes the effect of grouping different periods in the longitudinal direction (x). The similarity of this equation with the far-field pattern of an array of antennas (Eq.2.4) indicates that this type of periodic antenna can be considered a travelling-wave antenna, which is a very common type of antennas used in telecommunications for radio-frequency (RF), where a travelling mode is emitted by several holes arrayed in the propagation direction.

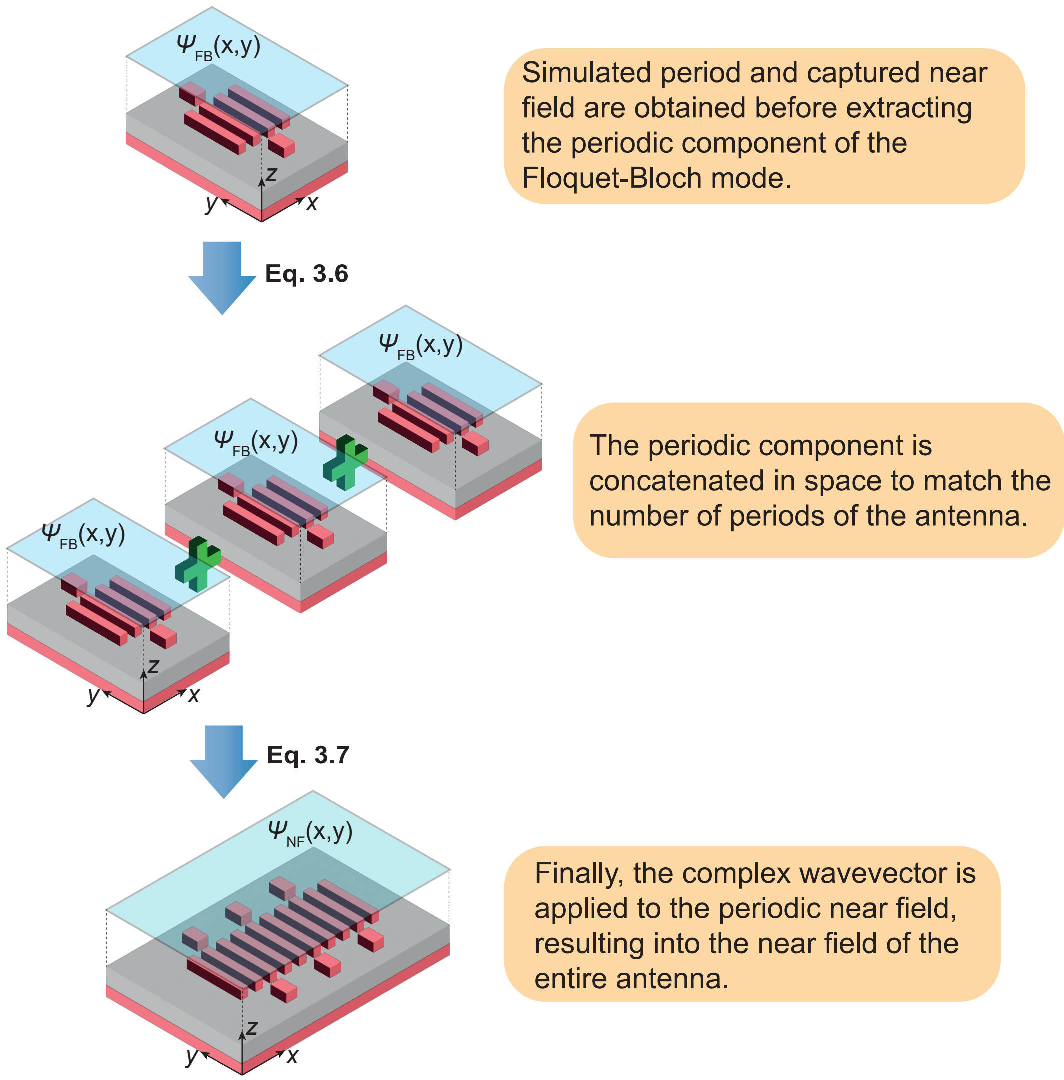

Figure 3.4.: Near-field synthesis method. Schematic of the method of the concatenation of the simulated near field of one period for an antenna of N periods.

3.3. Experimental characterization of the antenna

Over the years, numerous techniques for antenna characterization have been developed, particularly in the RF domain. The main challenge lies in measuring far-field radiation patterns, which are often situated far from the antenna, making it difficult to set up a fully controlled experiment. The three most commonly used techniques in antenna theory for estimating the far-field using near-field measurements are [102]:

1. Using a probe to measure the phase and amplitude of the near field. With this information, the far-field radiation pattern can be estimated through a Fourier transform with post-processing. However, this technique is not applicable in the field of optics since it is not possible to measure the phase of a radiated beam with a probe. Only the amplitude can be measured using infrared (IR) cameras, thus it is not a valid approach for

integrated optical antennas.

2. Generate a quasi-uniform plane wave to feed the aperture at different angles and measure the power obtained by the antenna to be characterized. In the RF domain this technique is tedious due to the size of the plane wave that would have to be generated to characterize large aperture antennas. However, in the field of optics, it is a technique that can be used with a fiber and lenses, where the angle of the fiber with respect to the antenna is very well controlled and it is far enough to create a plane wave that impinges into the integrated antenna [49].

3. The last technique is based on refocusing the antenna radiation to infinity to obtain the far-field radiation pattern in the near-field region. In the RF domain, a parabolic reflector can be used to refocus the radiation diagram placing the antenna under test in the focus of the parabola. This ensures that near the parabola an electromagnetic probe can be used to measure the radiation pattern of the antenna without having to do the measurement in the far-field region. In optics, a similar solution can be achieved by using optical lenses and an IR camera. Optical lenses can project the far-field radiation pattern of an antenna onto their focal plane when the lens captures the near field. To measure the amplitude of the radiation pattern, an IR camera needs to be placed in the focal plane of the lens. A schematic of how the lens works to project the image of the far-field radiation pattern onto the IR camera sensor is shown in Fig. 3.5(b). This approach is simpler than the previous one because a large part of the radiation pattern is projected onto an image, without the need to move the probe at different angles and measure multiple points. An example of the result obtained with this approach is shown in Fig. 3.5.a, where the most important part of the far-field radiation pattern is captured in an single image. Accordingly, this is the approach that has been developed during the thesis for the characterization of the radiation pattern of the fabricated antennas.

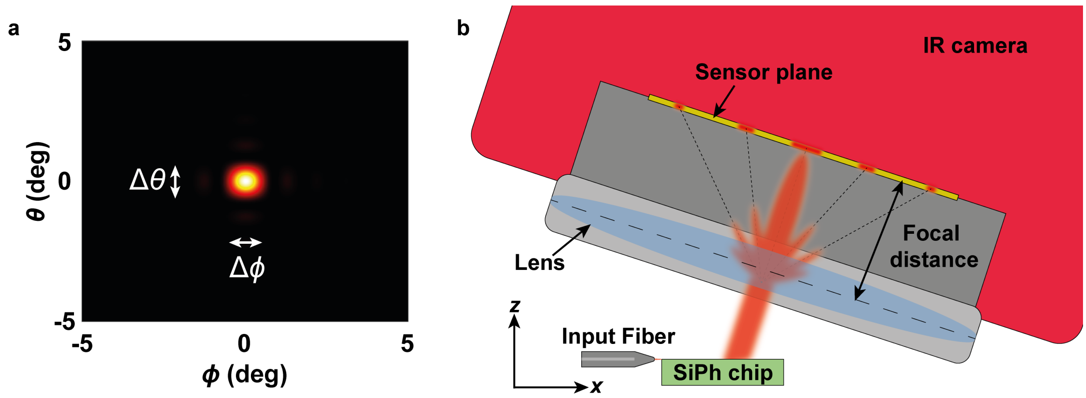

Figure 3.5.: Far-field characterization for integrated optical antennas a) Far-field radiation diagram of a rectangular radiative aperture with a physical size of $100\,\mu m \times 100\,\mu m$ projected into the sensor of the IR camera. b) Schematic of the main approach used in this thesis to characterize the radiation diagram of the fabricated antennas.

3.3.1. Fundamentals of optical lenses

A lens is an optical device made of transparent materials at optical wavelengths that modify the wavefronts of optical beams that impinge on them from one side causing a focus or defocus of the light beam into the other side. There are many types of lenses with different behavior depending on their geometry. Conventional lenses can be analyzed as a Fourier transform system that converts waves from the spatial domain into the angular domain and vice versa. Therefore, a conventional convex lens will transform a plane wave into a spherical wave focused on a point in the so-called lens focal plane, placed at a focal length f [82] (see Fig. 3.6.a). When the plane wave enters the lens with a certain angle (θ) the focused point in the focal plane is displaced from the center of the optical axis (d) inside the focal plane, as it is shown in Fig. 3.6.b. This displacement depends on the focal length of the lens as:

$$d = tan(\theta) \cdot f \approx \theta \cdot f. \tag{3.9}$$

The displacement d in the focal plane depends directly on the input angle θ and the focal length f. Assuming paraxiality ($\theta \approx 0$), it can be approximate as the product between these two parameters. Therefore, a lens is a system that transforms angles into displacements and vice versa. A lens can also function as an image relay, which is an optical system that takes an object and relays its image to another plane at the other side of the lens with a certain magnification. The incoming light rays from the object are refracted by the lens and converge to a point, creating a real inverted image. This image can be viewed directly magnified or reduced at a different distance from the first image plane. The ability of a lens to form an image relay depends on the distances between the object, the lens, and the image plane. When images are further away from the focal length of the lens at a distance u on one side, it relays the image into the image plane situated at a distance v, and the focal length of the lens relates these two distances as:

$$\frac{1}{u} + \frac{1}{v} = \frac{1}{f}, \tag{3.10}$$

the projected image will be inverted and will have a magnification M depending on the distances u and v as:

$$M = -\frac{v}{u}. \tag{3.11}$$

The negative sign indicates the inversion of the image in the image plane. In many optical systems, lenses are used in conjunction with other optical components or more lenses to create a desired image size, position, and orientation. In Fig. 3.6.c it is shown a schematic of a conventional convex lens working as an image system.

3.3.2. Lens systems for far-field characterization

As previously mentioned, a conventional convex lens can be analyzed as a system that projects the Fourier transform of an incident field into his focal plane. This property is very interesting for radiation-pattern characterization of emitters. Very similar to the solution of parabolic reflectors in the RF domain [102], lenses can be used in optics to bring the far-field region near to the antenna, specifically in the focal plane of the lens. Using an IR-camera the far-field radiation pattern of antennas can be captured with high fidelity if the lens captures the entire near field. In this work, for the design of the lens systems to measure the radiation pattern of the antennas, it has been used the software OSLO (Optics Software for Layout and Optimization) [103]. It is a powerful ray optics simulator that allows modeling complex lens systems using commercial elements and obtaining accurate results.

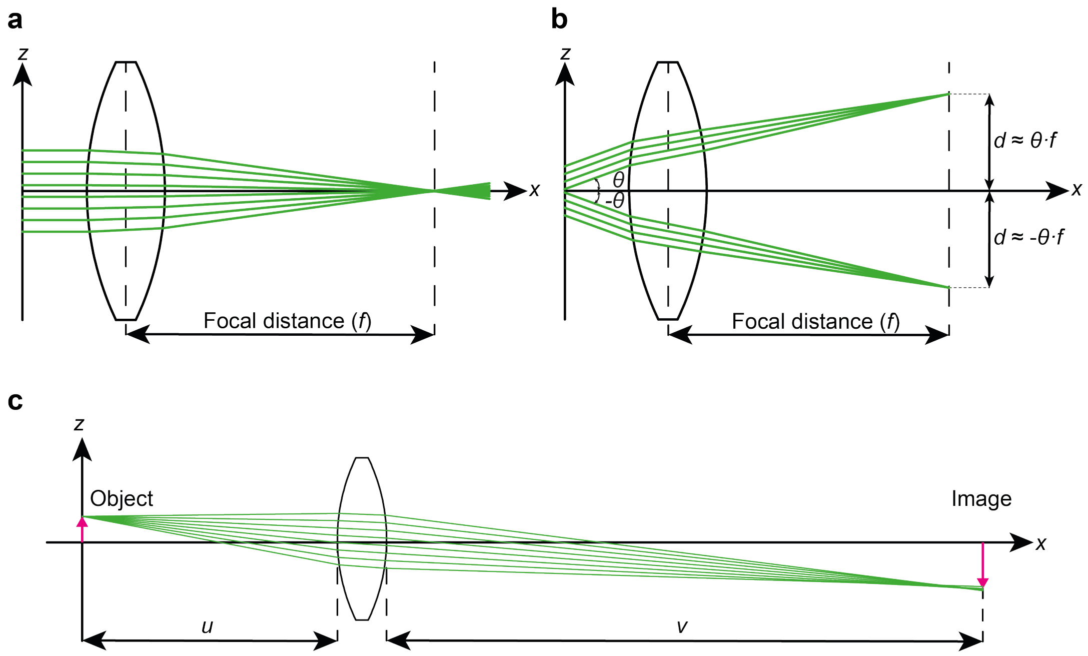

Figure 3.6.: Schematic of lens operation. a) Conventional convex lens focusing a plane wave into a spot at a focal length f. b) The effect of lenses transforming angles into displacements in the focal plane. Two plane waves that enters a lens with different angles θ will be focused at different distances d in the focal plane. c) Lens working as an image system where the object separated a distance u from the lens is relayed into the image plane placed at a distance v with a certain magnification.

Two different lens systems have been designed during this thesis. The first configuration is designed with a single lens that provides an overview of the far-field radiation pattern and allows characterization of the antenna's scanning behavior. This system projects a far-field image onto the IR camera sensor, covering a wide angular range, albeit with a lower image resolution. The second configuration has a more complex design, where two lenses are involved. This lens system is designed to provide a large magnification of the far-field radiation pattern, thus allowing for accurate characterization of the beamwidth of the main lobe. Unlike the previous design, the far-field image projected onto the camera will have a very narrow angular range but an extremely high image resolution. Both systems are designed to project an image of the radiation pattern of the antenna onto a plane, where the sensor of an IR camera should be placed to measure the far-field intensity. For all the measurements in the thesis the same infrared camera has been used, the GOLDEYE P-008 SWIR, which has an InGaAs sensor with 320 × 256 pixels at a pitch of 30 µm. The total size of the sensor is 9.6 mm × 7.68 mm and it is found 1.5 cm inside the housing of the camera. To adapt the system to the IR camera, a tube lens system is used. The tubes must be of sufficient diameter to accommodate the lens of choice, and they are attached to the camera housing through a C-mount. In the following, we will discuss the design of these two different lens systems and the characteristics they offer.

Single-lens setup

The single-lens setup is designed to measure the far-field radiation diagram at various wavelengths to characterize the scanning sensitivity of the antennas. Since the mechanism to steer the radiated beam in the vertical direction (θ) involves wavelength tuning, it is necessary to design an optical lens system without chromatic aberrations. The chromatic aberration arises because the refractive index of a material varies with the wavelength of light, a phenomenon known as dispersion. As per Snell's law, the angle of refraction for light of different wavelengths or colors will vary due to the non-uniform nature of the refractive index. This effect causes a variation of focal length with wavelength in conventional lenses ($f(\lambda)$). Therefore, the single-lens setup consists of an achromatic doublet designed to have its focal plane constantly over the sensor of the IR camera at different wavelengths. An achromatic doublet is a type of lens consisting of two individual lenses with different types of glass and different dispersions. The combination of these lenses helps to minimize chromatic aberration.

The selection of the lens considers many factors as the size and thickness of the lens, separation from the camera housing, length of the tube lens, etc. Even if the design of a lens is obtained by simulation (size, focal length, position,...) then it is necessary to find a commercial lens with similar specifications, which in most cases is not simple. For the single-lens setup there are several commercial lenses that can be used to measure the far field with a wide angular range. However, for this experiment, a particular achromatic doublet was selected based on the availability of lens tubes with exact lengths that could achieve the focal plane over the sensor plane of the IR camera. The chosen lens is the achromatic doublet AC254-035-C from Thorlabs, with a diameter of $D = 1"$ compatible with commercial lens tubes and a focal length of $f = 35.1\,\text{mm}$ and a back focal length of $f_b = 27.4\,\text{mm}$. Fig. 3.7.a shows a schematic of the complete system, including the achromatic doublet AC254-035-C, the lens tube SM1L03, and the SM1 to C-mount adapter SM1A9 from Thorlabs. The total length of the lens tube system is 29.1 mm. With the focal length ($f = 35.1\,\text{mm}$) and the size of the IR camera sensor ($9.6\,\text{mm} \times 7.68\,\text{mm}$) the FoV available for the far field can be estimated using Eq.3.9:

$$\text{FoV}_\theta = \frac{180^\circ}{\pi} \cdot \frac{9.6}{35.1}$$

$$\text{FoV}_\phi = \frac{180^\circ}{\pi} \cdot \frac{7.68}{35.1}$$

The achromatic doublet can project into the sensor the radiation pattern with an angular range of $15.7^\circ \times 12.5^\circ$ and a minimum resolution of $\Delta\theta \approx \Delta\phi = 0.05^\circ/\text{pixel}$. This FoV will be the maximum angles that could be measure from the far-field radiation pattern, which are sufficient to demonstrate the antenna scanning in the wavelength band of operation ($\lambda = [1500\,nm - 1640\,nm]$). In Fig. 3.7.b it is shown a simulation in OSLO of the lens, and in Fig. 3.7.c its behavior with wavelength, presenting a maximum focal shift from the central wavelength of $50\,\mu\text{m}$ in the entire wavelength band, which is negligible for this measurement. In the following table (Table 3.1) an overview of the specifications that offers the single-lens system is collected.

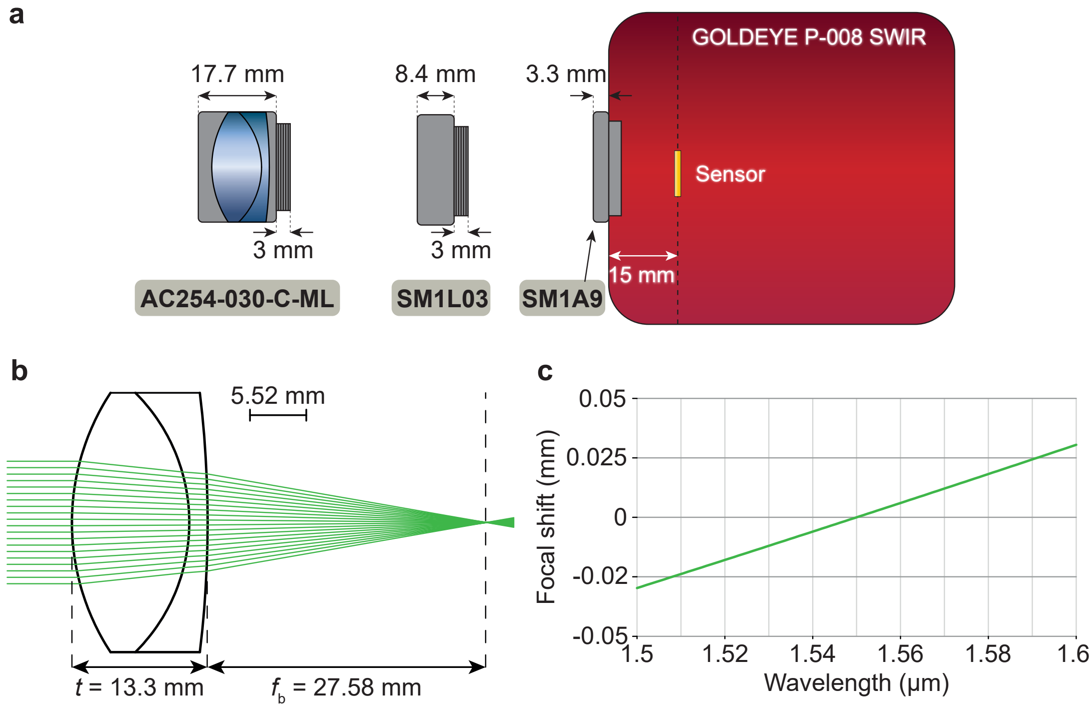

Figure 3.7.: Schematic of the single-lens system. a) Schematic of the achromatic doublet together with its case and the necessary tube lenses to measure the far-field patter in the IR camera sensor. b) Ray tracing simulation in OSLO of the commercial achromatic doublet. c) Behavior of the system with a wavelength tuning, presenting a negligible effect in the focal distance of the system.

Length (mm)	Field of View (°)	Resolution (°)	Focal shift (μm)	D (mm)
29.1	15.7 × 12.5	0.05	50	1" = 25.4

Table 3.1.: Main specifications of the single-lens setup. The focal shift is obtained from a wavelength sweep of 100 nm from 1.5 μm to 1.6 μm.

Double-lens setup (magnification system)

The magnification system consists of two lenses: a plano-convex lens that will perform the Fourier transform of the near field radiated by the antenna, and a bi-convex lens that will be responsible for relay the image of the far field from the focal plane of the first lens to the sensor plane of the IR camera with a certain magnification (M). Fig. 3.8.a shows a simulation in OSLO of how these two lenses work to achieve the far-field image magnified in the plane of the camera sensor. As can be seen in Fig. 3.8.a, the final displacement (z_2) will depend on the focal length of the first lens (f_1), the input angle (θ) and the magnification (M). The use of a large magnification in the measurement system will enable the characterization of highly collimated beams with increased resolution compared to the previous setup. However, this comes at the expense of a reduced angular range available in the far-field image. The system is designed to target a resolution of $\Delta\theta = 0.01°/\text{pixel}$, which is sufficient to characterize the beamwidth of the emitted beams of the antennas studied in this thesis. To achieve this, the following condition needs to be fulfilled:

$$\Delta z = f_1 \Delta\theta M \Rightarrow f_1 M = 171.88\,\text{mm/rad}, \tag{3.12}$$

where Δz is the physical size of a pixel of the camera ($\Delta z = 30\,\mu\text{m}$), $\Delta\theta$ is the target resolution we want to achieve, f_1 is the focal length of the first lens in the system and M is the magnification of the second lens. If the first lens is chosen with a large focal distance, the second lens will be less restrictive as the magnification M will be lower. After performing simulations in OSLO and reviewing the catalog of available commercial lenses and lens tubes at Thorlabs, the final system is composed of the following components: The plano-convex lens LA1509-C with a focal length of $f_1 = 100\,\text{mm}$ and a diameter of $D = 1"$ packaged in a lens tube SM1L40. This will be the first lens of the system placed near the antenna, and it will project the far-field radiation diagram in its focal plane at a distance f_1. The second lens is the bi-convex lens LB1761-C with a focal length of $f_2 = 25.4\,\text{mm}$ and a diameter of $D = 1"$ packaged in a lens tube SM1L25. The distance between the lenses is adjusted to be 140.5 mm between last and first surfaces of the lenses. Therefore, the distance between the far-field image and the second lens will be $u = 40.2\,\text{mm}$ and the distance between the second lens and the magnified image on the camera sensor will be $v = 69\,\text{mm}$. A schematic of the complete system together with the necessary tube lens is shown in Fig. 3.8.b. The designed distances for u and v theoretically result in an image system with a magnification of $M = 1.72$. However, the validity of Eq.3.11 is limited to ideal lenses (planar devices), and since the lenses in this case have thickness, the performance of the system degrades. To measure the magnification of the second lens, a Gaussian beam was propagated through the system using OSLO, as shown in Fig. 3.8.c. The input Gaussian beam has a radius of $W_{in} = 1\,\text{mm}$, and after being focused in the focal plane of the first lens, it has a radius of $W_u = 50.7\,\mu\text{m}$. After passing through the second lens, it is focused into a beam of $W_v = 76.4\,\mu\text{m}$. Therefore, the effective magnification of the second lens is $M = W_v/W_u = 1.42$. The system's resolution in the simulation is $\Delta\theta_{\text{simulation}} = 0.012°/\text{pixel}$, which is very similar to the theoretical value of $\Delta\theta_{\text{theory}} = 0.01°/\text{pixel}$. Finally, as the lenses used in the system are made with the same material NBK-7, they suffer from chromatic aberration, and the system is not tolerant to wavelength tuning. In Fig. 3.8.d the behavior of the system when the wavelength changes is represented, having a maximum focal shift from the central wavelength of 1.25 mm, which is going to blurry the projected image in the camera sensor. However, this is not a limiting factor since the section between the second lens and the IR camera is made of an adjustable lens tube SM1V15 and a conventional lens tube SM1L15 to have the possibility of focusing the image on the sensor when the wavelength of the emitted beam is changed. The double-lens system presents a resolution of $\Delta\theta = 0.01°/\text{pixel}$, which is ~ 5× more than the previous lens system. However, as the sensor has 320 × 254 pixels, the available FoV for the far-field image is reduced to 3.2° × 2.54°. In the following table (Table 3.2) an overview of the specifications that offers the single-lens system is collected.

Length (mm)	Field of View (°)	Resolution (°)	Focal shift (mm)	D (mm)
221.3 − 259.4	3.2 × 2.54	0.01	0.8	1" = 25.4

Table 3.2.: Main specifications of the double-lens setup. The length of the system is inside a range as there is an adjustable lens tube. The focal shift is obtained from a wavelength sweep of 100 nm from 1.5 µm to 1.6 µm.

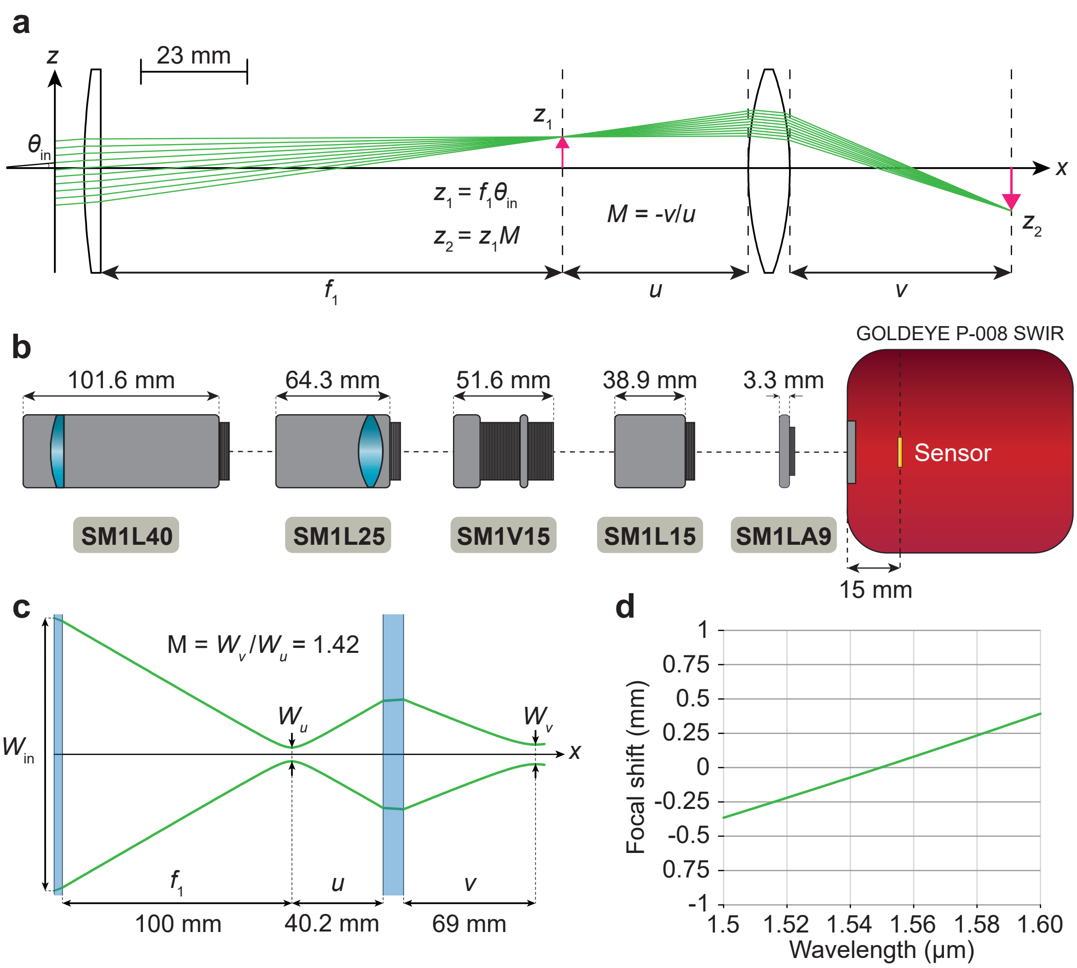

Figure 3.8.: Schematic of the double-lens system. a) Ray tracing simulation in OSLO of a double lens system, where the first lens works as a Fourier transform system and the second lens acts as an image relay with a specific magnification factor M. b) Schematic of the double-lens system, including the necessary commercial tube lenses, used for measuring the far-field pattern of integrated optical antennas with an IR camera. c) Simulation in OSLO demonstrating the propagation of a Gaussian beam through the system. The observed magnification closely aligns with the theoretical estimation, although slight deviations are present due to the non-ideal characteristics of the lenses. d) Behavior of the system with wavelength tuning, showcasing pronounced variations in focal length arising from the chromatic aberration present in both lenses.

3.4. Mask layout and fabrication of the prototypes

This section describes the last step in the prototyping cycle before the experimental characterization of the integrated optical antennas. So far, all the necessary tools for designing integrated optical antennas have been explained. Software methods such as Floquet-Bloch analysis and far-field calculation have been used to reach the final designs. Additionally, different lens systems have been developed in this Thesis to characterize the radiation pattern of the antennas in the laboratory. However, in order to measure the performance of the designed devices, fabrication of the prototypes is required. This entails the need for a well-controlled environment, such as a clean room, with highly specialized fabrication processes to precisely pattern the materials used for the devices through CMOS-compatible protocols.

This Thesis was conducted at the Photonics & RF Lab at the University of Malaga, a research group equipped with the necessary tools and expertise to undertake nearly all stages of prototyping, encompassing design, modeling, and experimental characterization of integrated optical devices. However, as a fabless research group, the chip manufacturing process is outsourced to external facilities. All the devices fabricated during this Thesis were made in the commercial foundry Applied Nanotools Inc (ANT) [104]. This Canadian company provides fabrication services for solid-state chips on various platforms, such as silicon-on-insulator (SOI) and silicon nitride (Si_3N_4). All the integrated optical antennas designed in this Thesis have been developed for the SOI platform. ANT offers a fabrication service for multi-project wafers (MPW) of SOI chips, with a fabrication run scheduled every two months. The chips fabricated in these MPW runs have a dimension of 9 mm × 9 mm, and they are patterned in a 220-nm thick silicon layer with a 2-μm buried oxide (BOX) layer using electron beam lithography and anisotropic ICP-RIE etching process, with a single fully etch step. The minimum feature size they offer is 60 nm, which allows the synthesis of deep-SWG metamaterials. The cladding is optional and they are able to fabricate a 2.2-μm thick upper SiO_2 cladding deposited by chemical vapor deposition. Finally, depending on the devices used to couple light into the chip, chip facets can be defined with a deep-etch process.

To carry out the fabrication at ANT, they require what is known as a fabrication mask. The mask is a file that geometrically indicates the location of the devices on the chip. In the case of ANT, it is necessary to specify the portion of silicon that does not need to be fully etched. The delivery time for the fabricated chips using MPW runs is approximately 2-3 months. Given the considerable time it takes to characterize the designs experimentally, the process of creating the fabrication mask becomes crucial. In order to maximize efficiency in the group, researchers often share a single mask, allowing them to incorporate as many designs as possible on a single chip.

The fabrication mask not only includes the main designs to be tested but also incorporates additional structures known as auxiliary devices. The inclusion of these auxiliary devices is a crucial aspect of the mask design process, as they are responsible for guiding the light to test the correct functioning of the device under test (DUT). The antennas presented in the three publications of this Thesis were fabricated on the same chip along with many auxiliary structures to characterize their performance. The chip mask includes weak metamaterial surface-emitting antennas designed for TE (in-plane) and TM (out-plane) polarization, as well as antenna designs to maximize the scanning sensitivity by using slow-light metamaterial waveguides and arrays of antennas fed with distributed Bragg reflectors. A schematic representation of the mask is depicted in Fig. 3.9, highlighting specific devices with corresponding scanning electron microscope (SEM) images. These SEM images are captured prior to cladding deposition at the foundry and serve as a valuable tool for quantifying fabrication errors. Understanding these errors is crucial in comprehending the behavior of the DUT as measured in the laboratory.

3.4.1. Main aspects for a mask design

Coupling light into the chip

The experimental equipment for characterizing the prototypes used in this Thesis requires the use of an external laser. In this case, a fundamental device must be included in the mask,

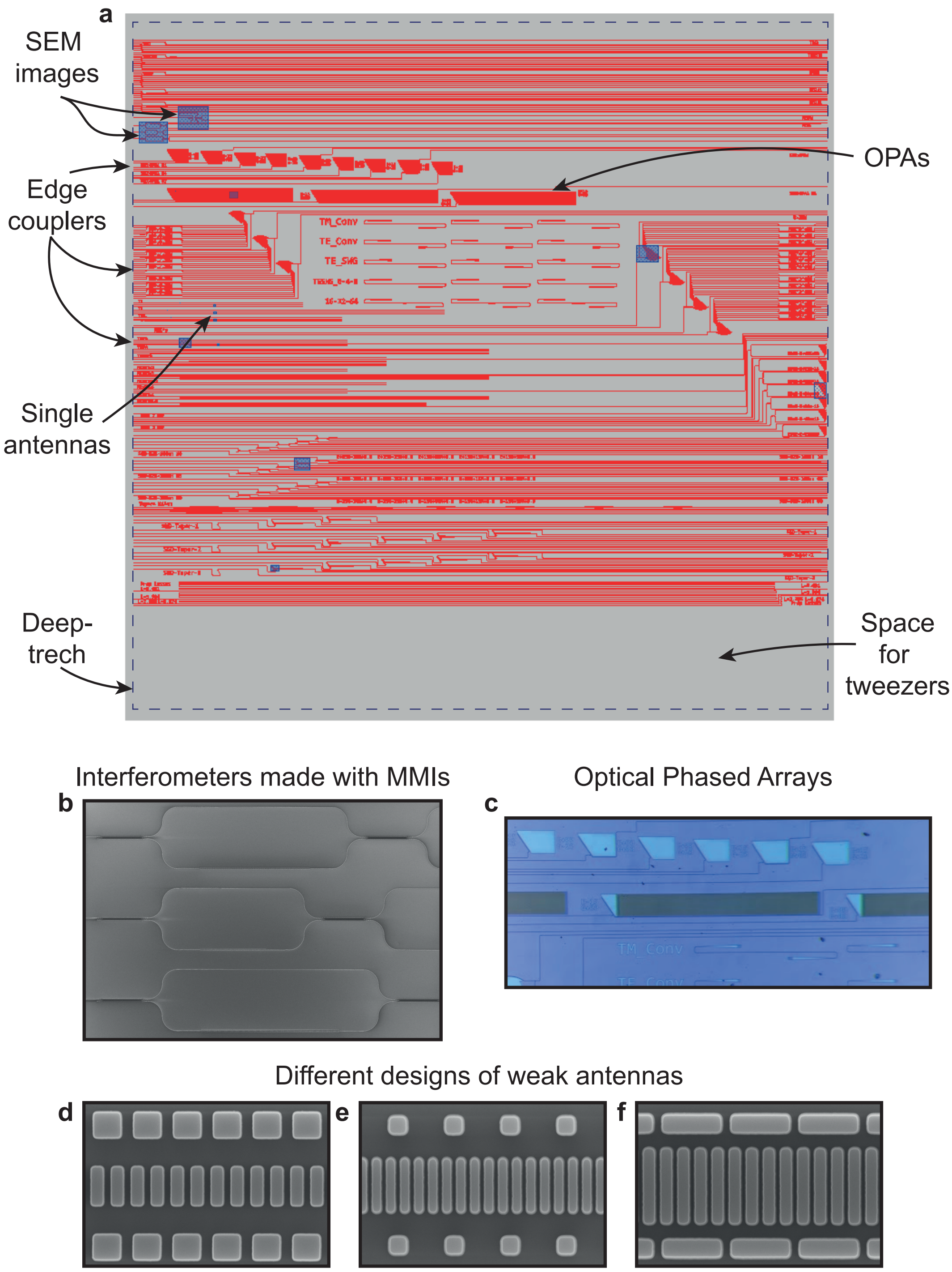

Figure 3.9.: Fabrication mask for ANT MPW run for SOI platform. a) Mask layout for the fabrication of metamaterial surface-emitting antennas, with grey and red colors indicating the etched and non-etched areas, respectively. The dashed line represents the boundary for deep-trench, necessary when light is coupled to the chip through the edge. Blue areas indicates the region for SEM imaging. b) SEM image of a Mach-Zehnder interferometer using 2×2 MMIs. c) Microscope image of an optical phased array (OPA). d), e), f) Different prototypes for weak metamaterial surface-emitting antennas.

fiber-chip couplers. The fundamental mode of a single-mode fiber at an operating wavelength of 1550 nm has a mode field diameter (MFD) approximately $\sim 20\times$ larger than the MFD of a conventional strip waveguide in SOI. In recent years, significant research efforts have been focused on developing highly efficient couplers with large bandwidths. However, these solutions often require special fabrication processes that are not compatible with commercial foundries [105–107]. In the context of silicon-on-insulator (SOI) platforms, two common methods are used to couple light into the chip: surface grating couplers and edge couplers.

Surface grating couplers offer the advantage of being able to be placed anywhere on the chip. However, they typically suffer from poor coupling efficiency, limited operation bandwidth and a strong polarization dependence. Additionally, grating couplers require a specific setup that involves tilting an optical fiber to enable coupling of light at the designed angle of the grating coupler. It is crucial to position the fiber as close as possible to the grating to minimize free-space beam divergence. In most cases, a conventional fiber with a straight-cut facet is used for this purpose. An schematic of a grating coupler with typical size values is shown in Fig. 3.10.a.

Edge couplers, on the other hand, offer a solution with a wider operating bandwidth. These couplers are positioned near the edge of a chip and work by delocalizing the mode through an adiabatic waveguide to achieve better matching with the mode profile of a fiber. Edge couplers can only be used at the chip facets, and for coupling light into them, a lensed fiber with a MFD of $2-3\,\mu$m is typically employed at a specific working distance from the edge ($\sim 15\,\mu$m). The lensed fiber helps to collimate the mode of a single-mode fiber into a small spot, thereby relaxing the requirements for mode delocalization in the edge coupler. Furthermore, edge couplers offer a large operation bandwidth and they can be designed to work for both polarizations TE (in-plane) and TM (out-plane). A schematic of a grating coupler with typical size values is shown in Fig. 3.10.b.

For the fabrication mask developed in this Thesis, edge couplers were employed to couple light into the chip. This choice was made considering that the antennas are dispersive devices with a wide wavelength band of operation (the same band as the laser source). Using edge couplers is more suitable in this scenario compared to grating couplers, as it allows for measuring the scanning behavior of the antennas through wavelength tuning. The edge coupler implemented in the mask is an SWG metamaterial edge coupler [108], which offers low losses and similar behavior for both polarizations in SOI.

Flavors for fabrication compensation

During the fabrication process of the designed devices, there is always an inherent uncertainty associated with possible fabrication errors. The most common errors encountered in commercial foundries are under-etching and over-etching of the silicon segments, as well as small variations in the thickness of the silicon layer. These errors have the potential to alter the refractive index of the supported modes in these devices, resulting in behaviors that may differ from the originally simulated ones.

To compensate this type of errors, the mask includes variations of the nominal design known as flavors. The flavors are copies of the nominal design whose size has been scaled by a factor δ. For the fabrication of the prototypes each nominal design has flavors with

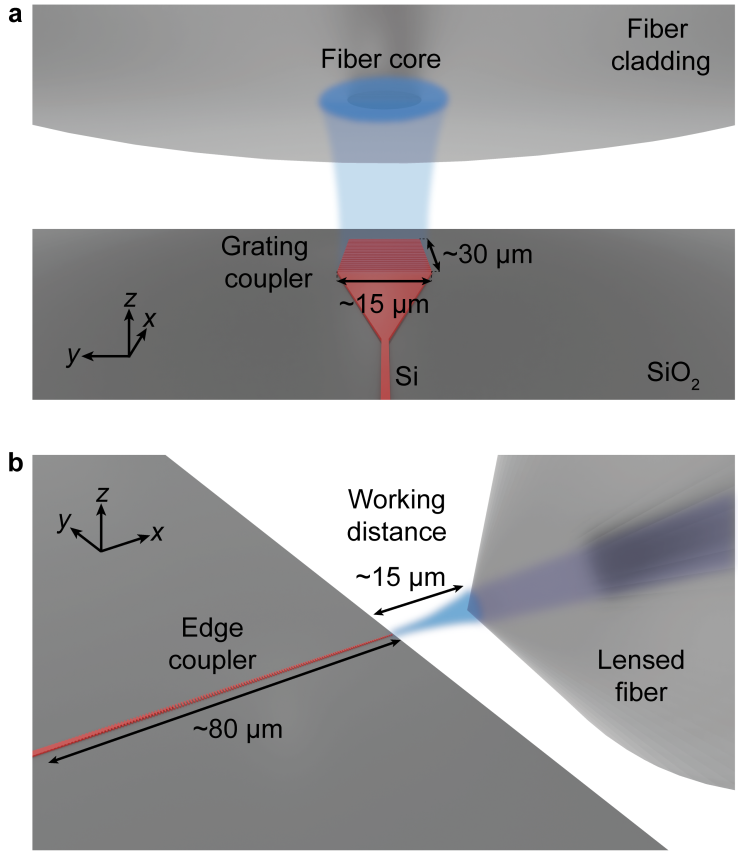

Figure 3.10.: Two commonly used approaches for light coupling into SiPh chips a) Conceptual depiction illustrating a fiber positioned over a grating coupler, enabling the coupling of the fiber mode into the periodic structure. b) Conceptual depiction showing an edge coupler receiving light from a lensed fiber, where the focused spot size closely matches the delocalized mode achieved by the edge coupler at its tip.

$\delta = \pm 20\,\mathrm{nm}$.

Auxiliary devices

The auxiliary devices consist of essential structures integrated on the chip to facilitate the routing of light into the DUT. These devices typically comprise interconnection waveguides, tapers, and MMIs (Multimode Interference devices) that serve as power splitters.

An interconnection waveguide in a SiPh chip refers to a guiding structure designed to facilitate the efficient transmission of optical signals between different components or functional elements within the chip. In the fabricated chip for antenna prototyping, optical interconnects with a width of 500 nm were used. This dimension is typical for these waveguides, as it ensures that only the fundamental mode for both polarizations (TE and TM) can propagate effectively, without any leakage to the bottom substrate when a 2 μm thick buried oxide (BOX) layer is used.

In theory, a conventional waveguide should not introduce losses to the propagating mode if there is no leakage. However, during the fabrication process, there are inherent physical phenomena, such as side-wall roughness, that can induce losses. Side-wall roughness losses occur when there is a random modulation in the lateral wall of the waveguide during the etching process, resulting in some level of attenuation. To measure this effect, the cut-back technique can be used. This technique requires injecting power into one side of the chip, passing through the structure to be analyzed, and having enough power coming out of the chip. By calculating the output power for the same device with different lengths, the losses introduced by the device can be easily obtained through linear regression of the output power as a function of the device length. By using this method, we estimated the losses introduced by the interconnection waveguides for both polarizations TE and TM at different wavelengths (see Fig. 3.11.a and Fig. 3.11.b). The total losses in units of dB/cm introduced by the waveguides are represented in Fig. 3.11.c. At an operating wavelength of $\lambda = 1550\,\mathrm{nm}$ a mode propagating through the interconnection waveguide exhibited a loss of $L_{TE} = 0.95\,\mathrm{dB/cm}$ for TE polarization and $L_{TM} = 1.1\,\mathrm{dB/cm}$ for the TM polarization, which were lower than the typical values offered by ANT. Finally, if the linear regression is extended to a length of zero, the measured loss is the one related with the coupler. In this case, we used for all the devices a metamaterial edge coupler as mentioned before, whose measured losses are showed in Fig. 3.11.d

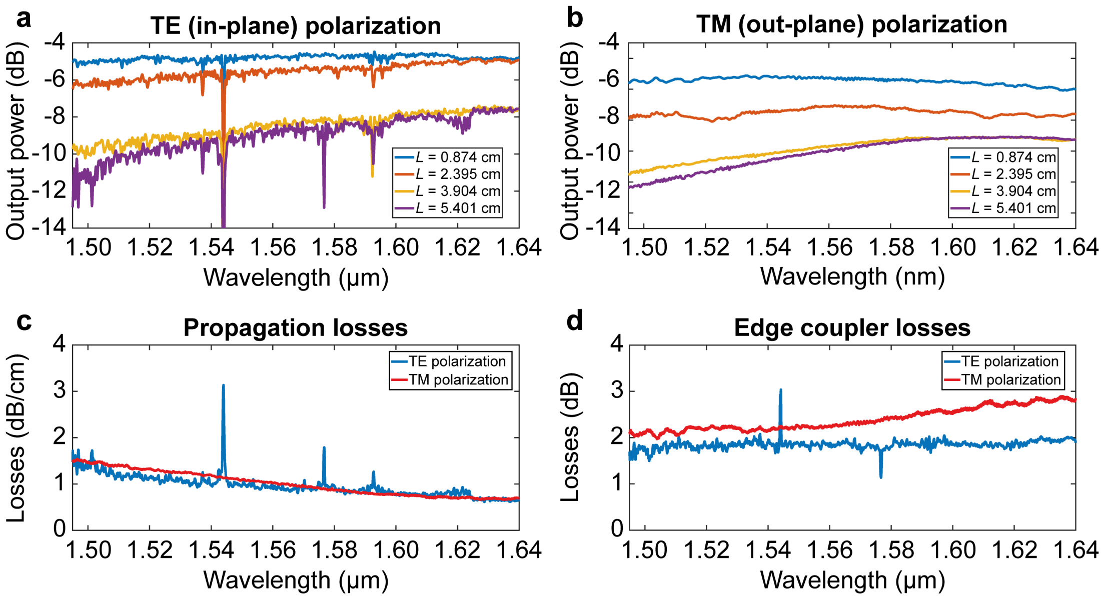

Figure 3.11.: Cut-back method to estimate interconnection waveguide losses. Measured losses of an interconnection waveguide for different lengths and wavelengths for a) TE polarization and b) TM polarization. The measurement of the third waveguide (yellow curve) is not valid. This power drop may be due to facet damage.) Total losses in units of dB/cm. d) Losses inherent to the edge coupler when the linear regression is extended to zero length.

Another widely used auxiliary device is the taper waveguide. A waveguide taper is a type of waveguide with a gradual change in the width along its length. It is employed to efficiently couple light between waveguides with different dimensions or geometry, such as interconnecting a conventional waveguide and an SWG waveguide. In the case of interconnecting a conventional waveguide with an SWG waveguide, the taper linearly decrease its width, while the periods of the SWG material are placed over the taper. This process allows for efficient mode conversion and avoids excessive mode mismatch, which could lead to significant power loss and degraded device performance. For the case of the fabricated chip, the taper was designed to couple the light between the interconnection waveguide an the SWG waveguides of the antenna cores with a length of $L = 15\,\mu\text{m}$, ensuring minimal power loss and maintaining the desired mode characteristics like polarization.

3.4.2. Design of experiments for antenna characterization

The devices developed in this Thesis were fabricated on the same chip along with many auxiliary structures to characterize the performance of the antennas. The chip mask included designs for antennas with TM and TE polarizations, as well as designs to maximize scanning sensitivity by using slow-light metamaterial waveguides and arrays of antennas fed with distributed Bragg deflectors. For the characterization of each antenna, three experiments were designed: calculation of the radiation strength, calculation of the group index of the Floquet-Bloch mode, and characterization of the far-field radiation pattern. In total, all the following devices were included in the chip:

- 27 test structures to measure the radiation strength of the antennas.
- 4 MZIs to measure the group index of Floquet-Bloch modes traveling through the antennas and interconnecting waveguides.
- 9 weakly radiating antennas and 9 antenna arrays with 2, 4 and 8 antennas.
- 3 1D-OPAs with 112 antennas grouped in the transverse direction, and fed with a distributed Bragg deflector.

The experiment for characterizing the far-field radiation pattern has been previously discussed when the lens systems were presented, as it is the only experiment that requires measurements to be conducted off-chip. However, there are other important parameters that can be estimated on-chip, such as the radiation strength of the antennas and the group index of the Floquet-Bloch modes (related to scanning sensitivity). The following is an explanation of the methodology used to determine these parameters directly on the chip.

Radiation strength experiment

To quantify the radiation strength of the different antenna designs, the cut-back method was employed to determine the losses associated with these structures. In the case of antennas, there are two primary sources of losses: losses inherent to propagation through an SWG waveguide and losses resulting from the radiation of light off-chip.

The mask included for each antenna design: i) an experiment with the SWG core of the antenna with three different lengths. ii) an experiment with the antenna with three different lengths, the same as the ones used for the SWG core characterization. This allowed for performing a cut-back analysis to estimate the losses associated with the SWG, followed by another cut-back analysis to estimate the radiation strength of the antennas after accounting for the SWG losses. This resulted in a total of 27 input-output pairs on the chip, considering three lengths for each design and three different flavors for design.

Conclusive measurements could not be obtained because the selected lengths for the cut-back method were too short. As both loss sources exhibited a very weak effect, the power transmission measurements lacked sufficient resolution to distinguish a significant power difference between the measurements. However, the radiation strength of each antenna could be estimated thanks to the far-field characterization experiment, as will be shown in the next chapter.

Group index experiment

Measuring the group index of the Floquet-Bloch modes propagating through the antennas is of great interest. The group index directly affects the scanning sensitivity of the antennas, as explained in Chapter 2 (Eq. 2.29). While the far-field characterization experiment can provide this information about the scanning sensitivity, comparing the on-chip results with the far-field measurements serves as a valuable cross-validation, ensuring the proper functionality of both systems.

To measure the group index of the Floquet-Bloch modes interferometric techniques were used. The design of Mach-Zehnder interferometers (MZI) was realized to obtain these values. A first MZI is designed to measure the group index of the modes propagating through the interconnection waveguides. With this information, a second MZI is designed to measure the group index of the Floquet-Bloch modes of the antennas. Each MZI is designed with a different approximation.

The first interferometer to be designed aims to obtain the group index of the mode of

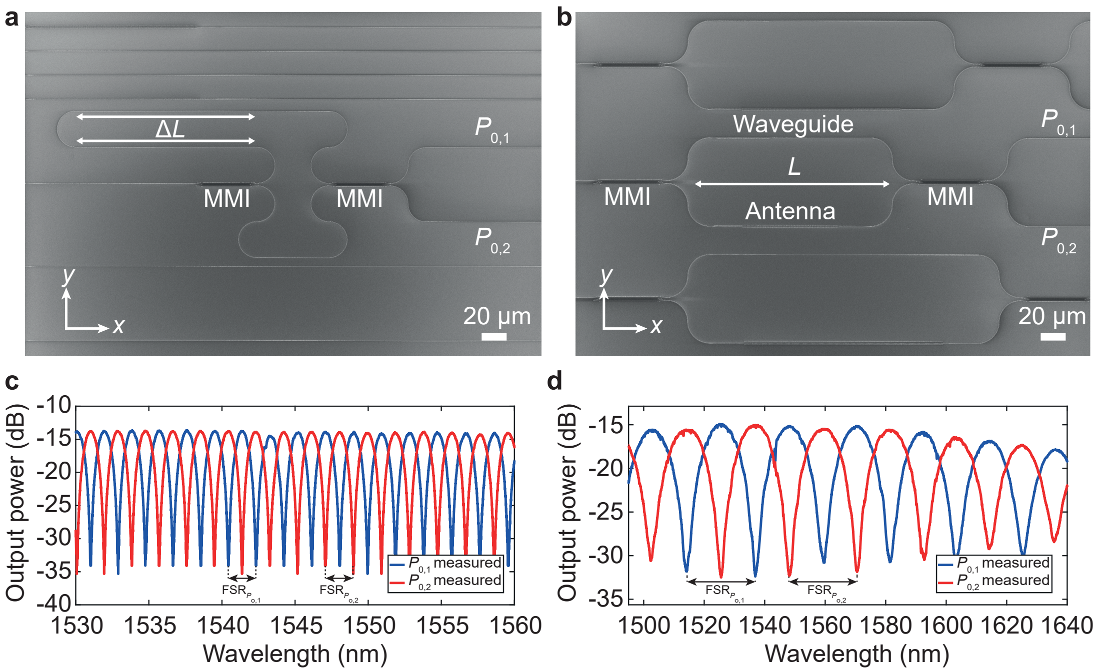

Figure 3.12.: Mach-Zehnder interferometers for group index characterization: a) MZI design for measuring the group index of the interconnection waveguides. b) MZI designs for measuring the group index of the Floquet-Bloch mode propagating in the antennas. c) Transmitted power function of the MZI for the interconnection waveguide on each output. d) Transmitted power function of the MZI for the antennas on each output.

the interconnection waveguides. For this purpose, a 2×2 multimode interferometer (MMI) will be used to split the power into two paths of different lengths (L_1 and $L_2 = L_1 + \Delta L$). Each arm of the MZI will consist of a photonic wire with the same dimensions as the interconnection waveguides. These two paths will be recombined at the output using a 2×2 MMI (see Fig. 3.12.a). By scanning the wavelength at the interferometer output, it will be measured the free spectral range (FSR), which is the distance in wavelengths between two consecutive maxima of the transmitted power, as shown in Fig. 3.12.c. With this information and knowing the path length difference between the two arms (ΔL), we will be able to obtain the group index of the photonic wire, defined as:

$$n_{g,\mathrm{PW}} = \frac{\lambda^2}{\Delta L \cdot \mathrm{FSR}}. \tag{3.13}$$

Once the group index of the interconnection waveguide is determined, a new MZI can be designed to estimate the group index of the Floquet-Bloch mode of the antennas. In this new MZI configuration, both arms have the same length (L), with one arm consisting of a photonic interconnection waveguide and the other arm comprises an antenna with a short length to minimize radiation losses. By measuring the FSR at the output of the MZI (see Fig. 3.12.b), the group index of the Floquet-Bloch mode can be obtained as follows:

$$n_{g,\mathrm{antenna}} = \left| n_{g,\mathrm{PW}} - \frac{\lambda^2}{L \cdot \mathrm{FSR}} \right|. \tag{3.14}$$

In Fig. 3.12.d, it can be observed that the FSR curves exhibit a gradual decay with increasing wavelength. This behavior is attributed to the frequency-dependent radiation strength of the antenna.

3.4.3. Laboratory equipment

All the antenna designs presented in this thesis have undergone fabrication and experimental characterization at the Photonics & RF Laboratory of the University of Malaga. The experimental setup used for this purpose is divided into three different stages summarized with photographs in Fig. 3.13.

Input stage

The input stage is in charge of routing the light from an external laser source to the chip. The external source is the Agilent 81600B tunable laser that injects the light into a SMF-28 fiber. Then a polarization controller (FPC561 from Thorlabs) is used to align the linear polarized light of the laser with a polarization filter. The linearly polarized light at the output of the filter is then guided to another polarization controller (FPC561 from Thorlabs) which aligns the polarization of the fiber with the desired on-chip polarization. Finally, before reaching the chip, the fiber is connected to an optical circulator whose outputs are a fiber injecting the light into the chip and a photodiode to measure the reflections coming from the chip.

Chip stage

The chip stage is responsible for coupling light into and out of the chip. For this work, edge couplers have been used. A lensed fiber is connected to the output of the circulator guiding the light to the edge coupler at the input chip facet. At the output chip facet another edge coupler will guide the light to the free space and a microscope objective placed near will collect the light.

Output stage

The output stage is divided into two different paths. The first path is used for the characterization of on-chip devices using the cut-back method and for the alignment of the input lensed fiber and the output microscope objective with the corresponding edge couplers. All the light collected by the microscope objective is collimated and guided to a Glan-Thompson polarizer and then onto a photodetector (818-IR). A folding mirror can be used to focus the light into a camera to help in the alignment. The second path involves the use of the lens systems, as explained in Section 3.3.2, which consists of a separate system placed over the chip for the characterization of antenna radiation patterns.

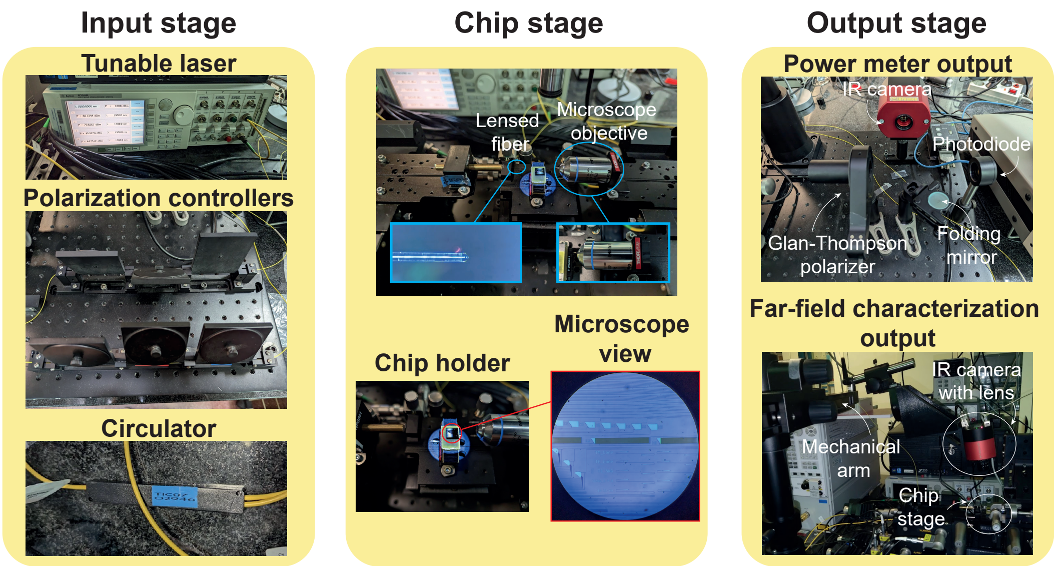

Figure 3.13.: Different stages of laboratory setup to characterize photonic chips. The input stage shows photographs of the main elements such as the laser source, the polarization controllers and the circulator that is placed in the last section before injecting light into the chip. The chip stage shows the lensed fiber that injects light on one side of the chip and the microscope objective that collects the light on the other side of the chip. Finally, two different setups are shown in the output stage, the one corresponding to the device alignment and the one designed to characterize the antenna radiation pattern.

4. Final designs and publications

This chapter provides a comprehensive overview of the diverse designs of metamaterial surface-emitting antennas developed during the Thesis, showcasing the main research of this work through a compilation of validated publications. The first and second publication introduce a novel topology for the development of weak radiating antennas on the SOI platform, targeting an operating wavelength band within 1500–1640 nm, which is the available wavelength band of the laser source used to characterize the prototypes (Section 3.4.3). This topology involves employing an SWG core in conjunction with evanescently coupled lateral segments that are arranged in a periodic manner along the propagation direction, enabling the efficient radiation of the mode off-chip (see Fig.4.1). The separation of the lateral segments with the SWG core (g) gives a highly precise mechanism to control the radiation strength of the antennas. With this innovative approach, millimeter-scale antennas can be designed without being constrained by fabrication limitations, as the MFS of the device can be significantly large. The latest publication in this Thesis centers around the design and characterization of a complete 1D-OPA. It leverages the use of these metamaterial surface-emitting antennas to form an array with a large directivity and the ability to electronically steer the radiated beam, eliminating the need for mechanical adjustments. Moreover, the publication introduces an innovative feeding scheme employing a distributed Bragg deflector working as a beam expander, providing a compact and efficient solution that deviates from conventional approaches. These advancements position these antennas as pivotal components in several beam-steering applications such as Free-Space Optics (FSO) and remote sensing.

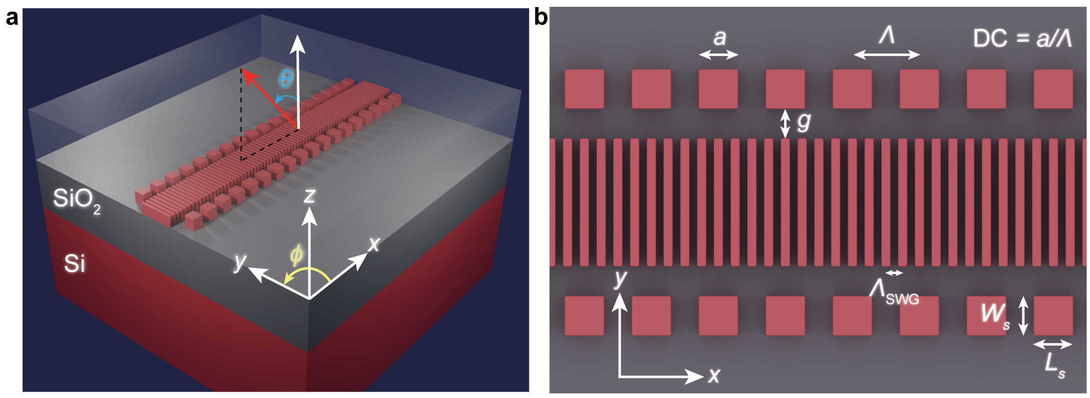

Figure 4.1.: Main topology presented in this Thesis. The topology of a metamaterial surface-emitting antenna. a) 3D-view shcematic. b) Top view schematic

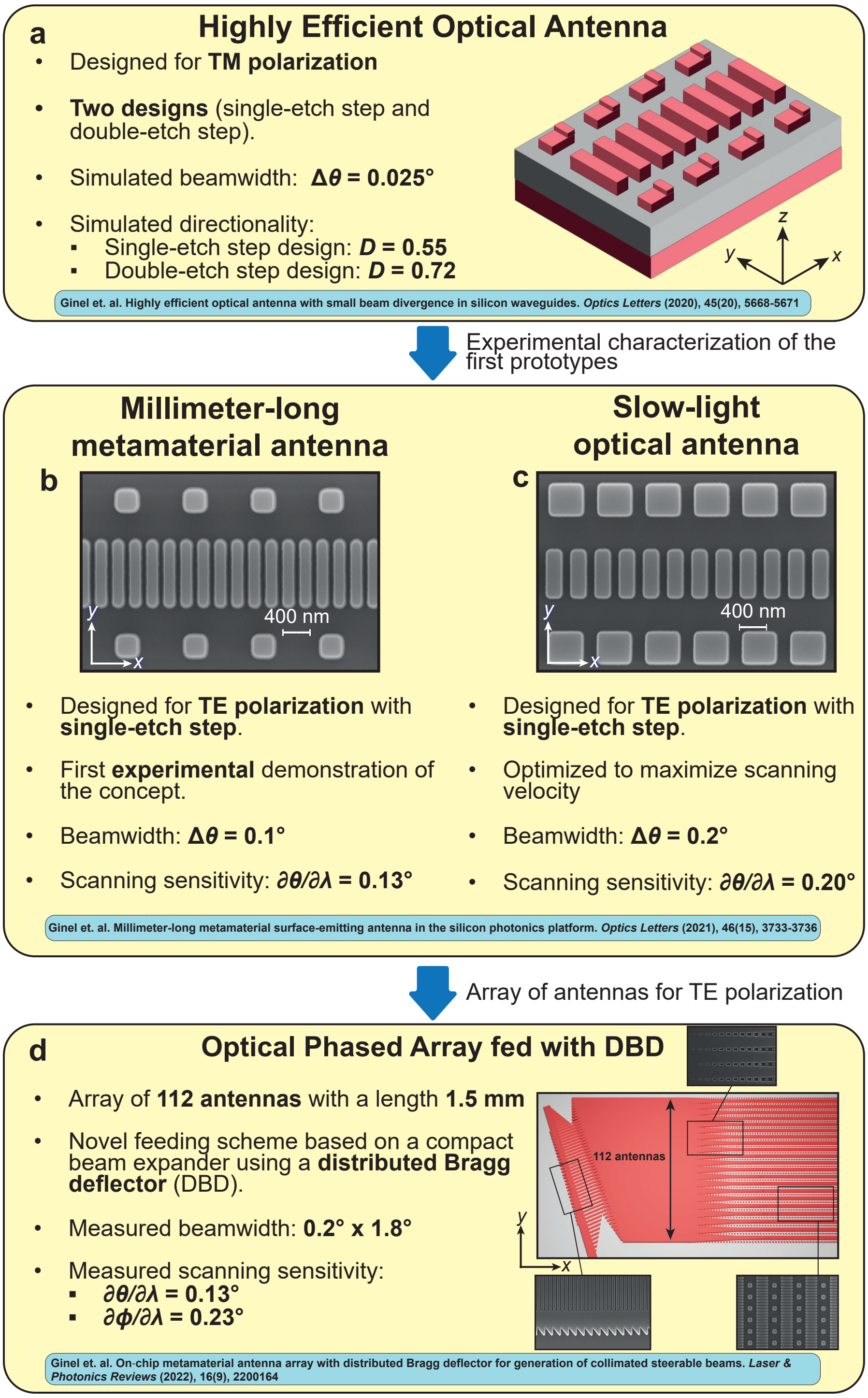

Figure 4.2.: Overview of the different designs of antennas developed during the Thesis. The chronological evolution of metamaterial surface-emitting antenna designs developed during the Thesis is presented in this figure. a) Highly efficient optical antenna. b) Millimeter-long metamaterial antenna. c) Slow-light optical antenna. d) Optical phased array fed by distributed Bragg deflector.

4.1. Overview of metamaterial surface-emitting antenna designs

Figure 4.2 represents an overview of all the antenna designs developed during the Thesis and the progressive research carried out during this work. The research progress has been characterized by a series of milestones presented below.

4.1.1. Simulation and verification of the topology for SOI platform.

The first milestone of the research was focused on the modeling and design of antennas using the proposed topology (Fig. 4.2) particularized for the SOI platform. Several software tools were developed to efficiently design weak radiating antennas (Chapter 3, Section 3.2.1-3.2.2). As a result, a large variety of antennas were designed (see Fig. 4.2.a-c), demonstrating the versatility offered by the proposed topology. The main objective in the design process was focused on achieving weak antennas with an aperture size in the millimeter-scale ($\alpha < 2\text{mm}^{-2}$). This design approach enables the antennas to exhibit remarkably narrow far-field beam divergences of approximately $\sim 0.1°$. Another crucial design objective was related to the radiation angle, which was carefully engineered to be sufficiently far from the normal of the chip plane ($\theta = 0°$). This deliberate choice helps prevent issues related to coupling light into the periodic structure within the second Bragg region. Furthermore, the effective index of the Floquet-Bloch mode is meticulously designed to avoid leakage to the bottom substrate and ensure sufficient delocalization. This consideration helps mitigate losses resulting from side-wall corrugation and fabrication errors, particularly in the case of SWG waveguides.

Figure 4.2.a exhibits the initial results obtained in the Thesis, focusing on the design of a metamaterial surface-emitting antenna for TM polarization. As the simulation methods became more refined and precise, the potential of the topology was explored further, leading to the research of innovative techniques such as double-etch step designs to enhance radiation efficiency. The publication titled "Highly efficient optical antenna with small beam divergence in silicon waveguides" presents the entire design process along with simulated results for both the single etch-step antenna and its highly efficient counterpart achieved through the double-etch step process [109]. This publication marks the first appearance of the proposed topology for weakly radiating antennas, showcasing an unprecedented antenna length of 3.65 mm for silicon-based surface-emitting antennas in simulation. The corresponding design yields a remarkable beam divergence of 0.025° in the far-field region. Furthermore, it demonstrates that by implementing the double-etch step process, the radiation efficiency of such antennas can be increased up to $D = 72\%$, thereby opening up promising prospects for the design of 1D-OPAs for applications where the power budget is critical as communications or remote sensing. A summary of the geometrical parameters (Table 4.1) and simulation results (Table 4.2) of both designs are given in the following tables.

TM design	W	H	g	W_s	L_s	L_n	Λ	Λ_{SWG}	DC	L_{ant}
Single-etch	900	220	180	190	0	700	832	208	60%	3.65
Double-etch	900	220/150	155	190	600	100	832	208	60%	3.65

Table 4.1.: Geometrical parameters of TM designs. All parameters are in units of nm, except for the length of the antenna L_{ant}, which is in units of mm. The length of the antenna is estimated as the required length to radiate 99% of the input power. L_s represents the length of the shallowed lateral segment, while L_n represents the length of the non-shallowed lateral segment. In the case of the single-etch step design, the lateral segment thickness does not have a shallowed length.

TM design	n_{FB}	n_g	θ_0 (°)	D	α_{FB} (mm^{-1})	$\Delta\theta$ (°)	$\partial\theta/\partial\lambda$ (°/nm)
Single-etch	1.60	2.19	-15.7	58%	0.63	0.025	0.093
Double-etch	1.579	2.15	-16.5	72%	0.63	0.025	0.053

Table 4.2.: Simulation results of TM designs. The simulation results of the TM designs are directly related to the Floquet-Bloch mode supported by the antennas. The physical parameters are calculated for the central wavelength $\lambda = 1.55\,\mu$m and the radiation angle (θ_0) is the corresponding angle in the air. Both antennas are designed to have similar parameters, except for the directionality, which is superior in the double-etch step design.

4.1.2. Experimental validation of different antenna designs.

The second milestone in the Thesis involved the fabrication and experimental validation of the proposed designs to verify the consistency between simulations and fabricated prototypes. To accomplish this phase of the research, specialized Fourier optics systems were designed to experimentally characterize the radiation patterns of the antennas, as discussed in the previous chapter (Section 3.3.2). All the measurements and experiments realized for antenna characterization were done with the laboratory equipment described in the preceding chapter (Section 3.4.3). During this phase, three different designs of the antenna were fabricated: i) a metamaterial surface-emitting antenna for TM polarization, ii) a metamaterial surface-emitting antenna for TE polarization, and iii) a slow-light metamaterial surface-emitting antenna for TE polarization. All the prototypes were fabricated in ANT, patterned in a 220-nm thick silicon layer with a 2-µm buried oxide (BOX) layer using electron beam lithography using a single fully-etch step and a 2.2-µm thick upper SiO_2 cladding deposited by chemical vapor deposition.

The prototype of the antenna designed for TM polarization with a single-etch step exhibited a bad performance due to some anomalies observed in the laboratory. The transmitted power measured at the output of the antenna suffered from a periodic behavior when the wavelength was tuned, resulting in a polarization rotation. This issue can be attributed to a potential fabrication error of the SWG core leading to air gaps between the segments. Despite this problem, an apparent radiation pattern could be observed, and a scanning sensitivity of $\partial\theta/\partial\lambda = 0.09°$/nm was measured, which agrees with the simulation results.

The second antenna designed for TE polarization was successfully characterized in the laboratory, presenting outstanding results for a millimeter-scale antenna in SOI. Figure 4.2.b presents an overview of the design including an SEM image. The design process and experimental testing conducted to characterize this particular antenna are presented in the second publication of this Thesis titled "Millimeter-long metamaterial surface-emitting antenna in the silicon photonics platform" [110]. This publication presents for the first time the experimental results of the proposed topology for integrated optical antennas on the SOI platform. Through the use of lens systems and an IR camera, a far-field beam divergence of approximately 0.1° was measured. Furthermore, a scan range of 16° was achieved with a wavelength variation of 120 nm. The experimental results exhibited remarkable agreement with the simulations. However, it is worth noting that the measured beam divergence in the laboratory was slightly wider than the simulation, suggesting a higher radiation strength due to manufacturing errors. Nonetheless, the achieved beam divergence remains comparable to the state-of-the-art as highlighted in the publication. A summary of the geometrical parameters (Table 4.3) and simulation results (Table 4.4) of the published design are given in the following tables.

	W	H	g	W_s	L_s	Λ	Λ_{SWG}	DC	L_{ant}
Experimental TE	650	220	300	200	200	680	170	0.55	2.3

Table 4.3.: Geometrical parameters of the measured antenna for TE polarization. All parameters are in units of nm, except for the length of the antenna L_{ant}, which is in units of mm. The length of the antenna is estimated as the required length to radiate 99% of the input power.

	n_{FB}	n_g	θ_0 (°)	$\Delta\theta$ (°)	$\partial\theta/\partial\lambda$ (°/nm)
Experimental TE	1.83	3.20	-26.6	0.10	0.13

Table 4.4.: Experimental results of the measured antenna for TE polarization. The experimental results of the TE design represented here are the ones measured by experimental characterization of the antenna. The effective index is the only result measured in an indirect way through the radiation angle (θ_0). All the results of the table correspond to the central wavelength $\lambda = 1.55\,\mu$m. The corresponding estimated fabrication error is an under-etching of approximately 20 nm.

The third design that was demonstrated experimentally was the slow-light antenna. It demonstrated satisfactory performance, validating the concept of slow-light within this topology (see Fig. 4.2.c), improving the scanning sensitivity by exploiting the use of metamaterials. The measured scanning sensitivity was $\partial\theta/\partial\lambda = 0.198°/\mathrm{nm}$ which agrees with the simulation results. However, the group index could not be experimentally demonstrated as the measurements with the interferometric experiment were not conclusive. These results have not yet been published, but they will be shared in the near future or upon the development of a more advanced prototype.

4.1.3. Design and validation of a complete 1D-OPA.

The final milestone of the research conducted during the Thesis involved the development and experimental evaluation of a complete functional 1D-OPA. In this case, an antenna array comprising 112 metamaterial surface-emitting antennas was realized. The antennas used for the OPA were those that have been previously published (TE design). Moreover, the 1D-OPA developed here included a novel feeding scheme based in the use of a beam expander using a distributed Bragg deflector (DBD). The DBD was previously designed as part of a different Thesis conducted by the same research group (Photonics & RF Lab). It has been successfully employed for different applications, including serving as a mode expander for low-loss on-chip transitions and as a demultiplexer for communications [111, 112]. The DBD emits a beam into a silicon slab at a specific angle ϕ_{slab}, which illuminates the entire antenna array. The on-chip beam radiated by the DBD has a Gaussian amplitude profile with a mode field diameter (MFD) of MFD = 40 µm. As a result, each individual antenna within the array receives a unique amplitude and phase distribution due to a tapered region designed to connect the slab with the antenna array. This configuration enables beam shaping in the far-field region and facilitates beam scanning using a single control element for 112 antennas. As the DBD is a dispersive device, with a wavelength tuning both the elevation angle (θ) and azimuthal angle (ϕ) will change, but if a thermal phase shifter were used over the DBD an orthogonal 2D-scanning of the emitted beam could be possible with this architecture. The OPA was successfully fabricated and experimentally evaluated. Figure 4.2.d shows the design presented in the third publication of this Thesis titled "On-chip metamaterial antenna array with distributed Bragg deflector for generation of collimated steerable beams" [33]. For the first time a 1D-OPA using a DBD as feeding scheme was experimentally demonstrated. A summary of the experimental results of the published design are given in the following table (Table 4.5).

	Beamwidth	**Gain**	**Directivity**	$\partial\theta/\partial\lambda$	$\partial\phi/\partial\lambda$
Experimental 1D-OPA	0.2° × 1.8°	50 dB	53.8 dBi	0.13°/nm	0.23°/nm

Table 4.5.: Performance of the measured 1D-OPA for TE polarization. The experimental results are those related to the far-field radiation pattern as the beamwidth and scanning sensitivity. The antenna gain and directivity results are estimations based on simulations. The far-field spot has a Gaussian profile in the azimuthal direction due to the illumination of the OPA.

4.2. Research publications

Almost all of the designs discussed in this chapter are thoroughly documented and elaborated in three research publications that validate the Thesis. These publications are arranged chronologically, demonstrating a favorable progression throughout the development of the Thesis as it was planned. Each publication is a milestone in the process of the design of an 1D-OPA for the SOI platform using a novel topology. The publications are presented below.

1. **Highly efficient optical antenna with small beam divergence in silicon waveguides.**

   Pablo Ginel-Moreno, Daniel Pereira-Martín, Abdelfettah Hadij-ElHouati, Winnie N. Ye, Daniele Melati, Dan-Xia Xu, Siegfried Janz, Alejandro Ortega-Moñux, J. Gonzalo Wangüemert-Pérez, Robert Halir, Íñigo Molina-Fernández, Jens H. Schmid, and Pavel Cheben, "Highly efficient optical antenna with small beam divergence in silicon waveguides," Optics Letters vol. 45, no. 20, pp. 5668-5671 (2020). DOI:10.1364/OL.404012

   The first publication that endorses this work. It introduces the theoretical groundwork, showcasing the novel application of this antenna synthesis topology in SOI.

   Abstract: Optical antennas are key components in optical phased arrays for light detection and ranging technology requiring long sensing range and high scanning resolution. To achieve a narrow beam width in the far-field region, antenna lengths of several millimeters or more are required. To date, such long antennas have been impossible to achieve in silicon waveguides because currently demonstrated technologies do not allow accurate control of grating strength. Here, we report on a new type of surface-emitting silicon waveguide with a dramatically increased antenna length of $L = 3.65$ mm. This

is achieved by using a subwavelength metamaterial waveguide core evanescently coupled with radiative segments laterally separated from the core. This results in a far-field diffracted beam width of 0.025°, which is a record small beam divergence for a silicon photonics surface-emitting device. We also demonstrate that by using a design with L-shaped surface-emitting segments, the radiation efficiency of the antenna can be substantially increased compared to a conventional design, with an efficiency of 72% at the wavelength of 1550 nm.

2. **Millimeter-long metamaterial surface-emitting antenna in the silicon photonics platform.**

   Pablo Ginel-Moreno, Alejandro Sánchez-Postigo, José de-Oliva-Rubio, Abdelfettah Hadij-ElHouati, Winnie N. Ye, J. Gonzalo Wangüemert-Pérez, Íñigo Molina-Fernández, Jens H. Schmid, Pavel Cheben, and Alejandro Ortega-Moñux, "Millimeter-long metamaterial surface-emitting antenna in the silicon photonics platform," Optics Letters 46(15), 3733-3736 (2021). DOI:10.1364/OL.431983

   The second publication presents the experimental measurements of an antenna, yielding remarkable outcomes compared to the stat-of-the-art and validating the simulation methods used to characterize this large-scale structures.

   Abstract: Integrated optical antennas are key components for on-chip light detection and ranging technology (LIDAR). In order to achieve a highly collimated far field with reduced beam divergence, antenna lengths on the order of several millimeters are required. In the high-index contrast silicon photonics platform, achieving such long antennas typically demands weakly modulated gratings with lithographic minimum feature sizes below 10 nm. Here, we experimentally demonstrate a new, to the best of our knowledge, strategy to make long antennas in silicon waveguides using a metamaterial subwavelength grating (SWG) waveguide core loaded with a lateral periodic array of radiative elements. The mode field confinement is controlled by the SWG duty cycle, and the delocalized propagating mode overlaps with the periodic perturbations. With this arrangement, weak antenna radiation strength can be achieved while maintaining a minimum feature size as large as 80 nm. Using this strategy, we experimentally demonstrate a 2-millimeter-long, single-etched subwavelength-engineered optical antenna on a conventional 220 nm SOI platform, presenting a measured far-field beam divergence of 0.1° and a wavelength scanning sensitivity of 0.13°/nm.

3. **On-chip metamaterial antenna array with distributed Bragg deflector for generation of collimated steerable beams.**

   Pablo Ginel-Moreno, Abdelfettah Hadij-ElHouati, Alejandro Sánchez-Postigo, J. Gonzalo Wangüemert-Pérez, Íñigo Molina-Fernández, Jens H. Schmid, Pavel Cheben and Alejandro Ortega-Moñux, "On-chip metamaterial antenna array with distributed Bragg deflector for generation of collimated steerable beams," Laser & Photonics Reviews 16(9), 2200164 (2022).DOI:10.1002/lpor.202200164

   Lastly, the third publication details an antenna array design, highlighting its originality related to the feeding scheme, paving the wave to future design of 1D-OPAs with a large number of antennas and a single control element, reducing complexity of the whole system and using a extremely highly efficient antenna.

Abstract: The generation of collimated steerable beams of light is a fundamental function in optics needed in many applications, including free-space optical communications, remote sensing, and light detection and ranging. Implementing large-aperture light emitters directly on a photonic integrated chip without using external optics and expensive alignment systems is an outstanding challenge in integrated photonics. Here, the experimental demonstration of a new integrated antenna array architecture that uses a compact feeding circuit is reported. The design is based on an apodized Bragg deflector working as a low-loss (<0.3 dB) ultra-compact beam expander, which generates a 40-μm-wide on-chip Gaussian beam that illuminates a one-dimensional array of 112 optical antennas with a length of 1.5 mm. Each antenna comprises a metamaterial subwavelength grating waveguide core that is laterally loaded with an array of periodic radiative silicon segments. The device is fabricated on a 220-nm silicon-on-insulator platform using a single etch process with a minimum feature size of 80 nm. An antenna array with a power gain of 50 dB, a radiation efficiency of 3.8 dB, and a far-field angular divergence of 1.8° × 0.2°, in a wavelength range of 1500–1580 nm is presented.

5. Conclusions and prospects for future research

This chapter presents the main conclusions and milestones achieved through the completion of this Thesis (Section 5.1). Furthermore, it will show the current status of the work and how it will continue in the future (Section 5.2).

5.1. Conclusions

The advancement of integrated optical antennas is crucial for generating highly collimated beams from a chip. Furthermore, by arranging these antennas into arrays and having control over the complex amplitude of each element, the radiated beam can be electronically manipulated without the reliance on mechanical systems. This capability offers key characteristics required for various applications, including Free-Space Optics (FSO), Inter-Satellite Links (ISL), remote sensing, and automotive LIDAR, among others. One emerging solution gaining momentum is the development and integration of large-scale weak antennas to construct 1D-OPAs. These arrays offer a simpler alternative to their 2D counterparts in terms of circuit complexity and power efficiency while providing comparable performance. However, the development of large-scale weak antennas on silicon photonics platforms such as SOI or Si_3N_4 presents challenges, as small perturbations may result in design incompatibilities with commercial foundries.

In this Thesis, we introduce a novel topology for the SOI platform, which enables the synthesis of millimeter-scale weak antennas with a MFS compatible with commercial foundries, i.e., a laterally loaded SWG waveguide with a series of segments arranged periodically along the propagation direction. All the designs in this Thesis have been developed using this topology, and they have been developed using software tools and characterized by optical hardware systems specifically designed for this purpose. The prototypes were fabricated at Applied Nanotools Canada in MPW runs using electron beam lithography on a SOI platform with a 220-nm thick silicon layer, a 2-μm buried oxide (BOX), and a 2.2-μm thick upper SiO_2 cladding. All the prototypes did not require any additional processes, and were characterized at the Photonics & RF facilities at the University of Malaga.

As an overview of all the work developed on this Thesis the following milestones were addresed:

- Software methods were developed to efficiently design large-scale antennas with the 3D-FDTD method and estimate the shape and behavior of the far-field radiation pattern emitted by these antennas.
- Optical systems consisting of lenses have been designed with specialized software to

facilitate the characterization of far-field radiation patterns of integrated optical antennas.

- Design, fabrication and experimental characterization of different antenna designs were done, demonstrating the versatility and opportunities of this topology in the design of integrated optical antennas.
- A complete 1D-OPA was fabricated and characterized in the laboratory, demonstrating a highly directive device with a novel feeding scheme for OPAs.

Based on the extensive research conducted on millimeter-scale integrated optical antennas in this Thesis, the following key conclusions have been drawn:

1. **The use of this innovative topology enables the synthesis of large-scale integrated optical antennas with significant MFS.** By employing evanescent coupling between laterally arranged segments and a primary SWG core, a high degree of design flexibility is achieved for weakly radiating antennas. Additionally, the physically distant placement of the lateral segments allows for larger dimensions to be accommodated, offering a way to reduce the radiation strength of integrated antennas having MFS compatible with modern commercial lithography processes. The antennas were experimentally demonstrated and the performance obtained are similar to the results obtained in state-of-the-art, demonstrating the potential of the approach showed here.
2. **The design of a complete 1D-OPA has been accomplished, featuring a novel feeding scheme that is based in the use of a distributed Bragg deflector (DBD).** The 1D-OPA has been fabricated and characterized experimentally. It includes 112 metamaterial surface-emitting antennas that are separated a distance of $d = 1.45\,\mu\text{m}$. The use of DBDs for antenna arrays has been demonstrated, modulating the amplitude and phase fed to each antenna in the array with a single control element. The DBD is designed to achieve very low insertion loss and radiate a Gaussian beam to illuminate all antennas. The OPA exhibits a diagonal behavior when the radiated beam is scanned as only the wavelength is used as steering mechanism.

5.2. Future prospects

The main results of this Thesis lay the groundwork for several potential directions of future research and exploration. Here, we present a list of future prospects and areas that can be further investigated based on the findings of this study.

5.2.1. Thermal control of the DBD to achieve 2D-scanning of the radiated beam with the design of the 1D-OPA.

The main ongoing line of research focuses on the experimental characterization of the 1D-OPA design using a thermal phase shifter over the DBD. This solution allows for wavelength tuning and thermal shifting to achieve a 2D-scanning of the radiated beam. By doing so, it will be demonstrated one of the most energy-efficient solutions in SOI, as conventional OPAs typically require the use of N phase shifters for N antennas. Currently, the prototype of the 1D-OPA, along with the thermal phase shifter, has been fabricated and we are waiting to receive the chip for the characterization in the laboratory.

5.2.2. Study of further improvements in the topology.

The versatility of the proposed topology provides various approaches for improving antenna parameters. In this regard, further research will be conducted to achieve OPAs with shorter distances between antennas, to prevent the appearance of grating lobes. One approach under investigation involves the use of metamaterials between antennas to prevent coupling and be able to approach the antennas at a distance of less than $\lambda/2$. Additionally, new designs with alternative shapes for lateral segments are being considered for future investigation. The goal is to achieve larger emitters with high scanning sensitivity.

5.2.3. New approaches for designing ultra-highly efficient antennas.

A new technique is currently being patented by the Photonics & RF Lab to achieve highly efficient emitters in terms of radiation efficiency. This method is compatible with SOI and Si_3N_4 platforms and allows for a directionality of $D = 1$. The prototypes have undergone laboratory testing, and the antennas were able to emit light off-chip. However, further investigation is required to address certain technical issues. This design opens up possibilities for the utilization of integrated optical antennas as a solution for systems where radiated power is critical, such as in automotive LIDAR.

A. Derivation of the radiation pattern from Fraunhofer diffraction equation

The far-field radiation pattern of an aperture antenna that lays on the plane XY and it has a physical aperture surface D can be estimated with the Fraunhofer diffraction equation as:

$$\mathbf{f}(\phi,\theta) = \iint_D \mathbf{E_a}(x,y)e^{j(k_x x+k_y y)}\mathrm{dxdy}, \tag{A.1}$$

where $\mathbf{f}(\phi,\theta)$ is a complex vector directly related to the radiation vector of the antenna, defined as:

$$\mathbf{F_m}(\phi,\theta) = -\hat{\mathbf{z}} \times \mathbf{f}(\phi,\theta) = \hat{\mathbf{x}}f_y - \hat{\mathbf{y}}f_x. \tag{A.2}$$

The radiation vector is the Fourier transform of the current density of the antenna and it is completely defined by the spherical coordinates. The radiation vector resulted from the electric field in the aperture is defined in polar components as follows:

$$\mathbf{F_m}(\phi,\theta) = \hat{\boldsymbol{\theta}}cos(\theta)\left(f_y cos(\phi) - f_x sin(\phi)\right) - \hat{\boldsymbol{\phi}}\left(f_x cos(\phi) + f_y sin(\phi)\right). \tag{A.3}$$

To calculate the far field radiated by the antenna, the same process should be done with the magnetic field on the radiation aperture $\mathbf{E_a}(x,y)$, obtaining the complex vector $\mathbf{g}(\phi,\theta)$ and his corresponding radiation vector $\mathbf{F}(\phi,\theta)$. However, by using the Fraunhofer approximation it can be assumed that the field outside the radiative aperture is zero, thus assuming that the material around the aperture is composed of perfectly electric conductor (PEC). Under this assumption, only the electric field contained in the aperture $\mathbf{E_a}$ is needed for the calculation of the far field radiated by the antenna, defined in polar coordinates as:

$$\mathbf{E}_{\mathrm{far}}(\phi,\theta) = \hat{\boldsymbol{\theta}}E_\theta(\phi,\theta) + \hat{\boldsymbol{\phi}}E_\phi(\phi,\theta), \tag{A.4}$$

where each component of the electric field vector is defined as:

$$E_\theta = 2jk\frac{e^{-jkr}}{4\pi r}\left[f_x cos(\phi) + f_y sin(\phi)\right], \tag{A.5}$$

$$E_\phi = 2jk\frac{e^{-jkr}}{4\pi r}\left[cos(\theta)\left(f_y sin(\phi) - f_x cos(\phi)\right)\right]. \tag{A.6}$$

Finally, to calculate the radiation pattern of the antenna in terms of intensity, it will be defined as the square of the magnitude of the electric field:

$$U(\phi,\theta) = |E_\theta|^2 + |E_\phi|^2. \tag{A.7}$$

B. Resumen en Español

B.1. Introducción

B.1.1. Fotónica del silicio para la sociedad de la información

Nuestra actual sociedad de la información se basa fundamentalmente en dos tecnologías clave que surgieron hace más de 50 años: los circuitos integrados monolíticos y las comunicaciones ópticas de alta capacidad. Estas tecnologías han desempeñado un papel vital en el desarrollo de nuestro mundo moderno. Un aspecto notable de estas tecnologías es su rápida evolución, tal y como demuestra la Ley de Moore en el ámbito de los microprocesadores, donde el número de transistores de un microprocesador se duplica cada dos años [1]. Del mismo modo, las comunicaciones ópticas están experimentando un notable crecimiento en la capacidad de enlace, viéndose incrementada en un factor 10 cada cuatro años [2]. Estos avances continuos han sido decisivos para impulsar el progreso incesante y fomentar la innovación, definiendo así el panorama tecnológico en constante evolución por el que navegamos hoy en día.

La óptica integrada siempre ha sido proclive a revolucionar este campo fusionando a la perfección diversas funcionalidades en un mismo circuito integrado fotónico (PIC) compacto. Este enfoque innovador aprovecha las múltiples ventajas de la escalabilidad, como la reducción significativa del tamaño, el peso y los gastos de fabricación. Además, la integración permite realizar funciones complejas que, de otro modo, serían inviables con componentes discretos. Hasta principios de este siglo, el desarrollo de los PIC ha sido relativamente lento en comparación con el avance de la microelectrónica, ya que sólo unos pocos nichos de aplicación irrumpieron con claridad en el panorama tecnológico, como los láseres semiconductores III-V [3], moduladores de niobato de litio [4], demultiplexores de longitud de onda basados en agrupaciones de guías de ondas (AWG) [5] y rejillas *echelle* [6]. Sin embargo, el contexto tecnológico actual ha experimentado un cambio radical en los últimos años con la aparición de la fotónica de silicio.

El silicio es el material fundamental de esta tecnología, que tiene la propiedad de ser transparente en una amplia gama de longitudes de onda utilizadas en las comunicaciones ópticas. La figura B.1 muestra una guía de onda típica *photonic-wire* sobre la plataforma tecnológica silicio sobre aislante (SOI), en la que el núcleo de silicio ($n_{\mathrm{Si}} \sim 3{,}45$) está rodeado de dióxido de silicio ($n_{\mathrm{SiO_2}} \sim 1{,}45$). El elevado contraste de índices ($\Delta n \sim 2$) implica el uso de guías de onda de muy pequeñas dimensiones (cientos de nanómetros) para mantener el régimen monomodo y conduce a radios de curvatura muy compactos, del orden de sólo $5\,\mu m$, lo que reduce el tamaño de los circuitos integrados en el chip. Para longitudes de onda inferiores a 1100 nm, en las que el silicio ya no es transparente, o cuando se necesitan altos niveles de potencia, otras plataformas tecnológicas se imponen sobre SOI. Algunos ejemplos son las plataformas con nitruro de silicio ($n_{\mathrm{SiN}} \sim 2$), ya que son compatibles con

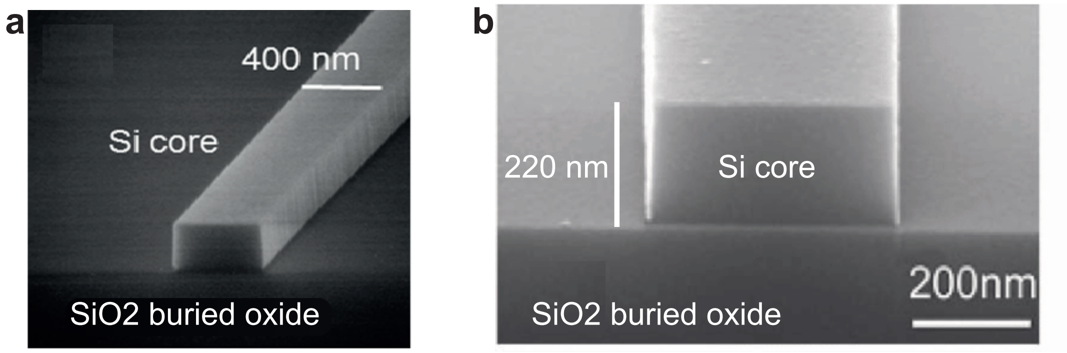

Figure B.1.: Imagen SEM de una guía de onda *photonic-wire* convencional sobre la plataforma SOI. a) Perspectiva 3D de la guía de onda antes de depositar un revestimiento de SiO_2 sobre ella. b) Imagen transversal de la guía de onda. Fuente de las imágenes [11, 12].

los procesos de fabricación estándar.

Pese a que la fotónica del silicio junto con plataformas como SOI presentan una serie de características idóneas para el desarrollo de nuevas aplicaciones integradas, este tipo de plataformas carece de flexibilidad, ya que están restringidas al uso de sólo dos materiales silicio y dióxido de silicio. Esto, unido a su elevado contraste de índice, plantea algunos problemas a la hora de diseñar dispositivos complejos de alto rendimiento. Recientemente se han dedicado importantes esfuerzos a desarrollar tecnologías que permitan la implementación de metamateriales artificiales compatibles con los procesos de fabricación estándar en fotónica de silicio. Entre el abanico de posibles enfoques, el más exitoso se basa en las estructuras de rejilla de sublongitud de onda (SWG) [27–29]. Un SWG es un material artificial nanoestructurado con características ópticas determinadas por su geometría que, cuando se diseña adecuadamente, mejora el rendimiento del dispositivo en términos de eficiencia, ancho de banda y manejo de la polarización, al tiempo que mantiene la compatibilidad con las técnicas de fabricación estándar.

Esta Tesis se centra en el diseño de antenas ópticas integradas basadas en metamateriales SWG para la generación y control de haces altamente colimados emitidos desde chips fotónicos. Las antenas ópticas integradas son elementos fundamentales para muchas aplicaciones, como las interconexiones ópticas, los sistemas LIDAR en chip, la teledetección y las comunicaciones ópticas en espacio libre. Normalmente, las antenas ópticas integradas se diseñan como guías de rejilla con una topología específica para conseguir un comportamiento de radiación concreto en términos de directividad, dirección de radiación o divergencia angular. Sin embargo, existen muchos otros mecanismos diferentes para controlar la emisión de haces ópticos desde antenas de estado sólido, como las nanoantenas plasmónicas [36–38], rejillas de cristal líquido [39, 40] o emisores controlados por sistemas microelectromecánicos (MEMS) [22, 41]. Sin embargo, una solución de estado sólido que ha ganado mucho impulso en los últimos años es el uso de antenas ópticas integradas para la formación de agrupaciones de antenas controladas por fase (OPAs). Con esta solución se consigue emitir haces altamente colimados y manipular electrónicamente la dirección de radiación del haz sin necesidad de ningún sistema mecánico. Hay muchas arquitecturas diferentes para implementar OPAs como los OPAs unidimensionales (OPA-1D) [43–46, 50], los OPAs bidimensionales (OPA-2D) [48, 49, 51, 113], agrupaciones de antenas dispersadas [52–54], agrupaciones de antenas en planos focales [22, 55], agrupaciones circulares [56], entre otros. En los últimos años se ha publicado un importante número de trabajos recopilatorios que corroboran la creciente popularidad de este tipo de estructuras [57–60].

Las dos arquitecturas más comunes utilizadas en el estado del arte son el OPA-2D y el OPA-1D (ver Fig. B.2). Las principales diferencias entre ellos son las siguientes: El OPA-2D consta de una matriz de antenas de $N \times N$ dispuestas uniformemente tanto en la dirección transversal (y) como en la longitudinal (x). Como resultado, las antenas utilizadas en los OPAs-2D suelen ser cortas y requieren una alta potencia de radiación. Por otro lado, el OPA-1D consiste en una agrupación de antenas dispuestas únicamente en la dirección transversal (y), lo que requiere antenas más débiles con longitudes mayores, generalmente de unos pocos milímetros o miles de longitudes de onda ($> 1000\lambda$). En cuanto al diagrama de radiación, el OPA-2D permite manipular la forma del diagrama y dirigir el haz hacia cualquier dirección deseada en el espacio (θ_0, ϕ_0) mediante la aplicación de desfases entre antenas adyacentes de manera electrónica. Por el contrario, el OPA-1D requiere la aplicación de desfases entre antenas junto con ajustes de la longitud de onda para dirigir el haz radiado hacia un punto arbitrario en el espacio.

En resumen los OPA-2D permiten tener un sistema integrado que emita haces altamente colimados hacia una dirección deseada a una longitud de onda fija. Sin embargo, sus esquemas de alimentación y de desfase son muy complejos y suele ser muy complicado conseguir agrupaciones sin sufrir de lóbulos secundarios perjudiciales para el diagrama de radiación. Por ello, la solución OPA-1D a pesar de necesitar variar la longitud de onda para realizar el apuntamiento de haces ópticos, es una solución más sencilla a nivel de sistema, y por lo tanto más eficiente. En la Fig. B.2 se representan de manera esquemática estas dos soluciones para realizar agrupaciones de antenas controladas por fase en plataformas de SOI.

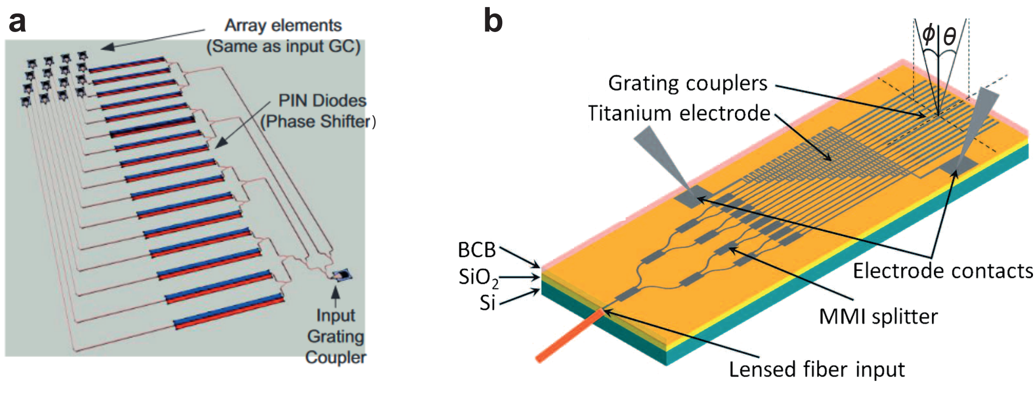

Figure B.2.: Configuraciones típicas de agrupaciones de antenas controladas por fase (OPA). a) OPA-2D compuesto por 4×4 elementos radiantes (antenas cortas con alta fuerza de radiación) y 16 desfasadores para control del apuntamiento del haz emitido [61]. b) OPA-1D compuesto de 16 antena unidimensionales (antenas largas de radiación débil) y 16 desfasadores para control del apuntamiento del haz en la dirección azimutal (ϕ). El apuntamiento en la dirección vertical (θ) requiere de un ajuste en longitud de onda [42].

B.1.2. Resumen y contribuciones de esta Tesis

El objetivo principal de la investigación llevada a cabo en esta Tesis es el desarrollo de antenas de superficie asistidas por metamateriales SWG para conseguir aperturas a escala milimétrica en plataformas de fotónica del silicio. Estas antenas han sido específicamente diseñadas para porder formar agrupaciones de antenas unidimensionales controladas por fase (OPA-1D). En las guías de onda de silicio sobre aislante de alto contraste, es extremadamente difícil implementar antenas de radiación débil, con longitudes de varios milímetros o más, sin utilizar perturbaciones con tamaños del orden de decenas de nanómetros [62, 63]. En este trabajo se han abordado los retos más relevantes de este tipo de antenas, obteniendo en todos los casos soluciones innovadoras. Como prueba de concepto, se ha propuesto y demostrado experimentalmente por primera vez un concepto radicalmente nuevo para la formación de una agrupación de antenas unidimensional (OPA-1D). Esta solución se caracteriza por utilizar un novedoso esquema de alimentación para iluminar 112 antenas, basado en un deflector de Bragg distribuido (DBD) para irradiar eficazmente haces colimados y orientarlos desde chips fotónicos de silicio utilizando un único elemento de control.

Las principales contribuciones de esta Tesis se han materializado en tres publicaciones en revistas indexadas en el Journal Citation Reports (JCR) [33, 109, 110] y seis conferencias nacionales e internacionales revisadas por pares, en cuatro de las cuales el candidato ha sido el primer autor. Además, el candidato es co-inventor de una patente relacionada con las topologías de las antenas de superficie presentadas en esta Tesis [114]. De acuerdo con las regulaciones de los estudios doctorales en la Universidad de Málaga, se propone que las mencionadas publicaciones respalden la presentación de esta Tesis como un compendio de publicaciones.

B.1.3. Contribuciones

Todas las contribuciones de la Tesis se resumen en la Figura B.3, donde se presentan brevemente las principales características de cada diseño realizado. Además, en la figura se incluyen las tres publicaciones que respaldan esta Tesis.

Antenas de superficie diseñadas con metamateriales SWG

En esta Tesis se presenta una nueva topología para el desarrollo de antenas débilmente radiantes en plataformas de alto contraste como SOI. Esta topología implica el uso de un núcleo de rejilla sublongitud de onda (SWG) junto con segmentos laterales acoplados evanescentemente que se disponen de manera periódica a lo largo de la dirección de propagación, lo que permite la radiación eficiente del modo fuera del chip. La separación de los segmentos laterales con el núcleo SWG proporciona un mecanismo altamente preciso para controlar la fuerza de radiación de las antenas. Con este enfoque innovador, se pueden diseñar antenas con longitudes de milímetros sin estar limitadas por los tamaños mínimos de fabricación, ya que usando esta topología los tamaños de bloque pueden ser significativamente grandes.

Se han desarrollado diversos diseños de antenas a lo largo de la Tesis (ver Figura B.3). Estos diseños incluyen: i) Antenas de superficie altamente eficientes diseñadas específicamente para la polarización TM. ii) Antenas de superficie optimizadas para la polarización

TE. iii) Antenas de superficie de luz lenta diseñadas específicamente para la polarización TE. Cada diseño posee características distintas, pero todas las antenas comparten un elemento en común: la topología que permite la realización de antenas compactas a gran escala en plataformas SOI mientras emiten haces altamente colimados con divergencias del haz inferiores a $\Delta\theta = 0.2°$. La mayoría de las ideas desarrolladas en esta Tesis se han fabricado y caracterizado experimentalmente, demostrando una concordancia satisfactoria con los resultados de modelado y simulación.

Agrupación de antenas unidimensional (OPA-1D) alimentada por un deflector de Bragg distribuido

El objetivo final de la investigación realizada durante la Tesis fue el desarrollo y la evaluación experimental de una agrupación de antenas OPA-1D completa como prueba de concepto. En este caso, se realizó una agrupación de antenas que comprende 112 antenas de superficie con metamateriales. El diseño presentó en experimentación una directividad de 53 dBi con un haz emitido con perfil gaussiano y divergencia angular de $0.2° \times 1.8°$, dando así un resultado concorde con las simulaciones. Además, el OPA-1D desarrollado incluía un nuevo esquema de alimentación basado en el uso de un expansor de haz utilizando un deflector de Bragg distribuido (DBD). Esta configuración permite la formación de haces altamente colimados y facilita el escaneo del haz utilizando un solo elemento de control. Por lo que su diseño y validación experimental se considera una de las aportaciones más relevantes de esta Tesis.

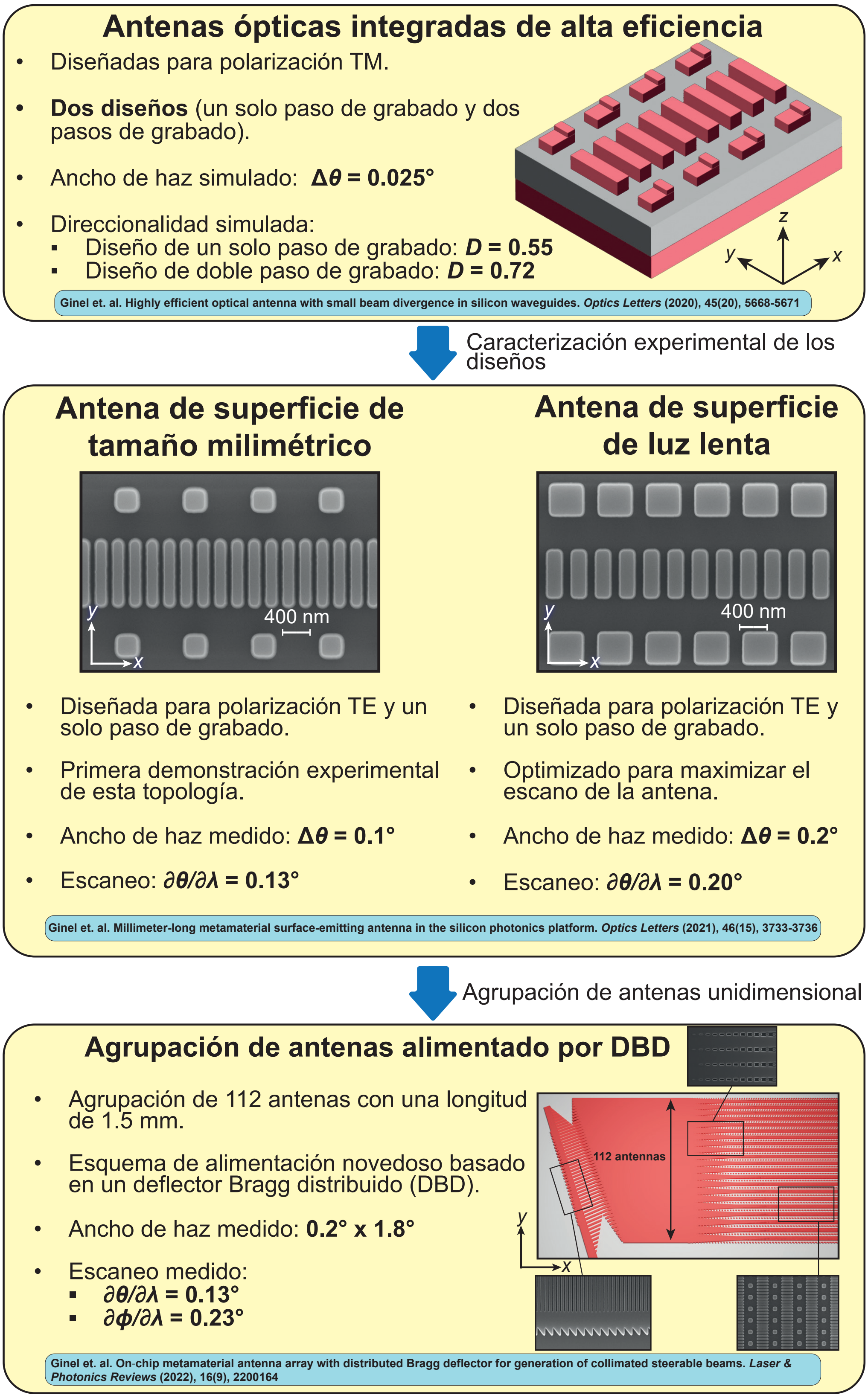

Figure B.3.: Resumen de las contribuciones presentadas en esta Tesis

B.1.4. Metodología para el diseño de antenas

El diseño y caracterización de las antenas de superficie con metamateriales desarrolladas en esta Tesis han requerido implementar nuevos métodos y herramientas tanto en el ámbito del modelado y simulación como en el campo experimental.

Desarrollo de herramientas numéricas para el diseño de antenas ópticas

El diseño de antenas de superficie requiere métodos de simulación específicos para reducir el tiempo de prototipado. Esto se debe a las grandes dimensiones de estas antenas, del orden de milímetros, que pueden hacer que las simulaciones electromagnéticas sean computacionalmente inviables. Por lo tanto, un logro importante en este trabajo fue el diseño y la optimización de un método de análisis Floquet-Bloch que puede analizar el comportamiento de toda la antena, a partir de la simulación de un único periodo, sin la necesidad de simular toda la estructura. Otra contribución significativa para reducir el tiempo de simulación fue el desarrollo de herramientas numéricas para calcular el diagrama de radiación de las antenas. Por lo general, calcular el diagrama de radiación en campo lejano requiere aplicar métodos matemáticos, como la aproximación de Fraunhofer, a los datos del campo cercano. Por lo tanto, se requiere una simulación de toda la estructura. Sin embargo, uno de los objetivos de esta Tesis es el diseño de un método numérico que aproveche los resultados obtenidos del análisis Floquet-Bloch, que simula un solo período de la estructura, para calcular el diagrama de radiación de las antenas sin la necesidad de sintetizar todo el campo cercano, ahorrando así una gran carga computacional.

Diseño y montaje de configuraciones experimentales para caracterizar las antenas

Se diseñaron y ensamblaron dos configuraciones experimentales diferentes para caracterizar el patrón de radiación de las antenas fabricadas. Las configuraciones consisten en lentes ópticas y una cámara infrarroja. En la primera configuración, se utiliza una sola lente para observar el patrón de radiación en el campo lejano y evaluar la capacidad de escaneo de la antena. Mientras que la segunda configuración involucra dos lentes. Este sistema de lentes tiene como objetivo lograr una amplificación significativa del patrón de radiación en el campo lejano, lo que permite una medición precisa de la anchura del lóbulo principal. Utilizando estas dos configuraciones diferentes, la antena puede ser caracterizada con la medición de diferentes figuras de mérito como la dirección de radiación, la sensibilidad de escaneo y la divergencia del haz. Ambas configuraciones se muestran en la Figura B.4 junto con el chip que incluye las diferentes antenas, demostrando la compacidad del montaje experimental.

B.2. Resultados de las aportaciones de esta Tesis

En esta sección se muestra un resumen de los resultados obtenidos durante la Tesis. Se incluyen de manera ordenada, comenzando por el modelado de la topología presentada y la obtención de resultados en simulación. Tras realizar una verificación a través de simulaciones electromagnéticas de la topología propuesta para la plataforma SOI, se avanza a la

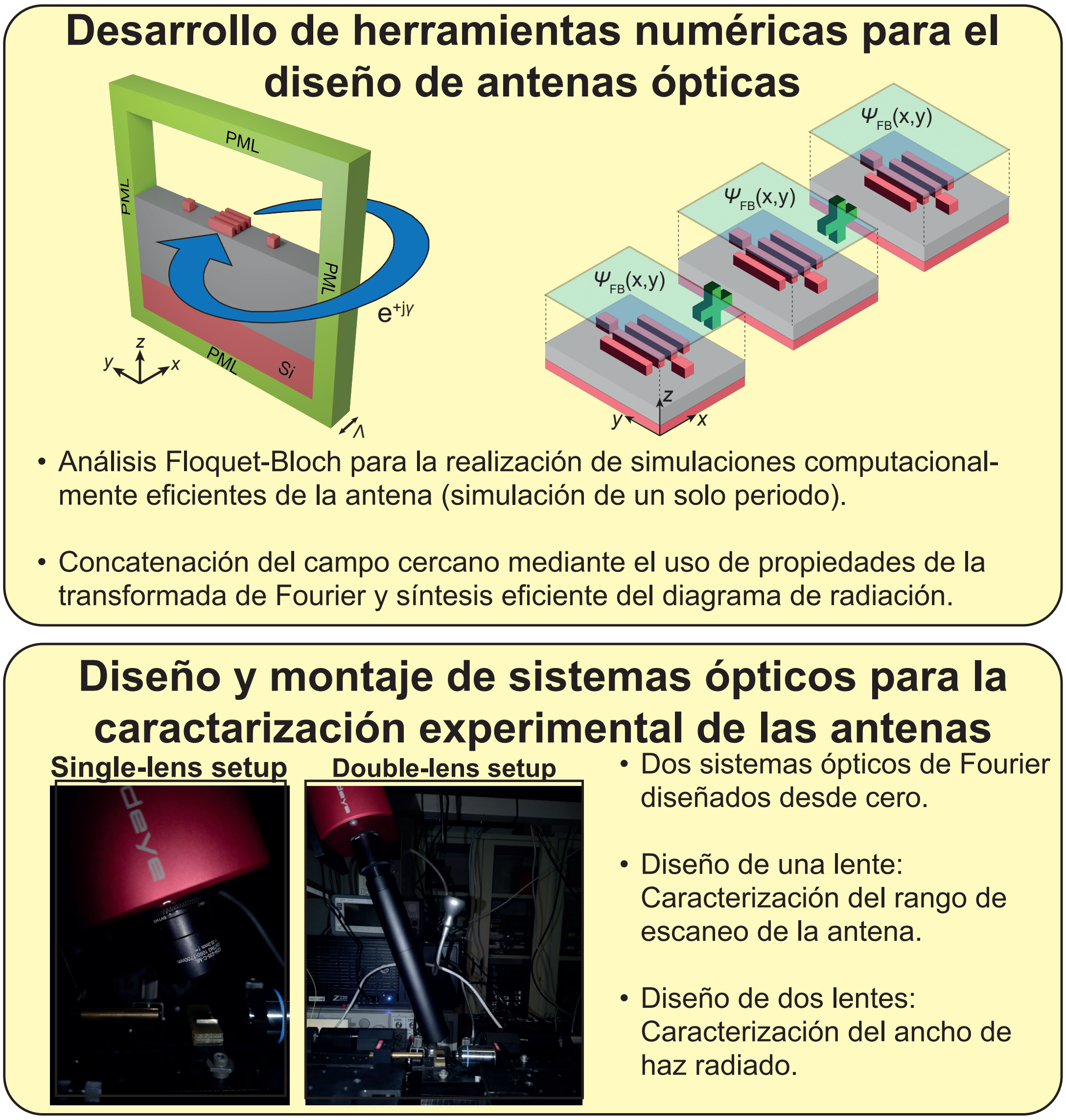

Figure B.4.: Resumen de la metodología desarrollada durante la Tesis. Breve resumen de los métodos y procedimientos usados para llevar a cabo el diseño y la caracterización experimental de los diferentes diseños de antenas ópticas integradas presentadas en este trabajo.

fase de fabricación y prototipado, donde se demuestra satisfactoriamente el funcionamiento de las antenas a través de la caracterización experimental. Los resultados de este trabajo acaban con una prueba de concepto en la que se desarrolla una agrupacion de antenas unidimensional controladas por fase (OPA-1D), que consta de 112 antenas con longitudes milimétricas y alimentadas con un esquema novedoso basado en un deflector Bragg distribuido (DBD).

Equipamiento de laboratorio

Los resultados relacionados con la caracterización experimental de las antenas no hubieran sido posible sin contar con las instalaciones del Photonics & RF Laboratory de la Universidad de Málaga. La configuración experimental utilizada con este propósito se divide en tres etapas diferentes, resumidas con fotografías en la Fig. B.5.

Etapa de entrada

La etapa de entrada se encarga de dirigir la luz desde una fuente de láser externa hasta el chip. La fuente externa es el láser sintonizable Agilent 81600B que inyecta la luz en una fibra SMF-28. Se utiliza un controlador de polarización (FPC561 de Thorlabs) para alinear la luz polarizada linealmente del láser con un filtro de polarización. La luz linealmente polarizada en la salida del filtro se guía hacia otro controlador de polarización (FPC561 de Thorlabs) que alinea la polarización de la fibra con la polarización deseada en el chip. Finalmente, antes de llegar al chip, la fibra se conecta a un circulador óptico cuyas salidas son una fibra que inyecta la luz en el chip y un fotodiodo para medir las reflexiones procedentes del chip.

Etapa del chip

La etapa del chip se encarga de acoplar la luz al chip y de extraerla fuera del chip. Para este trabajo, se han utilizado acopladores de borde lateral (*edge couplers*). Una fibra con lente se conecta a la salida del circulador, guiando la luz hacia el acoplador en la cara de entrada del chip. En la cara de salida del chip, otro acoplador guiará la luz hacia el espacio libre y un objetivo de microscopio recogerá y colimará la luz.

Etapa de salida

La etapa de salida se divide en dos caminos diferentes. El primer camino se utiliza para la caracterización de dispositivos en el chip utilizando el método de *cut-back* y para la alineación de la fibra con lente de entrada y el objetivo de microscopio de salida con los correspondientes acopladores *edge coupler*. Toda la luz recogida por el objetivo de microscopio se colima y se guía hacia un polarizador Glan-Thompson y luego a un fotodetector (818-IR). Un espejo plegable se puede utilizar para enfocar la luz en una cámara y ayudar en la alineación. El segundo camino implica el uso de los sistemas de lentes, que consiste en un sistema separado colocado sobre el chip para la caracterización de los patrones de radiación de la antena.

B.2.1. Resultados de los diseños de antenas

Todos los diseños de antena realizados en esta Tesis comparten la misma topología para el desarrollo de antenas de radiación débil en la plataforma SOI. Esta topología implica el uso de un núcleo SWG en conjunto con segmentos laterales acoplados evanescentemente que se disponen de manera periódica a lo largo de la dirección de propagación, lo que permite la radiación eficiente del modo fuera del chip (ver Figura B.6). La separación de los

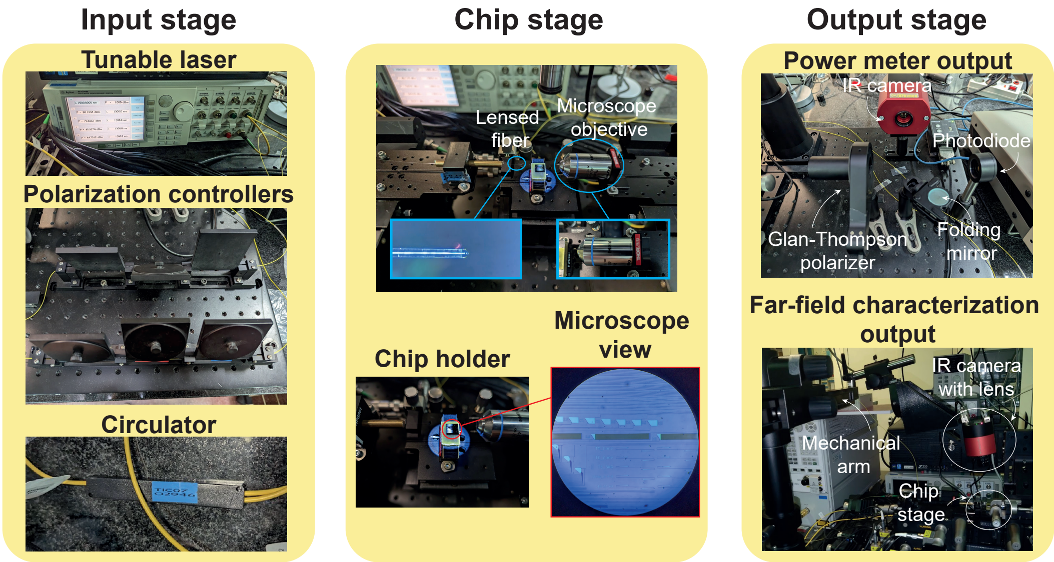

Figure B.5.: Diferentes etapas de la configuración del laboratorio para caracterizar chips fotónicos. En la etapa de entrada se muestran fotografías de los elementos principales como la fuente láser, los controladores de polarización y el circulador que se coloca en el último tramo antes de inyectar luz al chip. En la etapa del chip se muestra la fibra con lente que inyecta luz a la entrada por un lado del chip y el objetivo de microscopio que recoge la luz al otro lado del chip. Por último, se muestran dos setups diferentes en la etapa de salida, el correspondiente con el elineamiento y alimentación de dispositivos convencionales, y el diseñado para caracterizar el diagrama de radiación de las antenas.

segmentos laterales con el núcleo SWG (g) proporciona un mecanismo altamente preciso para controlar la intensidad de radiación de las antenas. Con este enfoque innovador, se pueden diseñar antenas de tamaño milimétrico sin estar limitadas por las restricciones de fabricación, ya que el tamaño mínimo de bloque del dispositivo puede ser significativamente grande. La última aportación de esta Tesis se centra en el diseño y caracterización de un OPA-1D completo, el cual aprovecha el uso de estas antenas de superficie metamaterial para formar una agrupación de antenas con una alta directividad y la capacidad de dirigir electrónicamente el haz radiado, eliminando la necesidad de ajustes mecánicos. Además, este OPA presenta un novedoso esquema de alimentación que utiliza un deflector de Bragg distribuido como expansor de haz, proporcionando una solución compacta y eficiente que se aparta de los enfoques convencionales. Estos avances posicionan a estas antenas como componentes fundamentales en diversas aplicaciones de direccionamiento de haz, como Óptica en Espacio Libre y teledetección.

Los resultados obtenidos durante la Tesis se pueden agrupar en tres diseños, los cuales se encuentran en las publicaciones que avalan esta Tesis.

Antenas ópticas integradas de alta eficiencia

Los resultados iniciales obtenidos en la Tesis se centran en el diseño de una antena de superficie metamaterial para polarización TM. Con el objetivo de llegar a un diseño que permitiese emitir haces altamente colimados (aperturas de milímetros) y pudiera escanear un área razonable ($\sim 10°$). A medida que los métodos de simulación se volvieron más refinados

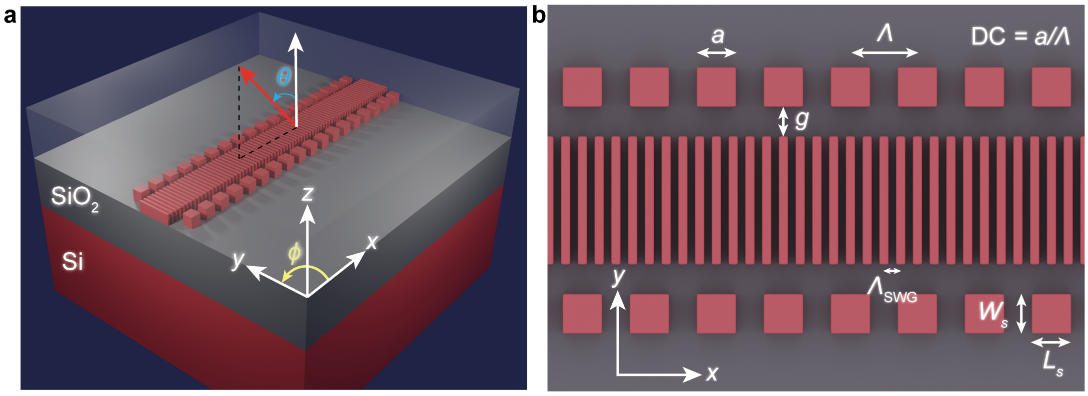

Figure B.6.: Topología de antena de superficie propuesta en esta Tesis. a) Esquemático 3D. b) Vista cenital de la estructura.

y precisos, se exploró aún más el potencial de la topología, lo que llevó a la investigación de técnicas innovadoras como diseños de doble grabado para mejorar la eficiencia de radiación. El primer hito de esta Tesis se centra en todo el proceso de diseño junto con los resultados simulados tanto para la antena de un solo paso de grabado como para su alternativa de radiación eficiente lograda mediante el proceso de doble grabado [109]. Este resultado marca la primera aparición de la topología propuesta para antenas de radiación débil, mostrando una longitud de antena sin precedentes de 3.65 mm para antenas emisoras de superficie basadas en silicio en simulación. El diseño correspondiente produce una divergencia del haz de sólo 0.025° en la región del campo lejano. Además, demuestra que al implementar el proceso de doble grabado, la eficiencia de radiación de dichas antenas puede aumentar hasta $D = 72\%$, abriendo así perspectivas prometedoras para el diseño de 1D-OPAs en aplicaciones donde el presupuesto de energía es crítico, como comunicaciones o teledetección. El proceso de diseño y los resultados de simulación se presentan en la primera publicación que avala esta Tesis [109].

Caracterización experimental de antenas de superficie metamateriales de tamaño milimétrico

El segundo hito en la Tesis implicó la fabricación y validación experimental de los diseños propuestos para verificar la consistencia entre las simulaciones y los prototipos fabricados. Para llevar a cabo esta fase de la investigación, se diseñaron sistemas especializados de óptica de Fourier para caracterizar experimentalmente los patrones de radiación de las antenas. Todas las mediciones y experimentos realizados para la caracterización de las antenas se llevaron a cabo con el equipo de laboratorio descrito anteriormente. Durante esta fase, se fabricaron tres diseños diferentes de la antena: i) una antena de superficie metamaterial para polarización TM, ii) una antena de superficie metamaterial para polarización TE, y iii) una antena de superficie metamaterial de luz lenta para polarización TE. Todos los prototipos se fabricaron en Applied Nanotools, con un proceso de fabricación SOI, con una capa de silicio de espesor de 220 nm y una capa de óxido inferior (BOX) de 2 µm utilizando litografía de haz de electrones (*e-beam*) con un solo paso de grabado completo y un recubrimiento de 2.2 µm de espesor de SiO_2 depositado por deposición química en fase vapor (CVD).

La antena diseñada para polarización TE fue caracterizada exitosamente en el laboratorio, presentando resultados destacados para una antena a escala de milímetros en SOI. El proceso de diseño y las pruebas experimentales realizadas para caracterizar esta antena en particular se presentan en la segunda publicación que avala esta Tesis [110]. Esta publicación presenta por primera vez resultados experimentales de la topología propuesta para antenas ópticas integradas en la plataforma SOI. Mediante el uso de sistemas de lentes y una cámara infrarroja, se midió una divergencia de haz en el campo lejano de 0.1°. Además, se logró un rango de escaneo de 16° con una variación de longitud de onda de 120 nm. Los resultados experimentales mostraron una notable concordancia con las simulaciones. Sin embargo, cabe destacar que la divergencia de haz medida en el laboratorio fue ligeramente mayor que la simulada, lo que sugiere una mayor fuerza de radiación debido a errores de fabricación. No obstante, la divergencia de haz alcanzada sigue siendo comparable al estado del arte, como se destaca en la publicación.

Agrupacion de antenas controladas por fase unidimensional (OPA-1D)

El último hito de la investigación llevada a cabo durante la Tesis involucró el desarrollo y evaluación experimental de un OPA-1D funcional completo. En este caso, se realizó un conjunto de antenas compuesto por 112 antenas emisoras de superficie metamaterial. Las antenas utilizadas para el OPA fueron aquellas que han sido publicadas previamente (diseño TE). Además, el OPA-1D desarrollado incluye un esquema de alimentación novedoso basado en el uso de un expansor de haz utilizando un deflector de Bragg distribuido (DBD). El DBD fue propuesto originalmente en una Tesis diferente realizada por el mismo grupo de investigación (Photonics & RF Lab). Ha sido utilizado con éxito para diferentes aplicaciones, como un expansor de modo para transiciones en chip de bajas pérdidas y como un demultiplexor para comunicaciones [111, 112]. El DBD emite un haz en un *slab* de silicio a un ángulo específico ϕ_{slab}, que ilumina todo el conjunto de antenas. El haz radiado en chip por el DBD tiene un perfil de amplitud gaussiano con un ancho MFD = 40 μm. Como resultado, cada antena individual dentro del conjunto recibe una distribución única de amplitud y fase debido a una transición adiabática diseñada especialmente para conectar el *slab* con el conjunto de antenas. Esta configuración permite modificar la forma del haz en la región del campo lejano y facilita el escaneo del haz utilizando un solo elemento de control para las 112 antenas. Como el DBD es un dispositivo dispersivo, con una sintonización de longitud de onda tanto el ángulo de elevación (θ) como el ángulo azimutal (ϕ) cambiarán, pero si se utiliza un desfasador térmico sobre el DBD, sería posible lograr un escaneo bidimensional ortogonal del haz emitido con esta arquitectura. El OPA fue fabricado y evaluado experimentalmente con éxito y los resultados se incluyen en la tercera publicación que avala esta Tesis [33].

B.3. Conclusiones y líneas futuras

B.3.1. Conclusiones

El avance de las antenas ópticas integradas es crucial para generar haces altamente colimados desde un chip. Además, al disponer estas antenas en matrices y tener control sobre la amplitud compleja de cada elemento, el haz radiado puede ser manipulado electrónicamente sin depender de sistemas mecánicos. Esta capacidad ofrece características clave requeridas para diversas aplicaciones, incluyendo óptica en espacio libre, enlaces intersatelitales, teledetección y LIDAR para coches autónomos, entre otras. Una solución emergente que está ganando impulso es el desarrollo e integración de antenas débiles de gran escala para construir OPAs unidimensionales. Estas agrupaciones de antenas ofrecen una alternativa más sencilla a sus contrapartes bidimensionales en términos de complejidad del circuito y eficiencia energética, al tiempo que proporcionan un rendimiento comparable. Sin embargo, el desarrollo de antenas débiles de gran escala en plataformas de fotónica de silicio como silicio sobre aislante o de nitruro de silicio sobre aislante presentan desafíos. Esto se debe a que conseguir antenas débiles requiere del uso de perturbaciones muy débiles en la apertura radiante, lo que puede resultar en incompatibilidades de diseño con procesos de litografía comerciales.

En esta Tesis, se presenta una nueva topología para la plataforma SOI, que permite la síntesis de antenas débiles a escala de milímetros con un tamaño de bloque compatible con fábricas comerciales, mediante una guía de onda SWG cargada lateralmente con una serie de segmentos dispuestos periódicamente a lo largo de la dirección de propagación. Todos los diseños en esta Tesis se basan en esta topología, y se han desarrollado utilizando herramientas de software y caracterizado mediante sistemas de hardware óptico diseñados específicamente para este propósito. Los prototipos se fabricaron en Applied Nanotools utilizando litografía de haz de electrones en una plataforma SOI con una capa de silicio de 220 nm de grosor, óxido inferior (BOX) de 2 μm y un recubrimiento superior de dióxido de silicio de 2.2 μm de grosor. Todos los prototipos no requirieron ningún proceso adicional y se caracterizaron en las instalaciones de Photonics & RF Laboratory en la Universidad de Málaga.

El trabajo desarrollado en esta Tesis ha abordado y cumplido una serie de hitos resumidos a continuación:

- Se desarrollaron métodos de software para diseñar eficientemente antenas a gran escala utilizando simulaciones electromagnéticas con el método FDTD aplicadas a un solo periodo de la estructura, y con ello se pudo estimar la forma y el comportamiento del diagrama de radiación de campo lejano emitido por estas antenas.
- Se han diseñado sistemas ópticos que consisten en lentes con software especializado para facilitar la caracterización de los diagramas de radiación de campo lejano de las antenas ópticas integradas.
- Se realizaron el diseño, la fabricación y la caracterización experimental de diferentes diseños de antenas, demostrando la versatilidad y las oportunidades de esta topología en el diseño de antenas ópticas integradas.
- Se fabricó y caracterizó en el laboratorio un OPA unidimensional completo, demostrando un dispositivo altamente directivo con un esquema de alimentación novedoso para OPAs.

Basándose en la extensa investigación realizada sobre antenas ópticas integradas a escala milimétrica en esta Tesis, se han obtenido las siguientes conclusiones.

1. **El uso de esta innovadora topología permite la síntesis de antenas ópticas integradas a gran escala compatible con procesos de litografía comerciales.**

Al emplear el acoplamiento evanescente entre segmentos dispuestos lateralmente y un núcleo principal SWG, se logra un alto grado de flexibilidad de diseño para antenas débilmente radiantes. Además, la ubicación físicamente distante de los segmentos laterales permite acomodar dimensiones más grandes, ofreciendo una forma de reducir la intensidad de radiación de las antenas integradas con tamaños compatibles con los procesos modernos de litografía comercial. Las antenas se demostraron experimentalmente y su rendimiento obtenido es estado del arte, lo que demuestra el potencial del enfoque presentado aquí.

2. **Se ha logrado el diseño de un OPA unidimensional completo, con un esquema de alimentación novedoso basado en el uso de un deflector de Bragg distribuido.**

   El OPA-1D ha sido fabricado y caracterizado experimentalmente. Incluye 112 antenas de superficie de metamateriales que están separadas por una distancia de $d = 1.45\,\mu\text{m}$. Se ha demostrado el uso de DBDs para matrices de antenas, modulando la amplitud y fase alimentada a cada antena de la matriz con un solo elemento de control. El DBD está diseñado para lograr una pérdida de inserción muy baja y emitir un haz gaussiano que ilumina todas las antenas. El OPA muestra un comportamiento diagonal cuando se escanea el haz radiado, ya que solo se ha demonstrado en laboratorio el escaneo con la longitud de onda como mecanismo de dirección.

B.3.2. Perspectivas futuras

Los principales resultados de esta Tesis sientan las bases para varias direcciones potenciales de futura investigación y exploración. A continuación, presentamos una lista de perspectivas futuras y áreas que pueden investigarse aún más basándose en los hallazgos de este estudio.

Control térmico del DBD para lograr el escaneo en 2D del haz radiado con el diseño del OPA-1D.

La principal línea de investigación en curso se centra en la caracterización experimental del diseño del OPA-1D utilizando un desfasador térmico sobre el DBD. Esta solución permite la sintonización de la longitud de onda y el desfase térmico para lograr un escaneo bidimensional del haz radiado. Al hacerlo, se demostrará una de las soluciones más eficientes en términos de energía en SOI, ya que los OPA convencionales típicamente requieren el uso de N desfasadores para N antenas. Actualmente, el prototipo del OPA 1D, junto con el desfasador térmico, ha sido fabricado y estamos esperando recibir el chip para la caracterización en el laboratorio.

Estudio de mejoras adicionales en la topología.

La versatilidad de la topología propuesta ofrece diversas aproximaciones para mejorar los parámetros de la antena. En este sentido, se llevarán a cabo investigaciones adicionales para lograr OPAs con distancias más cortas entre antenas, para evitar la aparición de lóbulos de rejilla o *grating lobes*. Una aproximación bajo investigación implica el uso de metamateriales entre antenas para evitar el acoplamiento y poder acercar las antenas a una distancia menor que $\lambda/2$. Además, se están considerando nuevos diseños con formas alternativas para los segmentos laterales para investigaciones futuras. El objetivo es lograr emisores más grandes con una alta sensibilidad de escaneo.

Nuevos enfoques para el diseño de antenas ultraeficientes.

Actualmente, el grupo de investigación está en proceso de patentar una nueva técnica para lograr emisores con una altísima eficiencia de radiación. Este método es compatible con las plataformas SOI y Si_3N_4 y potencialmente permite una direccionalidad de $D = 1$. Por lo que toda la potencia inyectada a la antena se dirigirá a la dirección de apuntamiento. Los prototipos han sido sometidos a pruebas de laboratorio y las antenas pudieron emitir luz fuera del chip. Sin embargo, se requiere una investigación adicional para abordar ciertos problemas técnicos relacionados con el empaquetado óptico de la solución. Este diseño abre posibilidades para utilizar antenas ópticas integradas como solución para sistemas donde la potencia radiada es crítica, como en el LIDAR para vehículos autónomos.

C. Curriculum Vitae

Pablo Ginel Moreno earned his BSc and MSc in Telecommunication Engineering from the Universidad de Málaga in 2018 and 2020 respectively. In 2021 he received a national scholarship from the Spanish Ministry of Science that funded his Ph.D. on the development of surface-emitting metamaterial antennas supervised by Prof. Dr. Alejandro Ortega Moñux and Dr. Pavel Cheben. The work developed in this PhD thesis was mostly done in the Photonics & Rf Lab at University of Malaga but in close collaboration with the National Research Council of Canada (NRC). A complete list of his publications is given below.

Articles in International Journals

1. **Pablo Ginel-Moreno**, Abdelfettah Hadij-ElHouati, Alejandro Sánchez-Postigo, J. Gonzalo Wangüemert-Pérez, Íñigo Molina-Fernández, Jens H. Schmid, Pavel Cheben and Alejandro Ortega-Moñux, "On-chip metamaterial antenna array with distributed Bragg deflector for generation of collimated steerable beams," Laser & Photonics Reviews 16(9), 2200164 (2022).
2. **Pablo Ginel-Moreno**, Alejandro Sánchez-Postigo, José de-Oliva-Rubio, Abdelfettah Hadij-ElHouati, Winnie N. Ye, J. Gonzalo Wangüemert-Pérez, Íñigo Molina-Fernández, Jens H. Schmid, Pavel Cheben, and Alejandro Ortega-Moñux, "Millimeter-long metamaterial surface-emitting antenna in the silicon photonics platform," Optics Letters 46(15), 3733- 3736 (2021).
3. **Pablo Ginel-Moreno**, Daniel Pereira-Martín, Abdelfettah Hadij-ElHouati, Winnie N. Ye, Daniele Melati, Dan-Xia Xu, Siegfried Janz, Alejandro Ortega-Moñux, J. Gonzalo Wangüemert-Pérez, Robert Halir, Íñigo Molina-Fernández, Jens H. Schmid, and Pavel Cheben, "Highly efficient optical antenna with small beam divergence in silicon waveguides," Optics Letters 45(20), 5668-5671 (2020).

International Conference Proceedings

1. **Pablo Ginel-Moreno**, Abdelfettah Hadij-El-Houati, Alejandro Sanchez-Postigo, Juan Gonzalo Wanguemert-Perez, Iñigo Molina-Fernandez, Jens H Schmid, Pavel Cheben and Alejandro Ortega-Moñux, "“Metamaterial antenna array fed by distributed Bragg deflector for beam steering on SOI platform,” IEEE Silicon Photonics Conference, April 2023, Arlington, USA. [Oral presentation]
2. **Pablo Ginel-Moreno**, Abdelfettah Hadij-ElHouati, Alejandro Sánchez-Postigo, J. Gonzalo Wangüemert-Pérez, Íñigo Molina-Fernández, Jens H. Schmid, Pavel Cheben and Alejandro Ortega-Moñux, “Metamaterial antenna array fed by distributed Bragg deflector for SOI platform,” 7th ePIXfab Silicon Photonics Summer School, Paris, France, 2022. [Poster presentation].

3. **Pablo Ginel-Moreno**, Alejandro Sánchez-Postigo, José de-Oliva-Rubio, Abdelfettah Hadij-ElHouati, Winnie N. Ye, J. Gonzalo Wangüemert-Pérez, Ínigo Molina- Fernández, Jens H Schmid, Pavel Cheben and Alejandro Ortega-Moñux, "Integrated metamaterial surface-emitting antenna for beam steering applications," 2021 IEEE 17th International Conference on Group IV Photonics (GFP), December 2022. [Remote presentation].

4. **Pablo Ginel-Moreno**, Daniel Pereira-Martín, Abdelfettah Hadij-ElHouati, Winnie N. Ye, Daniele Melati, Dan-Xia Xiu, Siegfried Janz, Alejandro Sanchez-Postigo, Juan Gonzalo Wanguemert-Perez, Robert Halir, Iñigo Molina-Fernandez, Jens H. Schmid, Pavel Cheben and Alejandro Ortega-Moñux, "Diseño de antena óptica integrada de haz estrecho en tecnología silicon-on- insulator," XII Reunión Española de Optoelectrónica (OPTOEL 2021), [Remote presentation].

Patents

1. Pavel Cheben, Jens H. Schmid, **Pablo Ginel-Moreno**, Daniel Pereira-Martín, Abdelfettah Hadij-elHouati, Winnie N. Ye, Daniele Melati, Dan-Xia Xu, Siegfried Janz, Alejandro Sánchez-Postigo, Alejandro Ortega-Moñux, Ínigo Molina-Fernández, J. Gonzalo Wangüemert-Pérez, “Waveguide antenna,” Patent WO2022013779A1 (WO). National Research Council Of Canada. 2022.

Awards

1. **June 2022** Best student contribution at 7th ePIXfab Silicon Photonics Summer School.
2. **May 2022** Best MSc Thesis. Given by DEKRA Spain.
3. **December 2021** Best Student Paper Award (First Place), 2021 IEEE Group IV Photonics Conference.
4. **April 2020** Best MSc Thesis. Given by the Escuela Técnica superior de Ingeniería de Telecomunicación (ETSIT) de la Universidad de Málaga.
5. **February 2018** Best BSc Thesis. Given by the Escuela Técnica superior de Ingeniería de Telecomunicación (ETSIT) de la Universidad de Málaga.

Notorious participation in invited/keynote conferences (first three authors)

1. P. Cheben, J.H. Schmid, **P. Ginel-Moreno**, S. Khajavi, R. Korcek, W. Fraser, D. Sirmaci, A. F. Hinestrosa, J.M. Luque-González, D. Pereira-Martín, A. Sánchez-Postigo, A. Hadij-ElHouati, D. Benedikovic, A. Ortega-Moñux, J. G. Wangüemert-Pérez, I. Molina-Fernández, R. Halir, W. N. Ye, D. Melati, C. Alonso-Ramos, D. González-Andrade, L. Vivien, I. Staude, J. Zhang, M. Milanizadeh, D.-X. Xu, Y. Grinberg, R. Cheriton, S. Janz, S. Wang, M. Vachon and M. Dado, "Subwavelength-engineered metamaterial devices for integrated photonics," 23rd International Conference on Transparent Optical Networks (ICTON 2023), 2023, Bucharest, Romania. [Oral presentation].

2. Juan Gonzalo Wangüemert-Pérez, Carlos Pérez-Armenta, **Pablo Ginel-Moreno**, José Manuel Luque-González, Abdelfettah Hadij-El Houati, Alejandro Sánchez Postigo, Jose

de Oliva Rubio, Alejandro Ortega-Moñux, Robert Halir, Jens H Schmid, Pavel Cheben, Íñigo Molina-Fernández, "Bricked and evanescently-coupled topologies: expanding the portfolio of subwavelength metamaterial silicon photonic devices," Integrated Optics: Devices, Materials, and Technologies XXVII (SPIE2023), 2023, San Francisco, California, United States. [Oral presentation]

3. Alejandro Sánchez Postigo, **Pablo Ginel-Moreno**, Daniel Pereira-Martin, Abdelfettah Hadij-ElHouati, J. Manuel LuqueGonzález, Carlos Pérez-Armenta, J. Gonzalo Wangüemert-Pérez, Alejandro Ortega-Moñux, Robert Halir, Jens H. Schmid, Jordi Soler Penadés, Milan Nedeljkovic, Winnie N. Ye, Goran Z. Mashanovich, Pavel Cheben and Íñigo Molina-Fernández, "Subwavelength-engineered metamaterial devices for integrated Photonics," in 2022 Smart Photonic and Optoelectronic Integrated Circuits (SPIE OPTO), San Francisco, USA, 2022. [Oral presentation].

4. Alejandro Sánchez-Postigo, **Pablo Ginel-Moreno**, Alejandro Ortega-Moñux, J. Gonzalo Wangüemert-Perez, Robert Halir, Daniel Pereira-Martín, Abdelfettah Hadij-ElHouati, Jens H. Schmid, Shurui Wang, Martin Vachon, Dan-Xia Xu, Winnie N. Ye, Jordi Soler-Penadés, Milos Nedeljkovic, Goran Z. Mashanovich, Íñigo Molina- Fernández, "Building high-performance integrated optical devices using subwavelength grating metamaterials," European Optical Society Annual Meeting (ECIO2021), Rome, Italy, 2021. [Oral presentation].

Bibliography

[1] Gordon E Moore. "Cramming More Components onto Integrated Circuits". In: *Proceedings of the IEEE* 86.1 (1998), pp. 82–85.

[2] E. Desurvire. "Optical Communications in 2025". In: *2005 31st European Conference on Optical Communication, ECOC 2005*. Vol. 1. 2005, pp. 5–6.

[3] N. Holonyak. "The Semiconductor Laser: A Thirty-Five-Year Perspective". In: *Proceedings of the IEEE* 85.11 (1997), pp. 1678–1693.

[4] E.L. Wooten et al. "A Review of Lithium Niobate Modulators for Fiber-Optic Communications Systems". In: *IEEE Journal of Selected Topics in Quantum Electronics* 6.1 (2000), pp. 69–82.

[5] K. Takada et al. "A.2.5 GHz-spaced 1080-Channel Tandem Multi/Demultiplexer Covering the. S-, C-, and L-bands Using an Arrayed-Waveguide Grating with Gaussian Passbands as a Primary Filter". In: *IEEE Photonics Technology Letters* 14.5 (2002), pp. 648–650.

[6] S. Janz et al. "Planar Waveguide Echelle Gratings in Silica-on-Silicon". In: *IEEE Photonics Technology Letters* 16.2 (2004), pp. 503–505.

[7] Pavel Cheben. "Wavelength Dispersive Planar Waveguide Devices: Echelle and Arrayed Waveguide Gratings". In: *Optical Waveguides*. CRC Press, 2007.

[8] Richard Soref. "Silicon Photonics: A Review of Recent Literature". In: *Silicon* 2.1 (2010), pp. 1–6.

[9] Shawn Yohanes Siew et al. "Review of silicon photonics technology and platform development". In: *Journal of Lightwave Technology* 39.13 (2021), pp. 4374–4389.

[10] Wim Bogaerts and Lukas Chrostowski. "Silicon photonics circuit design: methods, tools and challenges". In: *Laser & Photonics Reviews* 12.4 (2018), p. 1700237.

[11] Koji Yamada. "Silicon Photonic Wire Waveguides: Fundamentals and Applications". In: *Silicon Photonics II: Components and Integration*. Ed. by David J. Lockwood and Lorenzo Pavesi. Topics in Applied Physics. Berlin, Heidelberg: Springer, 2011, pp. 1–29.

[12] Xiaogang Chen. *Nonlinear Optics in Silicon Photonic Wires: Theory and Applications*. Columbia University, 2007.

[13] Yole Développement. *Silicon Photonics. Market and Technology Report, 2021*.

[14] J. A. Tatum et al. "VCSEL-Based Optical Transceivers for Future Data Center Applications". In: *Optical Fiber Communication Conference, Paper M3F.6*. 2018.

[15] Isiaka Alimi et al. "A Review of Self-Coherent Optical Transceivers: Fundamental Issues, Recent Advances, and Research Directions". In: *Applied Sciences* 11.16 (2021), p. 7554.

[16] Mehtab Singh et al. "Millimeter-Wave Hybrid OFDM-MDM Radio over Free Space Optical Transceiver for 5G Services in Desert Environment". In: *Alexandria Engineering Journal* 60.5 (2021), pp. 4275–4285.

[17] Fabienne Saliou et al. "Optical Access Network Interfaces for 5G and beyond [Invited]". In: *Journal of Optical Communications and Networking* 13.8 (2021), pp. D32–D42.

[18] Jayoung Kim et al. "Wearable Biosensors for Healthcare Monitoring". In: *Nature Biotechnology* 37.4 (2019), pp. 389–406.

[19] Yung-Tsan Chen et al. "Review of Integrated Optical Biosensors for Point-of-Care Applications". In: *Biosensors* 10.12 (2020), p. 209.

[20] Lars S. Madsen et al. "Quantum Computational Advantage with a Programmable Photonic Processor". In: *Nature* 606.7912 (2022), pp. 75–81.

[21] Federico Vernuccio et al. "Artificial Intelligence in Classical and Quantum Photonics". In: *Laser & Photonics Reviews* 16.5 (2022), p. 2100399.

[22] Xiaosheng Zhang et al. "A Large-Scale Microelectromechanical-Systems-Based Silicon Photonics LiDAR". In: *Nature* 603.7900 (2022), pp. 253–258.

[23] Christopher Vincent Poulton et al. "Long-Range LiDAR and Free-Space Data Communication With High-Performance Optical Phased Arrays". In: *IEEE Journal of Selected Topics in Quantum Electronics* 25.5 (2019), pp. 1–8.

[24] Christopher V. Poulton et al. "Coherent LiDAR with an 8,192-element optical phased array and driving laser". In: *IEEE Journal of Selected Topics in Quantum Electronics* 28.5 (2022), pp. 1–8.

[25] Ravi Mahajan et al. "Co-Packaged Photonics For High Performance Computing: Status, Challenges And Opportunities". In: *Journal of Lightwave Technology* 40.2 (2022), pp. 379–392.

[26] Cyriel Minkenberg et al. "Co-Packaged Datacenter Optics: Opportunities and Challenges". In: *IET Optoelectronics* 15.2 (2021), pp. 77–91.

[27] Pavel Cheben et al. "Subwavelength Integrated Photonics". In: *Nature* 560.7720 (2018), pp. 565–572.

[28] Robert Halir et al. "Subwavelength-Grating Metamaterial Structures for Silicon Photonic Devices". In: *Proceedings of the IEEE* 106.12 (2018), pp. 2144–2157.

[29] José Manuel Luque-González et al. "A Review of Silicon Subwavelength Gratings: Building Break-through Devices with Anisotropic Metamaterials". In: *Nanophotonics* 10.11 (2021), pp. 2765–2797.

[30] Robert Halir et al. "Ultra-Broadband Nanophotonic Beamsplitter Using an Anisotropic Sub-Wavelength Metamaterial". In: *Laser & Photonics Reviews* 10.6 (2016), pp. 1039–1046.

[31] Carlos Pérez-Armenta et al. "Polarization Insensitive Metamaterial Engineered Multimode Interference Coupler in a 220 Nm Silicon-on-Insulator Platform". In: *Optics & Laser Technology* 164 (2023), p. 109493.

[32] José Manuel Luque-González et al. "Polarization Splitting Directional Coupler Using Tilted Subwavelength Gratings". In: *Optics Letters* 45.13 (2020), pp. 3398–3401.

[33] Pablo Ginel-Moreno et al. "On-Chip Metamaterial Antenna Array with Distributed Bragg Deflector for Generation of Collimated Steerable Beams". In: *Laser & Photonics Reviews* 16.9 (2022), p. 2200164.

[34] José Manuel Luque-González et al. "An Ultracompact GRIN-Lens-Based Spot Size Converter Using Subwavelength Grating Metamaterials". In: *Laser & Photonics Reviews* 13.11 (2019), p. 1900172.

[35] Daniel Pereira-Martín et al. "Complex Spectral Filters in Silicon Waveguides Based on Cladding-Modulated Bragg Gratings". In: *Optics Express* 29.11 (2021), pp. 15867–15881.

[36] Carlos García-Meca et al. "On-Chip Wireless Silicon Photonics: From Reconfigurable Interconnects to Lab-on-Chip Devices". In: *Light: Science & Applications* 6.9 (2017), e17053–e17053.

[37] Alba Espinosa-Soria, Amadeu Griol, and Alejandro Martínez. "Experimental Measurement of Plasmonic Nanostructures Embedded in Silicon Waveguide Gaps". In: *Optics Express* 24.9 (2016), pp. 9592–9601.

[38] Alba Espinosa-Soria et al. "Coherent Control of a Plasmonic Nanoantenna Integrated on a Silicon Chip". In: *ACS Photonics* 5.7 (2018), pp. 2712–2717.

[39] Rafael S. Zola et al. "Dynamic Control of Light Direction Enabled by Stimuli-Responsive Liquid Crystal Gratings". In: *Advanced Materials* 31.7 (2019), p. 1806172.

[40] Yi-Long Li et al. "Tunable Liquid Crystal Grating Based Holographic 3D Display System with Wide Viewing Angle and Large Size". In: *Light: Science & Applications* 11.1 (2022), p. 188.

[41] Youmin Wang et al. "2D Broadband Beamsteering with Large-Scale MEMS Optical Phased Array". In: *Optica* 6.5 (2019), pp. 557–562.

[42] Karel Van Acoleyen et al. "Off-Chip Beam Steering with a One-Dimensional Optical Phased Array on Silicon-on-Insulator". In: *Optics Letters* 34.9 (2009), pp. 1477–1479.

[43] J. K. Doylend et al. "Two-Dimensional Free-Space Beam Steering with an Optical Phased Array on Silicon-on-Insulator". In: *Optics Express* 19.22 (2011), pp. 21595–21604.

[44] David Kwong et al. "On-Chip Silicon Optical Phased Array for Two-Dimensional Beam Steering". In: *Optics Letters* 39.4 (2014), pp. 941–944.

[45] Christopher V. Poulton et al. "Large-Scale Silicon Nitride Nanophotonic Phased Arrays at Infrared and Visible Wavelengths". In: *Optics Letters* 42.1 (2017), pp. 21–24.

[46] Kuanping Shang et al. "Uniform Emission, Constant Wavevector Silicon Grating Surface Emitter for Beam Steering with Ultra-Sharp Instantaneous Field-of-View". In: *Optics Express* 25.17 (2017), pp. 19655–19661.

[47] Hyun-Woo Rhee et al. "32 Gbps Data Transmission With 2D Beam-Steering Using a Silicon Optical Phased Array". In: *IEEE Photonics Technology Letters* 32.13 (2020), pp. 803–806.

[48] Jie Sun et al. "Large-Scale Nanophotonic Phased Array". In: *Nature* 493.7431 (2013), pp. 195–199.

[49] Hooman Abediasl and Hossein Hashemi. "Monolithic Optical Phased-Array Transceiver in a Standard SOI CMOS Process". In: *Optics Express* 23.5 (2015), pp. 6509–6519.

[50] Karel Van Acoleyen, Hendrik Rogier, and Roel Baets. "Two-Dimensional Optical Phased Array Antenna on Silicon-on-Insulator". In: *Optics Express* 18.13 (2010), pp. 13655–13660.

[51] Jian Yue et al. "Design of Monolithic 2D Optical Phased Arrays Heterogeneously Integrated with On-Chip Laser Arrays Based on SOI Photonic Platform". In: *Micromachines* 13.12 (2022), p. 2117.

[52] Reza Fatemi, Aroutin Khachaturian, and Ali Hajimiri. "A Nonuniform Sparse 2-D Large-FOV Optical Phased Array With a Low-Power PWM Drive". In: *IEEE Journal of Solid-State Circuits* 54.5 (2019), pp. 1200–1215.

[53] Kunyang Du et al. "Design of a Sparse Array for a One-Dimensional Non-Uniform Optical Phased Array". In: *JOSA B* 39.4 (2022), pp. 1141–1146.

[54] Aroutin Khachaturian, Reza Fatemi, and Ali Hajimiri. "Achieving Full Grating-Lobe-Free Field of View with Low-Complexity Co-Prime Photonic Beamforming Transceivers". In: *Photonics Research* 10.5 (2022), A66–A73.

[55] Christopher Rogers et al. "A Universal 3D Imaging Sensor on a Silicon Photonics Platform". In: *Nature* 590.7845 (2021), pp. 256–261.

[56] Daniel Benedikovič et al. "Circular Optical Phased Array with Large Steering Range and High Resolution". In: *Sensors* 22.16 (2022), p. 6135.

[57] Chung-Yu Hsu, Gow-Zin Yiu, and You-Chia Chang. "Free-Space Applications of Silicon Photonics: A Review". In: *Micromachines* 13.7 (2022), p. 990.

[58] Yongjun Guo et al. "Integrated Optical Phased Arrays for Beam Forming and Steering". In: *Applied Sciences* 11.9 (2021), p. 4017.

[59] Jingwen He, Tao Dong, and Yue Xu. "Review of Photonic Integrated Optical Phased Arrays for Space Optical Communication". In: *IEEE Access* 8 (2020), pp. 188284–188298.

[60] Martijn J. R. Heck. "Highly Integrated Optical Phased Arrays: Photonic Integrated Circuits for Optical Beam Shaping and Beam Steering". In: *Nanophotonics* 6.1 (2017), pp. 93–107.

[61] Behrooz Abiri et al. "Electronic Two-Dimensional Beam Steering for Integrated Optical Phased Arrays". In: *Optical Fiber Communication Conference, Paper M2K.7*. Optica Publishing Group, 2014.

[62] Steven A. Miller et al. "Large-Scale Optical Phased Array Using a Low-Power Multi-Pass Silicon Photonic Platform". In: *Optica* 7.1 (2020), pp. 3–6.

[63] Taehwan Kim et al. "A Single-Chip Optical Phased Array in a Wafer-Scale Silicon Photonics/CMOS 3D-Integration Platform". In: *IEEE Journal of Solid-State Circuits* 54.11 (2019), pp. 3061–3074.

[64] Chi-Wai Chow et al. "Actively Controllable Beam Steering Optical Wireless Communication (OWC) Using Integrated Optical Phased Array (OPA)". In: *Journal of Lightwave Technology* 41.4 (2023), pp. 1122–1128.

[65] Yunhan Wu et al. "Multi-Beam Optical Phase Array for Long-Range LiDAR and Free-Space Data Communication". In: *Optics & Laser Technology* 151 (2022), p. 108027.

[66] Konstantinos S. Lekkas and George T. Kanellos. "Silicon Photonic Free-Space Beam Steered Optical Switch Using Wavelength Tuned Nanoantennas". In: *Integrated Photonics Platforms II*. Vol. 12148. SPIE, 2022, pp. 76–81.

[67] Karan K. Mehta et al. “Integrated Optical Multi-Ion Quantum Logic”. In: *Nature* 586.7830 (2020), pp. 533–537.

[68] R. J. Niffenegger et al. “Integrated Multi-Wavelength Control of an Ion Qubit”. In: *Nature* 586.7830 (2020), pp. 538–542.

[69] Sangsik Kim et al. “Photonic Waveguide to Free-Space Gaussian Beam Extreme Mode Converter”. In: *Light: Science & Applications* 7.1 (2018), p. 72.

[70] Emiel Dieussaert, Roel Baets, and Yanlu Li. “Silicon Photonics Based Laser Doppler Vibrometer for Non-Contact Photoacoustic Sensing”. In: *Smart Photonic and Optoelectronic Integrated Circuits 2023*. Vol. 12425. SPIE, 2023, pp. 66–71.

[71] Saneyuki Suyama et al. “Doppler Velocimeter and Vibrometer FMCW LiDAR with Si Photonic Crystal Beam Scanner”. In: *Optics Express* 29.19 (2021), pp. 30727–30734.

[72] P. Bhargava et al. “Fully Integrated Coherent LiDAR in 3D-Integrated Silicon Photonics/65nm CMOS”. In: *2019 Symposium on VLSI Circuits*. 2019 Symposium on VLSI Circuits. 2019, pp. C262–C263.

[73] Yoshisada Koyama et al. “SOTA: Small Optical Transponder for Micro-Satellite”. In: *2011 International Conference on Space Optical Systems and Applications (ICSOS)*. 2011, pp. 97–101.

[74] Alberto Carrasco-Casado et al. “LEO-to-ground Optical Communications Using SOTA (Small Optical TrAnsponder) – Payload Verification Results and Experiments on Space Quantum Communications”. In: *Acta Astronautica* 139 (2017), pp. 377–384.

[75] *The anatomy of an autonomous vehicle*. Ouster. URL: `https://ouster.com/blog/the-anatomy-of-an-autonomous-vehicle` (visited on 04/14/2023).

[76] Constantine A. Balanis. *Antenna Theory: Analysis and Design*. John Wiley & Sons, 2015.

[77] *High-Performance Digital Lidar: Autonomous Vehicles, Robotics, Industrial a...* Ouster. URL: `https://ouster.com/` (visited on 04/14/2023).

[78] *Envision the Future*. Velodyne Lidar. URL: `https://velodynelidar.com/` (visited on 04/14/2023).

[79] R.A. Conant et al. “A Flat High-Frequency Scanning Micromirror”. In: *2000 Solid-State, Actuators, and Microsystems Workshop Technical Digest*. 2000 Solid-State, Actuators, and Microsystems Workshop. Hilton Head, South Carolina, USA: Transducer Research Foundation, Inc., 2000, pp. 6–9.

[80] Deng-Ke Yang and Shin-Tson Wu. *Fundamentals of Liquid Crystal Devices*. John Wiley & Sons, 2014.

[81] Dingkang Wang, Connor Watkins, and Huikai Xie. “MEMS Mirrors for LiDAR: A Review”. In: *Micromachines* 11.5 (2020), p. 456.

[82] Bahaa E. A. Saleh and Malvin Carl Teich. *Fundamentals of Photonics*. John Wiley & Sons, 2019.

[83] M Born and E Wolf. *Principle of Optics*. Pergamon Press, Oxford, 1991.

[84] Sophocles J Orfanidis. *Electromagnetic Waves and Antennas*. Rutgers University New Brunswick, NJ, 2002.

[85] David N. Hutchison et al. “High-Resolution Aliasing-Free Optical Beam Steering”. In: *Optica* 3.8 (2016), pp. 887–890.

[86] Langlin Cui et al. “Two-Dimensional Scanning of Silicon-Based Focal Plane Array with Field-of-View Splicing Technology”. In: *Optics Express* 31.2 (2023), pp. 1464–1474.

[87] Farshid Ashtiani and Firooz Aflatouni. “N × N Optical Phased Array with 2N Phase Shifters”. In: *Optics Express* 27.19 (2019), pp. 27183–27190.

[88] Enxiao Luan et al. “Advances in Silicon Photonic Sensors Using Sub-Wavelength Gratings”. In: *2019 24th OptoElectronics and Communications Conference (OECC) and 2019 International Conference on Photonics in Switching and Computing (PSC)*. 2019, pp. 1–3.

[89] S.F. Helfert and R. Pregla. “Efficient Analysis of Periodic Structures”. In: *Journal of Lightwave Technology* 16.9 (1998), pp. 1694–1702.

[90] T. Tamir and S. T. Peng. “Analysis and Design of Grating Couplers”. In: *Applied physics* 14.3 (1977), pp. 235–254.

[91] Josué J. López et al. “Planar-Lens Enabled Beam Steering for Chip-scale LIDAR”. In: *2018 Conference on Lasers and Electro-Optics (CLEO)*. 2018, pp. 1–2.

[92] Ralf Waldhäusl et al. “Efficient Coupling into Polymer Waveguides by Gratings”. In: *Applied Optics* 36.36 (1997), pp. 9383–9390.

[93] Xu Wang et al. “Liquid-Crystal Blazed-Grating Beam Deflector”. In: *Applied Optics* 39.35 (2000), pp. 6545–6555.

[94] Shahrzad Khajavi et al. “Design of Compact Silicon Antennas Based on High Directionality Gratings”. In: *2020 IEEE Photonics Conference (IPC)*. 2020 IEEE Photonics Conference (IPC). 2020, pp. 1–2.

[95] Daniele Melati et al. “Design of Compact and Efficient Silicon Photonic Micro Antennas With Perfectly Vertical Emission”. In: *IEEE Journal of Selected Topics in Quantum Electronics* 27.1 (2021), pp. 1–10.

[96] Keisuke Kondo et al. “Fan-Beam Steering Device Using a Photonic Crystal Slow-Light Waveguide with Surface Diffraction Grating”. In: *Optics Letters* 42.23 (2017), pp. 4990–4993.

[97] Hiroyuki Ito et al. “Wide Beam Steering by Slow-Light Waveguide Gratings and a Prism Lens”. In: *Optica* 7.1 (2020), pp. 47–52.

[98] Takemasa Tamanuki, Hiroyuki Ito, and Toshihiko Baba. “Thermo-Optic Beam Scanner Employing Silicon Photonic Crystal Slow-Light Waveguides”. In: *Journal of Lightwave Technology* 39.4 (2021), pp. 904–911.

[99] Chin-Lin Chen. *Foundations for Guided-Wave Optics*. John Wiley & Sons, 2006. 482 pp.

[100] Allen Taflove, Ardavan Oskooi, and Steven G. Johnson. *Advances in FDTD Computational Electrodynamics: Photonics and Nanotechnology*. Artech House, 2013. 640 pp.

[101] Ardavan F. Oskooi et al. “Meep: A Flexible Free-Software Package for Electromagnetic Simulations by the FDTD Method”. In: *Computer Physics Communications* 181.3 (2010), pp. 687–702.

[102] R.C. Johnson, H.A. Ecker, and J.S. Hollis. "Determination of Far-Field Antenna Patterns from near-Field Measurements". In: *Proceedings of the IEEE* 61.12 (1973), pp. 1668–1694.

[103] *OSLO | Lambda Research Corporation.* URL: `https://lambdares.com/oslo` (visited on 04/22/2023).

[104] *Applied Nanotools Inc.* URL: `https://www.appliednt.com/` (visited on 05/06/2023).

[105] Masafumi Ayata et al. "Compact, Ultra-Broadband Plasmonic Grating Couplers". In: *Optics Express* 27.21 (2019), pp. 29719–29729.

[106] Alejandro Sánchez-Postigo et al. "Breaking the Coupling Efficiency–Bandwidth Trade-Off in Surface Grating Couplers Using Zero-Order Radiation". In: *Laser & Photonics Reviews* 15.6 (2021), p. 2000542.

[107] Shaoliang Yu et al. "Free-Form Micro-Optics Enabling Ultra-Broadband Low-Loss Off-Chip Coupling". In: *Laser & Photonics Reviews* n/a.n/a (2023), p. 2200025.

[108] Pavel Cheben et al. "Broadband Polarization Independent Nanophotonic Coupler for Silicon Waveguides with Ultra-High Efficiency". In: *Optics Express* 23.17 (2015), pp. 22553–22563.

[109] Pablo Ginel-Moreno et al. "Highly Efficient Optical Antenna with Small Beam Divergence in Silicon Waveguides". In: *Optics Letters* 45.20 (2020), pp. 5668–5671.

[110] Pablo Ginel-Moreno et al. "Millimeter-Long Metamaterial Surface-Emitting Antenna in the Silicon Photonics Platform". In: *Optics Letters* 46.15 (2021), pp. 3733–3736.

[111] Abdelfettah Hadij-ElHouati et al. "High-Efficiency Conversion from Waveguide Mode to an on-Chip Beam Using a Metamaterial Engineered Bragg Deflector". In: *Optics Letters* 46.10 (2021), pp. 2409–2412.

[112] Abdelfettah Hadij-ElHouati et al. "Low-Loss off-Axis Curved Waveguide Grating Demultiplexer". In: *Optics Letters* 46.19 (2021), pp. 4821–4824.

[113] Hyun-Woo Rhee et al. "32 Gbps Data Transmission With 2D Beam-Steering Using a Silicon Optical Phased Array". In: *IEEE Photonics Technology Letters* 32.13 (2020), pp. 803–806.

[114] Pavel Cheben et al. "Waveguide Antenna". Pat. WO2022013779A1 (WO). National Research Council Of Canada. 2022.